Cosmological particle production and curved spaces in an ultracold quantum gas

Celia Viermann
June 2022

Dissertation

submitted to the

Combined Faculty of Natural Sciences and Mathematics

of Heidelberg University, Germany

for the degree of

Doctor of Natural Sciences

put forward by

Celia Viermann

born in: Heidelberg

oral examination: 02.06.2022

Cosmological particle production and curved spaces in an ultracold quantum gas

Referees: Prof. Dr. Markus Oberthaler

Prof. Dr. Matthias Bartelmann

Summary

The dynamics of quantum fields in curved spacetime give rise to various intriguing phenomena. Among them is the production of particles in an expanding spacetime. This process is likely responsible for seeding the Universe's large-scale structure, which, in turn, causes the temperature fluctuations in the cosmic microwave background and grows into the distribution of galaxies and galaxy clusters we observed today. In this work, we simulate this process in an ultracold quantum gas. The simulation is based on a novel and particularly straightforward mapping between a mass-less, free, relativistic scalar field in a curved spacetime and the phononic excitations of a Bose-Einstein condensate. Here, the density distribution and speed of sound of the background condensate determine the geometry of the spacetime.

Additionally, this thesis introduces a new ultracold atom machine that creates and controls a quasi-two-dimensional Bose-Einstein condensate of potassium-39. This experimental system combines a high control over the condensate's density with the possibility to dynamically adjust the atomic interaction – and thus the speed of sound – via a broad Feshbach resonance. We use this control to implement the two aspects of a Friedmann-Lemaître-Robertson-Walker (FLRW) metric: spatial curvature and the expansion of space.

To demonstrate spatial curvature, we probe wave packet dynamics and show that a harmonically trapped Bose-Einstein condensate approximates a hyperbolically curved space.

For the expansion of space, we perform a global change of the speed of sound. We realize three different power-law expansions, corresponding to accelerated, uniform, and decelerated expansion. For all three, we observe the emergence of fluctuations equivalent to cosmological particle production. To characterize these fluctuations, we compute their correlation function and power spectrum. In the time evolution of these quantities after the expansion, we identify an intriguing feature. It is connected to a complex phase of the produced quantum state and shows a clear dependence on the expansion history. Understanding if and how such a feature can be used in real cosmological observations is an intriguing prospect for future research.

Additionally, a good agreement between our experimental results and analytical predictions confirms that our experimental system simulates the dynamics of a quantum field in a curved and expanding space. This is the starting point for the future investigation of more complex spacetime geometries.

Zusammenfassung

Die Dynamik von Quantenfeldern in einer gekrümmten Raumzeit führt zu einer Reihe faszinierender Phänomene, darunter die Erzeugung von Teilchen in einer expandierenden Raumzeit. Im frühen Universum erzeugt dieser Prozess vermutlich den Ausgangspunkt der großskaligen Strukturen, die wir heutzutage in den Temperaturschwankungen des kosmischen Mikrowellenhintergrunds und der Verteilung der Galaxien und Galaxienhaufen beobachten. In dieser Arbeit simulieren wir einen solchen Prozess in einem ultrakalten Quantengas. Dies basiert auf einer neuartigen und besonders direkten Transformation zwischen einem Masse-losen, freien, relativistischen Skalarfeld in einer gekrümmten Raumzeit und den phononischen Anregungen eines Bose-Einstein-Kondensats. Hierbei bestimmen Dichteverteilung und des Hintergrundkondensats die Geometrie der Raumzeit.

Diese Arbeit beginnt mit der Beschreibung eines neuen experimentellen Aufbaus, welcher ein quasi-zweidimensionales Bose-Einstein-Kondensat aus Kalium-39 Atomen erzeugt. Der Aufbau erlaubt eine feine Kontrolle der Kondensat-Dichte, kombiniert mit der Möglichkeit, die atomare Wechselwirkung – und damit die Schallgeschwindigkeit – dynamisch einzustellen. Letzteres wird durch die breite Feshbach Resonanz von Kalium-39 ermöglicht. Dies nutzen wir, um die beiden Aspekte einer Friedmann-Lemaître-Robertson-Walker (FLRW)-Metrik zu simulieren: räumliche Krümmung und die zeitliche Ausdehnung des Raums.

Für die räumliche Krümmung untersuchen wir die Dynamik von Wellenpaketen und können zeigen, dass ein Kondensat in einer harmonischen Falle näherungsweise einen hyperbolisch gekrümmten Raum implementiert.

Die Ausdehnung des Raumes erreichen wir mit einer globalen Änderung der Schallgeschwindigkeit. Für drei verschiedene Expansions-Szenarien (beschleunigt, gleichmäßig und abgebremst) beobachten wir das Auftreten von Fluktuationen, die der kosmologischen Teilchenproduktion entsprechen. Wir charakterisieren die Fluktuationen durch ihre Korrelations-Funktion sowie ihr Leistungsspektrum. In der Zeitentwicklung dieser Größen nach der Expansion identifizieren wir ein besonderes Merkmal. Dieses ist mit einer komplexen Phase des erzeugten Quantenzustands verbunden und zeigt eine deutliche Abhängigkeit von der Expansionsgeschichte. Ob und wie ein solches Merkmal für reale kosmologischen Beobachtungen genutzt werden kann, ist eine faszinierende Fragestellung für zukünftige Forschung.

Darüber hinaus bestätigt die gute Übereinstimmung unserer Messergebnisse mit analytischen Vorhersagen, dass unser experimentelles System in der Tat die Dynamik eines Quantenfeldes in einer gekrümmten und expandierenden Raumzeit simuliert. Dies dient als Ausgangspunkt für die Untersuchung komplexerer Raumzeit-Geometrien in der Zukunft.

Contents

Chapter 1

Introduction

Quantum field theory and general relativity are two fundamental pillars of modern physics. The first describes a vast variety of quantum processes, containing phenomena as strange and wonderful as entanglement or the fluctuations of the vacuum. The latter is an elegant formulation of gravity as the curvature of spacetime. While considerable effort is being put into combining these into a comprehensive theory of quantum gravity, this has not yet been achieved.

In semi-classical approaches, the dynamics of quantum fields are evaluated on a curved spacetime. So far, this approach has led to the prediction of Hawking radiation, emitted at the horizon of a black hole [1, 2], and Unruh radiation detected by an accelerated observer. In the context of cosmology, the expansion of spacetime itself leads to the creation of particles [3, 4]. During inflation, a phase of rapid expansion shortly after the Big-Bang, this process likely seeded the large-scale structure of our Universe. This structures can be seen in the temperature fluctuations of the cosmic microwave background and grow into galaxy clusters and the cosmic web in the more recent Universe [5]. To better understand the phenomenon of cosmological particle creation and the interplay between quantum fields and curved spacetimes in general, an experimental approach to this field of physics is highly desirable. The control over spacetime itself is far beyond our experimental reach since it is notoriously stiff, and huge masses or energies are necessary to curve it. However, the dynamics of quantum fields in curved spacetimes can be simulated in experimentally accessible model systems.

In 1981, Unruh [6] realized that the same mathematical model describes both the dynamics of a scalar field in a curved metric and wave excitations in a classical fluid with a distinctive flow pattern. He proposed to use this analogy for the simulation of a black hole event horizon with water. The idea lay dormant for almost ten

years until it was picked up and developed further [7–9]; and it took almost another ten years until a community had formed and the idea gathered momentum under the name of analog gravity. More exotic fluids or fluid-like model systems were introduced including superfluids like ^{4}He [10, 11] and Bose-Einstein condensates in ultra-cold atomic gases [12–15]. Thanks to impressive theoretical and experimental developments, black hole analogs have been realized both in classical [16–18] and superfluids [19–22], and the dynamical Casimir effect has been observed in ultracold gases [23]. Theoretical developments are well summarized in the reviews [24, 25] and [26] focuses on the experimental progress.

The investigation of analog expanding spacetimes in the form of Friedmann-Lemaître-Robertson-Walker (FLRW) metrics started in 2003. The FLRW metric describes a homogeneous and isotropic space and allows for the expansion of space as well as spherical, flat or hyperbolic spatial curvature. Research into analog FLRW spacetimes was sparked by progress in the ultracold atom community: the experimental demonstration of a Feshbach resonance [27, 28]. Magnetic Feshbach resonances change the scattering properties of atoms. They can be used to adjust the interaction between atoms and thus the speed of sound in an ultracold atomic gas. Control over the speed of sound, in turn, allows the simulation of an expanding spacetime: in a cosmological setting, the distance between two points can be defined by the duration of light propagation between those points. In an expanding space, light needs a longer time to cross from one point to the other. The same is true if the light becomes slower. Thus, the expansion of space is, at least mathematically, equivalent to a decrease in the speed of light. In a model system, the speed of light is replaced by the speed of sound. Feshbach resonances supply the necessary experimental control to implement this idea. Many variations on an analog FLRW metric have been explored [29–35], which differ in their mappings between the cosmological setting and the analog system. While Feshbach resonances are by now widely used, for example in quench experiments [36, 37], the only experimental realizations of an FLRW metric, so far, rely instead on an expanding one-dimensional ring-condensate [38, 39] or on a fluid of light [40].

Here, we report on the realization of an analog FLRW metric in a quasi-two dimensional Bose-Einstein condensate of potassium-39. The expansion of space is implemented by tuning the interaction between atoms. The second parameter of the FLRW metric, spatial curvature, is realized via the density distribution of the condensate. It is based on a novel and particularly direct mapping between the dynamics of a relativist, massless, scalar field and the condensate's phononic excitations. The mapping was developed within our collaboration and published in [41]. Potassium-39 was chosen for its broad Feshbach resonance, which allows

fine experimental control of the atomic interactions. However, potassium-39 is more difficult to cool and to condense than other atomic species.

This thesis focuses on the experimental side of implementing curved spacetimes. It consists of four major parts: the theoretical background for understanding the BEC, the FLRW metric, and their connection, the description of the experimental machine that creates and controls the two-dimensional condensate, the implementation of spatially curved geometries, and finally the realization of expanding spacetimes, and the observation of cosmological pair creation in the condensate. The results of the latter two parts are also published in [42].

Chapter 2 start with the mathematical description of a Bose-Einstein condensate and its excitations. Afterward, in chapter 3, the FLRW metric for an expanding, homogeneous, and isotropic spacetime is derived and connected with its application to cosmology. Chapter 4 derives the acoustic metric, i.e., it maps the dynamics of the phononic field of the condensate to those of a scalar field in the FLRW metric. The following two chapters are dedicated to the experimental machine itself. Chapter 5 introduces the methods for trapping an atomic cloud and cooling it to degeneracy, and chapter 6 gives a detailed description of the experimental setup. Chapter 7 takes a closer look at spherical and hyperbolically curved spaces and their implementation in the acoustic metric of a two-dimensional condensate. The experimental realization of a hyperbolic space is investigated in chapter 8 by tracing the propagation of wave packets in the condensate. Chapter 9 and chapter 10 describe the theoretical and experimental realisation of an expanding spacetime. The theoretical part also summarizes an analytic model for particle-pair creation in an expanding spacetime, and the experimental part reports on the observation and analysis of this intriguing phenomenon. Finally, chapter 11 summarizes the main results of this work and discusses open questions and prospects for future research.

Chapter 2

Theory of Bose-Einstein condensates

To simulate the dynamics of a quantum field in a curved spacetime, the dynamics of the field are mapped to the phononic excitations of a Bose-Einstein condensate (BEC). The analog metric of these excitations is connected to the sound-speed structure of the background condensate (see section 4.1). To experimentally achieve an analog spacetime, we need to understand how shape a condensate and its excitations. The purpose of this chapter is to provide this understanding. It starts with the Thomas-Fermi approximation in section 2.1, and the reduction to a quasi-two-dimensional BEC by 'freezing out' excitations along one direction in section 2.2. This defines the properties of the background condensate. The following two sections introduce perturbations on that background. Section 2.3 describes the Bogoliubov approximation, defines the acoustic regime, and connects the speed of sound to the properties of the condensate. Finally, the local density approximation is introduced in section 2.4 which allows for a position-dependent speed of sound.

2.1 Thomas-Fermi approximation

In the limit of classical fields, the atoms of a condensate are described by a collective wave function ϕ which fulfills the *Gross-Pitaevskii equation*

$$i\hbar\,\partial_t\phi = \left(-\frac{\hbar^2}{2m}\vec{\nabla}^2 + V(\vec{x}) + g|\phi|^2\right)\phi\ , \tag{2.1}$$

with the three-dimensional trapping potential $V(\vec{x})$ and the coupling g. The latter is related to the s-wave scattering length a_s of the atom-atom interaction by

$$g = \frac{4\pi\hbar^2}{m} a_s \ . \tag{2.2}$$

The kinetic term can be neglected for a dense cloud and a large trapping potential, which is the *Thomas Fermi approximation*. In this limit, the Gross-Pitaevski equation is solved by the ansatz

$$\phi_0 = \sqrt{n_{3d}(\vec{x})} \exp(-i\mu_0 t/\hbar) \ . \tag{2.3}$$

Inserting it into the simplified Gross-Piatevski equation yields

$$n_{3d}(\vec{x}) = \frac{\mu_0 - V(\vec{x})}{g} \ , \tag{2.4}$$

where μ_0 can be identified with the chemical potential. This shows the direct dependence of the density distribution on the trap's shape. Within the approximation, the condensate fills the potential to the energy μ_0, like water filling a bowl. Figure 2.1 illustrates this for the example of a harmonic trap in one dimension, which results in a parabolic density profile. The distance from the center at which the density vanishes is called the *Thomas Fermi radius* r_{TF}. A real-world condensate will not have this exact shape. The density decreases towards the edges, and the Thomas-Fermi approximation breaks down as the kinetic term can no longer be neglected. As a consequence, the density profile of a harmonically trapped condensate has a parabolic density profile around the center but displays slightly broadened wings at the edges.

2.2 Quasi two-dimensional BEC

A BEC can be reduced to quasi-two-dimensions by suppressing its excitations of along one direction. This is achieved by tight confinement. For the confined direction, the energy difference between the ground state and excited states is large. If the confinement is strong enough, excited states can no longer be populated and the dynamics of the BEC will be restricted to the remaining two dimensions. In typical settings, the length scale of atom-atom interaction is still small compared to the confinement. This is also the case for the experiments described in this work. Thus, scattering processes must still be treated as three-dimensional, and the coupling g remains unchanged. By integrating the strongly-confined direction, one can define an

effective 2d-density and effective 2d-coupling λ. For a harmonic trap in z-direction with frequency ω_z, the normalized ground state wave function along that direction is

$$\phi = \frac{1}{(\pi l^2)^{1/4}} \exp\left(-\frac{z^2}{2l^2}\right) , \tag{2.5}$$

with the characteristic length scale $l = \sqrt{\hbar/(m\omega_z)}$ of the harmonic oscillator. The integration of the confined dimension needs to be performed on the level of the Hamiltonian. The Hamiltonian has a standard kinetic and potential term and a quartic interaction $H_{\text{int}} = g\,\phi^*\phi\phi^*\phi$. While the kinetic and potential term remain unchanged during the integration, the interaction term changes to

$$H_{\text{int}} = \frac{g}{\pi l^2} \int dz \exp\left(-2z^2/l^2\right) \phi^*_{2d}\phi_{2d}\phi^*_{2d}\phi_{2d} = \lambda\,\phi^*_{2d}\phi_{2d}\phi^*_{2d}\phi_{2d} , \tag{2.6}$$

where eq. (2.2) was used for the 3d-coupling g and the effective 2d-coupling was defined as

$$\lambda = a_s \sqrt{8\pi\hbar^3\omega_z/m} . \tag{2.7}$$

Thus, the equation of motion for ϕ_{2d} is the Gross-Pitaevski equation with the coupling g replaced by λ. In the scope of this work, we will always work in this effective $2d$ description and use $n = \phi^*_{2d}\phi_{2d}$ to denote the effective two-dimensional density.

2.3 Perturbations - Bogoliubov approximation

Perturbations on a background condensate are described in the *Bogoliubov approximation*. The wave function is split into the mean-field ϕ_0 and a complex-valued perturbation $\delta\phi$

$$\phi = \phi_0 + \delta\phi , \tag{2.8}$$

which is inserted into the Gross-Pitaevski equation. Subtracting the background solution for ϕ and keeping only terms up to second order in the perturbation yields the equation

$$i\hbar\partial_t\,\delta\phi = -\frac{\hbar^2}{2m}\vec{\nabla}^2\delta\phi + V(\vec{x})\,\delta\phi + 2g|\phi_0|^2\,\delta\phi + g\,\phi_0^2\,\delta\phi^* . \tag{2.9}$$

This is a differential equation for the perturbations which still couple to the background. It is solved by the ansatz

$$\delta\phi = \mathrm{e}^{-i\mu t/\hbar}\left(u(\vec{x})\,\mathrm{e}^{-i\omega t} - v^*(\vec{x})\,\mathrm{e}^{i\omega t}\right) . \tag{2.10}$$

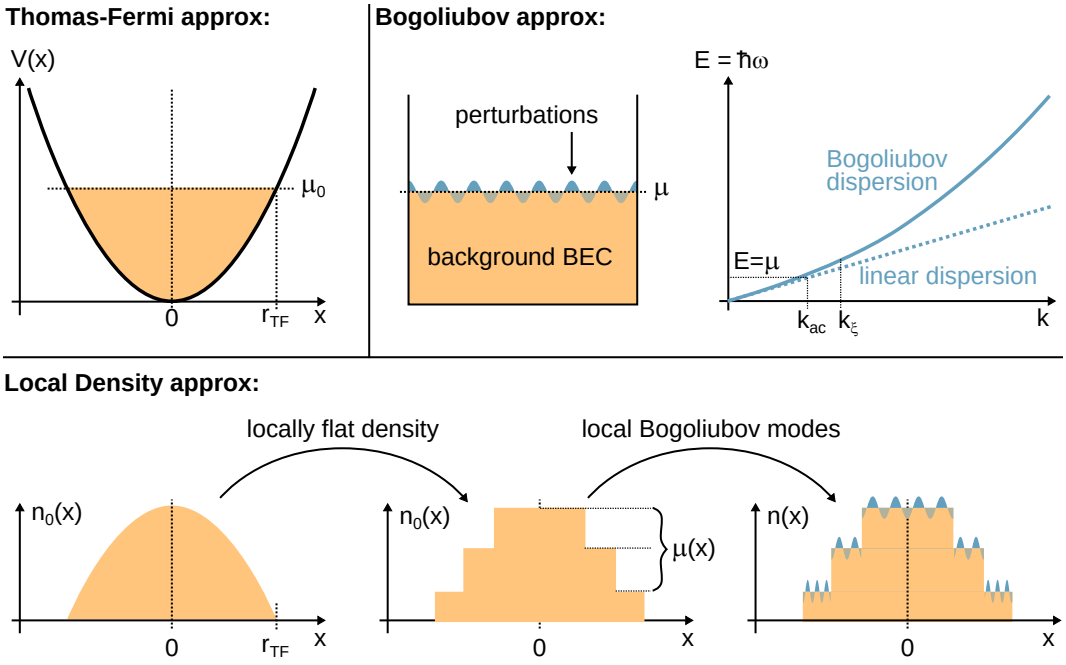

Figure 2.1: Thomas-Fermi, Bogoliubov and Local Density approximation. In the Thomas-Fermi approximation the kinetic term in the Gross-Pitaevski equation is neglected. In this approximation, the density distribution of a condensate fills a trap up to the chemical potential μ_0. The Bogoliubov approximation describes perturbations on a homogeneous background density. The dispersion relation of the perturbations is linear for small momenta and quadratic for large momenta. The slope of the linear part defines the speed of sound for phononic excitations. Characteristic momentum scales mark the transition point between linear and quadratic regimes, like the momentum of the healing length k_ξ or k_{ac}. For a non-homogeneous background, the local density approximation treats the background as locally flat. On the flat patches, the Bogoliubov approximation is used to define a local dispersion relation and speed of sound.

Note that the u and v in this chapter are not the same as the u and v in the calculations for particle creation in chapter 9. For a constant trap potential $V = \text{const} = \mu - gn$, the ansatz results in two equations for the positive and negative frequency solutions $\exp(\pm i\omega t)$, respectively

$$\left(-\frac{\hbar^2}{2m}\vec{\nabla}^2 + gn - \hbar\omega\right) u = gnv \,, \qquad \left(-\frac{\hbar^2}{2m}\vec{\nabla}^2 + gn + \hbar\omega\right) v = gnu \,, \tag{2.11}$$

where eq. (2.3) was used for the background condensate. A final ansatz $u, v = \exp\left(\pm i\vec{k}\vec{x}\right)$ yields the *Bogoliubov dispersion relation*

$$\hbar\omega = \sqrt{\frac{\hbar^2|k|^2}{2m}\left(\frac{\hbar^2|k|^2}{2m} + 2gn\right)} \,. \tag{2.12}$$

For large k, the dispersion relation is approximately quadratic

$$\omega \approx \frac{\hbar k^2}{2m} \tag{2.13}$$

and the perturbations have particle-like character. For small momenta k, the dispersion relation is approximately linear with

$$\omega \approx c_s k \,, \qquad c_s = \sqrt{\frac{gn}{m}} = \sqrt{\frac{\mu}{m}} \,. \tag{2.14}$$

which corresponds to sound waves, i.e., collective phononic excitations with the speed of sound c_s. Accordingly, it is called the *acoustic* or *phononic regime*. To distinguish the two cases, length and momentum scales can be defined, which mark the position of the transition between the two. A very common one is the *healing length* ξ_h and the corresponding momentum $k_\xi = 1/\xi_h$, defined via

$$\frac{\hbar^2}{2m\,\xi_h^2} \stackrel{!}{=} \mu \quad \Leftrightarrow \quad \hbar k_\xi = \sqrt{2}\, mc_s \,. \tag{2.15}$$

The healing length marks the position of the onset of the ´knee' in the dispersion relation (see Fig.2.1). A second scale is closer to the phononic regime and thus a more secure marker for the validity of a phononic approximation. We define it via the k-mode for which the energy in the linear dispersion equals the chemical potential

$$\hbar\,\omega_{\text{ac}} \stackrel{!}{=} \mu \quad \Leftrightarrow \quad \hbar k_{\text{ac}} = mc_s \,. \tag{2.16}$$

This measure will be used in chapter 10 when the validity of the linear regime is estimated for the real experiment.

2.4 Local density approximation

The Bogoliubov approximation in the previous section assumed a constant potential and thus a homogeneous density distribution. For a BEC in an inhomogeneous trap, excitation can be treated in the *local density approximation*. It assumes that the condensate is locally sufficiently homogeneous to define a position-dependent dispersion relation and speed of sound (see Fig 2.1). For a circularly symmetric, quasi-two-dimensional BEC, the sound speed is given by

$$c_s(r,\varphi) = \sqrt{\frac{n(r,\varphi)\cdot\lambda}{m}}\ . \tag{2.17}$$

Using appropriate traps, the density distribution and thus the sound speed of the condensate can be controlled. For this work, this will become important for realizing hyperbolic spaces in the condensate.

CHAPTER 3

Expanding and curved spacetimes

With the properties of a Bose-Einstein condensate discussed in the previous chapter, this chapter focuses on the metric-side of the analogy between a condensate and a curved spacetime. It starts with the brief description of general relativity (GR) in section 3.1 and describes which of its effects can be captured in analog models. Section 3.2 focuses on geodesics, and section 3.3 introduces the Friedmann-Lemaître-Robertson-Walker (FLRW) metric of a homogeneous and isotropic space. This metric allows for space to expand, and different types of expansion are defined in section 3.4. A connection between this metric and cosmology is established in section 3.5 and section 3.6 finally discusses cosmological particle production during a process called inflation and its possible connection to our Universe. This chapter is based on the works [5, 43–45].

3.1 General relativity and analog gravity models

The theory of general relativity connects gravity to the curvature of spacetime. It can be summarized by two effects. First, in a curved spacetime, particles and light propagate along generalized straight lines, the *geodesics* as is illustrated in fig. 3.1. Second, the presence of matter and energy curves the spacetime according to the *Einstein equations*. The interplay between both effects makes GR a formidable non-linear theory since the dynamics of matter, and the curvature of spacetime depend on each other and must be solved simultaneously. Analytically, this is only possible for very few selected geometries with strong symmetry assumptions. Among them is the Friedmann-Lemaître-Robertson-Walker (FLRW) metric which describes a homogeneous and isotropic space that may expand or contract. Analog systems, like

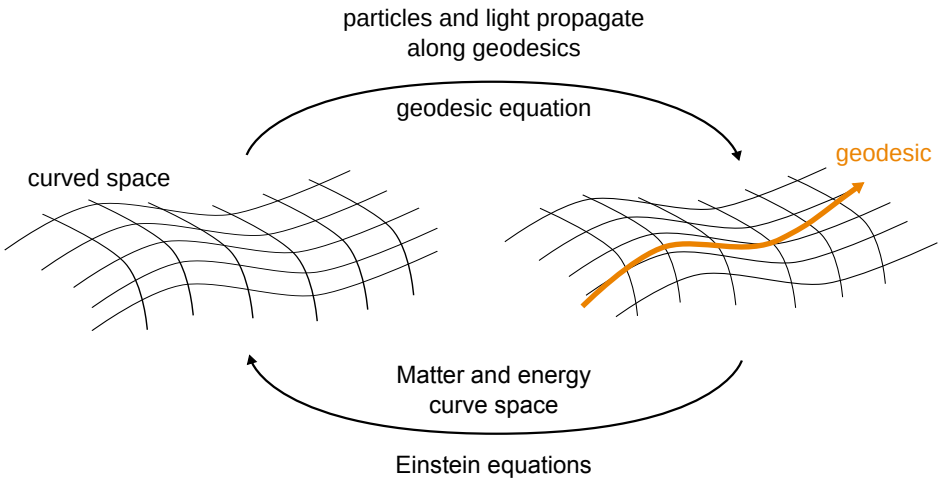

Figure 3.1: Curvature of spacetime and particle propagation in general relativity. In a curved space, particles and light propagate along geodesics. The matter and energy themselves lead to the curvature of space as is described in the Einstein equations. This leads to a back-reaction of the propagating matter on the spacetime itself. Thus, for a full solution of general relativity, the curvature of spacetime and the propagation of matter must be solved simultaneously.

the two-dimensional Bose-Einstein condensate considered in this work, simulate the dynamics of a quantum field in the curved spacetime (upper arrow in fig. 3.1), but they cannot capture the full non-linear dynamics. The back-reaction of the matter on the geometry of spacetime, (lower arrow), is not trivially included in these analog models [24]. For cosmological solutions, the back-reaction determines different expansion scenarios depending on the matter and energy content of the respective universe (see section 3.5). Therefore, in analog systems, the expansion must be imposed manually to probe the dynamics of a quantum field during the different scenarios.

3.2 Geodesics - propagation in curved spacetimes

A part of GR that is naturally captured in analog models is the propagation of excitations along geodesics which can be seen as the generalization Newton's first law to curved space. For flat space, the law states that objects move along straight

lines, which is mathematically formulated for one coordinate x^μ as

$$\frac{\mathrm{d}^2 x^\mu}{\mathrm{d}t^2} = 0 \,. \tag{3.1}$$

A straight line is a curve for which the tangent vector always points along the curve itself. This concept is generalized to curved space by the *geodesic equation*

$$\frac{\mathrm{d}^2 x^\mu}{\mathrm{d}\tau^2} + \Gamma^\mu{}_{\sigma\nu} \frac{\mathrm{d}x^\nu}{\mathrm{d}\tau} \frac{\mathrm{d}x^\sigma}{\mathrm{d}\tau} = 0 \,, \tag{3.2}$$

with τ a parameter of the curve, e.g. the eigentime of a moving particle. The second term takes into account that the tangent vector changes during movement on the curved surface. This is encoded in the connection Γ, the *Christoffel symbol* defined as

$$\Gamma^\mu{}_{\sigma\nu} = \frac{1}{2} g^{\mu\kappa} \left(\frac{\partial g_{\nu\kappa}}{\partial x^\sigma} + \frac{\partial g_{\sigma\kappa}}{\partial x^\nu} - \frac{\partial g_{\sigma\nu}}{\partial x^\kappa} \right) \,. \tag{3.3}$$

Geodesics are essential for the definition of distance between points. In flat space, the distance between two points is determined by the length of a straight line connecting them. In curved space, the same is true for the length of a geodesic, which is the shortest connection between the points. Therefore, the distance between points is calculated by integrating the line element along the geodesic connecting them. In this work, we will encounter geodesics in chapter 7 and chapter 8 for spaces with constant spherical and hyperbolic curvature. In these highly symmetric spaces, we will not solve the geodesic equation explicitly but use geometric arguments.

3.3 Friedmann-Lemaître-Robertson-Walker metric

The FLRW metric describes spacetimes that are spatially homogeneous and isotropic. These assumptions bring the metric into the very simple form discussed in this section. In general, a metric $g_{\mu\nu}$ encodes distances between points in a spacetime, where the greek indices μ and ν run over the time and all spatial dimensions. The metric is a symmetric tensor tensor which has ten degrees of freedom in 3 + 1 dimensions and six degrees of freedom in 2 + 1 dimensions. Each symmetry of the spacetime reduces these degrees of freedom. For example, the 3 + 1 dimensional spacetime of special relativity - Minkowski space - has the ten symmetries of the Lorentz group. These are three spatial translations, three spatial rotations, one

translation in time, and the three Lorentz boosts. Thus, the Minkowski metric has no degrees of freedom left. It takes the form

$$g_{\mu\nu} = \mathrm{diag}(-c^2, \mathbb{1}) \,, \tag{3.4}$$

with $\mathbb{1}$ representing he unit matrix with the size corresponding to the number of spatial dimensions. Often, the geometry is encoded by the line-element

$$\mathrm{d}s^2 \equiv g_{\mu\nu}\,\mathrm{d}x^\mu \mathrm{d}x^\nu \,, \tag{3.5}$$

where $\mathrm{d}x^\mu$ describes infinitesimal changes of the coordinates and a sum over repeated indices is implied according to the Einstein sum convention. For Minkowski space, the line element is

$$\mathrm{d}s^2 = -c^2\mathrm{d}t^2 + \mathrm{d}\vec{x}^{\,2}, \tag{3.6}$$

$$\tag{3.7}$$

with $\vec{x}$ denoting the spatial coordinate vector. The shape of both the metric and the line-element depend on the chosen coordinates. A coordinate transformation to spherical (polar) coordinates brings the line element of Minkowski space into the form

$$\mathrm{d}s^2 = -c^2\mathrm{d}t^2 + \mathrm{d}r^2 + r^2\mathrm{d}\Omega \,, \tag{3.8}$$

with r the radial coordinate, and $\mathrm{d}\Omega$ the solid angle element. In three dimensions it is $\mathrm{d}\Omega = \sin^2\vartheta\,\mathrm{d}\varphi^2 + \mathrm{d}\vartheta^2$, while it takes the form $\mathrm{d}\Omega = \mathrm{d}\varphi^2$ in two dimensions.

The Friedmann-Lemaître-Robertson-Walker metric is also based on strong symmetry assumptions, namely spatial homogeneity and isotropy. This assumption is known as the *cosmological principle* and sometimes also called *copernican principle*. It is equivalent with the statements that there is no extraordinary point or direction and that all observers will make equivalent observations along all directions. In comparison with Minkowski space, the time-symmetry is lifted which leaves a single time-dependent degree of freedom, the *scale factor* $a(t)$. In addition, the FLRW metric allows for (homogeneous) spatial curvature,[1] which leads to the line element

$$\mathrm{d}s^2 = -c^2\mathrm{d}t^2 + a^2(t)\left(\frac{\mathrm{d}u^2}{1-\kappa r^2} + u^2\mathrm{d}\Omega^2\right) \,, \tag{3.9}$$

[1] Note, that for different curvatures, the exact form of the symmetries changes but their number is not reduced.

with $a(t)$ the aforementioned scale factor and κ the curvature. The sign of κ determines the type of curvature: spherical curvature for $\kappa > 0$, hyperbolic curvature for $\kappa < 0$, and a flat space for $\kappa = 0$ (see chapter 7 for details). The time dependent function $a(t)$ is the aforementioned scale factor. As $a(t)$ increases/decreases in time, so do spatial distance which describes the expansion/contraction of space. As mentioned above, the exact form of the line-element depends on the choice of coordinates. The coordinates chosen here are called *reduced circumference coordinates* (see chapter 7 for more detail). These coordinates are *comoving coordinates*, i.e. they are time-independent. This is in contrast to *physical coordinates*, which absorb the time-dependence into the coordinates themselves.

For the above metrics and the line elements, distances are measured in the unit of length. Instead, distances can be measured in units of time - the time light needs to cover the respective distance. This is commonly used for the unit 'light year'. The FLRW metric then takes the form

$$\mathrm{d}s^2 = -\mathrm{d}t^2 + \frac{a^2(t)}{c^2}\left(\frac{\mathrm{d}u^2}{1-\kappa r^2} + u^2\mathrm{d}\Omega^2\right) , \tag{3.10}$$

which will be compared later to the acoustic metric in a Bose-Einstein condensate.

3.4 Accelerated, decelerated, or uniform expansion

The expansion of a universe can be accelerated, decelerated or uniformly expanding, depending on its matter content. To classify models the deceleration parameter q is used with

$$q = -\frac{\ddot{a}a}{\dot{a}^2} . \tag{3.11}$$

Here, $q > 0$ is a decelerated universe, $q = 0$ a uniformly expanding one and $q < 0$ an accelerated one. For power-law expansions with

$$a(t) \propto t^\gamma , \tag{3.12}$$

the deceleration parameter is

$$q = \frac{1-\gamma}{\gamma} . \tag{3.13}$$

Uniform expansion takes place for $\gamma = 1$, accelerated for $\gamma > 1$ and decelerated for $\gamma < 1$.

3.5 Connection to cosmology

So far, this chapter described the FLRW metric defined by the symmetry assumptions of spatial homogeneity and isotropy and how matter moves on geodesics, corresponding to the upper arrow in fig. 3.1. This is already all the information we need for implementing and testing an FLRW metric in an analog system. In this section and the following one, we lay the groundwork for possible future connections between observations in an analog system and a cosmological interpretation. This part can be skipped without loosing the narrative of the thesis. Reading should then continue with the derivation of the acoustic metric in chapter 4.

To establish the connection between an expansion scenario and the matter and energy content and curvature of a spacetime, the Einstein equations must be solved for the FLRW metric. The Einstein equations read

$$G_{\mu\nu} + \Lambda\, g_{\mu\nu} = \frac{8\pi G}{c^4} T_{\mu\nu} \,, \tag{3.14}$$

where Λ is the cosmological constant. $G_{\mu\nu}$ is the Einstein tensor which has the form

$$G_{\mu\nu} \equiv R_{\mu\nu} - \frac{1}{2} R g_{\mu\nu} \,, \tag{3.15}$$

with the Ricci-tensor $R_{\mu\nu}$ and Ricci scalar R

$$R_{\mu\nu} = R^{\alpha}{}_{\mu\alpha\nu} \,, \quad R = g^{\mu\nu} R_{\mu\nu} \,, \tag{3.16}$$

which are in turn defined via the Riemann curvature tensor

$$R^{\alpha}{}_{\mu\sigma\nu} = \partial_\sigma \Gamma^{\alpha}{}_{\nu\mu} - \partial_\nu \Gamma^{\alpha}{}_{\sigma\mu} + \Gamma^{\alpha}{}_{\sigma\lambda} \Gamma^{\lambda}{}_{\nu\mu} - \Gamma^{\alpha}{}_{\nu\lambda} \Gamma^{\lambda}{}_{\sigma\mu} \,. \tag{3.17}$$

Here, Γ again denotes the Christoffel symbols eq. (3.3) that already appeared in the section on geodesics section 3.2. In the last term of the Einstein equations contains the stress-energy tensor $T_{\mu\nu}$ which describes all forms of matter and energy in the spacetime. For an ideal fluid with density ρ and pressure P, the stress-energy tensor has the form

$$T^{\alpha\beta} = \left(\rho + \frac{P}{c^2}\right) u^\alpha u^\beta - P g^{\alpha\beta} \,, \tag{3.18}$$

with u the four-velocity of the fluid and $g^{\mu\nu}$ the inverse metric defined by $g_{\mu\sigma}\, g^{\sigma\nu} = \delta^\nu_\mu$.

To solve the Einstein equations for the FLRW metric, we need to compute the Einstein tensor and the stress-energy tensor ($T_{\mu\nu}$ - note the lower indices) within

that metric.Within the formalism used here, the Einstein tensor is derived by direct but lengthy calculation: From the metric and its derivatives follow the Christoffel symbols eq. (3.3), which allow to compute the Ricci tensor and scalar eq. (3.16) by using the definition of the Riemann curvature tensor eq. (3.17). This yields all components to assemble the Einstein tensor. The calculation in 3 + 1 dimensions can be found in most standard textbooks on General Relativity and in the more technical cosmology books including [5, 43]. Here, we show the slightly shorter calculation for 2 + 1 dimensions. Using polar coordinates, the metric and inverse metric read

$$g_{\mu\nu} = \begin{pmatrix} -c^2 & & \\ & \frac{a^2}{1-\kappa r^2} & \\ & & a^2 r^2 \end{pmatrix}, \qquad g^{\mu\nu} = \begin{pmatrix} -\frac{1}{c^2} & & \\ & \frac{1-\kappa r^2}{a^2} & \\ & & \frac{1}{a^2 r^2} \end{pmatrix}. \tag{3.19}$$

The non-zero Cristoffel symbols are

$$\begin{aligned} \Gamma^1{}_{10} = \Gamma^1{}_{01} = \Gamma^2{}_{20} = \Gamma^2{}_{02} &= \frac{\dot{a}}{a}\,, & \Gamma^0{}_{22} &= \frac{a\dot{a}r^2}{c^2}\,, \\ \Gamma^0{}_{11} &= \frac{a\dot{a}}{c^2(1-\kappa r^2)}\,, & \Gamma^1{}_{22} &= -r(1-\kappa r^2)\,, \\ \Gamma^1{}_{11} &= \frac{\kappa r}{1-\kappa r^2}\,, & \Gamma^2{}_{12} = \Gamma^2{}_{21} &= \frac{1}{r}\,. \end{aligned} \tag{3.20}$$

and the non-vansihing elements of the Ricci tensor are

$$R_{00} = -2\frac{\ddot{a}}{a}\,, \tag{3.21}$$

$$R_{11} = \frac{\ddot{a}a + \dot{a}^2 + \kappa c^2}{c^2(1-\kappa r^2)}\,, \tag{3.22}$$

$$R_{22} = \frac{r^2}{c^2}(a\ddot{a} + \dot{a}^2 + \kappa c^2)\,, \tag{3.23}$$

which results in the Ricci scalar

$$R = \frac{2}{c^2}\left(\frac{2\ddot{a}}{a} + \frac{\dot{a}^2}{a^2} + \frac{\kappa c^2}{a^2}\right). \tag{3.24}$$

The stress energy tensor must fulfill the same symmetry assumptions as the FLRW metric, namely homogeneity and isotropy. This implies a static fluid, since any fluid flow would define a direction and thus violate isotropy. The four-velocity then reduces to $u^\alpha = (c, 0, 0, 0)$ and the stress-energy tensor 3.18 takes the form

$$T_{\mu\nu} = \begin{pmatrix} \rho c^4 & 0 \\ 0 & P\, g_{ij} \end{pmatrix} \tag{3.25}$$

with g_{ij} the space-space part of the metric.

Inserting eq. (3.25), eq. (3.21) and eq. (3.24) in the Einstein equation, yields two different equations - one from the time-time element and one from the space-space elements. These are the *Friedmann equations* in 2 + 1 dimensions [46]

$$\left(\frac{\dot{a}}{a}\right)^2 = 8\pi G\rho - \frac{\kappa c^2}{a^2} + \Lambda c^2 \,, \tag{3.26}$$

$$\frac{\ddot{a}}{a} = -\frac{8\pi G}{c^2}P + \Lambda c^2 \,, \tag{3.27}$$

where $H = \dot{a}/a$ is named *Hubble parameter*. For comparison, the Friedmann equations in 3 + 1 dimensions are

$$\left(\frac{\dot{a}}{a}\right)^2 = \frac{8\pi G}{3}\rho - \frac{\kappa c^2}{a^2} + \frac{\Lambda c^2}{3} \,, \tag{3.28}$$

$$\frac{\ddot{a}}{a} = -\frac{4\pi G}{c^2}(\rho + 3P) + \Lambda c^2 \,. \tag{3.29}$$

They describe the evolution of the scale factor depending on the spatial curvature κ, the presence of a cosmological constant Λ and on the matter content of the universe. The matter is described by its density ρ and pressure P and different forms of matter are distinguished by their relation between these two quantities, the equation of state. For a fluid, the two Friedmann equations can be combined into a mass-energy conservation equation

$$\frac{\mathrm{d}}{\mathrm{d}t}(\rho a^d) = -\frac{P}{c^2}\frac{\mathrm{d}}{\mathrm{d}t}(a^d) \,, \tag{3.30}$$

with d the number of spatial dimensions. This equation directly describes how the density and pressure change during expansion. Depending on the relation of the different terms in the Friedmann equations, different expansion scenarios can be distinguished:

- A *de-Sitter universe* or *dark energy dominated universe* is an empty, flat universe with cosmological constant. In 2 + 1 dimensions, it expands with

  $$\frac{\dot{a}}{a} = \sqrt{\Lambda}c = \text{const.} \,, \tag{3.31}$$

  which corresponds to an exponential expansion

  $$a \propto t^{\sqrt{\Lambda}c} \,. \tag{3.32}$$

  The same is true for a 3 + 1-dimensional universe with the constant divided by $\sqrt{3}$. A scalar quantum field will lead to such an exponential expansion [47].

- A *matter-dominated* universe has no curvature and no cosmological constant. In the cosmological context a fluid is called 'matter' if it has a vanishing pressure $P = 0$. This is true the for collision-less dark matter and a reasonable approximation for 'ordinary' matter at low densities and temperatures. As can be derived with the conservation equation eq. (3.30), the energy density of this matter decreases with $\rho = \rho_0\, a^{-d}$ as the universe expands. Here, d denotes the number of spatial dimensions. This simply means that the same amount of matter is stretched over a larger space. Inserting these assumptions into the first Friedmann equation yields

$$\left(\frac{\dot{a}}{a}\right)^2 = \frac{8\pi G\rho_0}{a^2} \quad \Leftrightarrow \quad a(t) \propto t \qquad 2+1 \text{ dimensions}, \tag{3.33}$$

and

$$\left(\frac{\dot{a}}{a}\right)^2 = \frac{8\pi G\rho_0}{a^3} \quad \Leftrightarrow \quad a(t) \propto t^{2/3} \qquad 3+1 \text{ dimensions}. \tag{3.34}$$

- A flat *radiation dominated* universe contains only radiation. In the context of cosmology radiation denotes not only photons but all forms of highly relativistic matter. These have a pressure $P = \rho/d$. The density of radiation changes in an expanding space as $\rho = \rho_0\, a^{-(d+1)}$. The additional factor of $1/a$ is attributed to the redshift - a shift in wavelength, and hence energy, of relativistic matter due to the expansion. In the first Friedmann equation this leads to expansion

$$\left(\frac{\dot{a}}{a}\right)^2 = \frac{8\pi G\rho_0}{a^3} \quad \Leftrightarrow \quad a(t) \propto t^{2/3} \qquad 2+1 \text{ dimensions}, \tag{3.35}$$

and

$$\left(\frac{\dot{a}}{a}\right)^2 = \frac{8\pi G\rho_0}{a^4} \quad \Leftrightarrow \quad a(t) \propto t^{1/2} \qquad 3+1 \text{ dimensions}. \tag{3.36}$$

- Apart from matter and radiation, mixtures of the two can be imagined. Or a universe may contain strange forms of matter with a different relation between density and pressure. In general, the density of a fluid in d spatial dimensions with the equation of state $P = w\rho$ depends on the scale factor by

$$\rho = \rho_0\, a^{-d(1+w)}\,, \tag{3.37}$$

where w is called equation of state parameter. The corresponding time evolution of the scale factor is

$$a \propto t^{\gamma} \qquad \text{with} \qquad \gamma = \frac{2}{d(1+w)}\,. \tag{3.38}$$

- The best-fit model for our Universe allows for curvature, matter, radiation, and dark energy in the form of the cosmological constant. The parameters of the model as well as the Hubble parameter today can be determined by various observations. Among the most important ones are the observation of fluctuations in the cosmic microwave background, the measurement of the Hubble parameter using Type 1a supernovae as standard candles, the relative abundance of light elements in stars, and the distribution of the large scale structure of the Universe. Together they constrain the parameters to a universe with vanishing curvature, approximately 70% dark energy content, 25% dark matter, 5% ordinary matter and 0.01% radiation. Within the model, the expansion history of the Universe can be computed from the Friedmann equations: The early hot universe was in a radiation dominated era. As it expanded, radiation density decreased faster than matter density and radiation-domination gave way to a matter-dominated era. Both radiation and matter density decreased further until the cosmological constant becomes important and exponential expansion takes over. Currently, we are at the transition point from the matter domination into the exponential expansion of dark energy domination.

3.6 Particle production during inflation

On top of the homogeneous background, our Universe contains structures. These are observed as temperature fluctuations in the cosmic microwave background and grow into the large scale structure of the Universe today. The most widespread theory of the origin of this structure is an early rapid expansion of the Universe, directly after the Big Bang which is called *inflation* [5]. Such an expansion could be driven by a scalar quantum field [47], the *inflaton*. Usually, an expansion of at least 28 orders of magnitude (60e-folds) is assumed to take place in less than 10^{-32} s [5]. This vast expansion thins out all forms of matter and dilutes curvature until the observable universe is practically empty and spatially flat. However, the expansion itself leads to particle-pair creation within the inflaton field. This is the process of cosmological particle production that we will investigate with the phononic excitations of the Bose-Einstein condensate.

After inflation, the Universe is in an empty state, except for the excitations of the inflaton. It is commonly assumed that the inflaton field decays into ordinary matter and radiation via a parametric resonance in a process called *reheating*. This not only stops the exponential expansion but also refills the universe with matter and energy. During that process, the fluctuations of the inflaton field are translated into

fluctuations of matter. Thus it is possible that traces of the quantum state produced during inflation are still detectable in the observables of today's Universe [48].

One of these observables are the *baryon acoustic oscilations*. These are sound waves in the early universe that propagate in the mixture of ionized atomic nuclei, electrons and radiation. With the expansion of space, the temperature of the matter-radiation mixture decreases. Once the fluid has sufficiently cooled for atomic nuclei and electrons to combine to atoms, the radiation decouples from the matter and the universe is suddenly rendered transparent. The now freely-propagating radiation is observable today as the cosmic microwave background (CMB). Imprinted on this radiation is the density distribution of the matter-light mixture at the moment of its release; the fluctuation of the density lead to the temperature fluctuations of the radiation. The CMB thus contains a snapshot of the density distribution of the very early stage of the universe, around 380.000 years after the Big Bang. At the same time, the decoupling of matter and light abruptly stops the propagation of the sound-waves and freezes the density fluctuations. These are the seeds for the large-scale structure in the Universe. During the following 13.5 billion years, they have grown into galaxies, galaxy clusters, and the cosmic web. One distinctive feature in density correlation of the structure is still directly connected to the baryon accoustic oscillations. It is a correlation peak at a distance of 120 Mpc (MegaParsec). This marks the distance that spherical sound waves have traveled at the moment the CMB decoupled.

Especially the baryon acoustic oscillations may show traces of the original quantum state produces during inflation. Identifying and understanding these traces is an intriguing direction of research. While an analog system cannot capture the complex dynamics of the Universe, it helps to isolate and better understand processes like particle-pair creation. And it might even be possible to identify and test observables for the quantum processes in the very early Universe.

Chapter 4

Acoustic metric of a Bose-Einstein condensate

So far, we have introduced the FLRW metric of an expanding and curved spacetime and described a Bose-Einstein condensate and its perturbations. This chapter combines these two topics by deriving the acoustic analog of an FLRW metric in a Bose-Einstein condensate. For that purpose, it introduces a novel mapping between a mass-less, free, relativist scalar field and the phononic excitations of a condensate. Within the mapping, laboratory time and the coordinate time of the metric coincide, and a simple coordinate transformation relates spatial coordinates in the laboratory and in the analog FLRW metric. This makes the comparison between laboratory and simulated spacetime particularly straightforward. The mapping was developed by the theory side of our collaboration and is published in [41]. In this work, we only sketch the crucial steps and assumptions of the derivation and refer to this publication for the details. At the end of this chapter, section 4.2 discusses the potential and limitations of experiments in the analog system.

4.1 Derivation of the acoustic metric

The derivation of the acoustic metric starts from the action of a quasi-two-dimensional Bose-Einstein condensate of atoms with mass m

$$\Gamma[\Phi] = \int \mathrm{d}t\, \mathrm{d}^2 r \left(i\hbar\, \Phi^*(\partial_t + iA_0)\Phi - \frac{\hbar^2}{2m}(\vec{\nabla} - i\vec{A})\Phi^*(\vec{\nabla} + i\vec{A})\Phi - \frac{\lambda}{2}(\Phi^*\Phi)^2 \right), \tag{4.1}$$

with the $2d$-coupling λ introduced in eq. (2.7). The coupling is proportional to the s-wave scattering length a_s. Normally, the scattering length is written without the subscript s in the cold atom community. Unfortunately, the same symbol is used for the scale factor in an FLRW metric. For this work a, a_i, a_f denote the (initial and final) scale factor and a_s, $a_{s,i}$, $a_{s,f}$ the (initial and final) s-wave scattering length.

Within the action, the gauge field A is used to enforce a local $U(1)$ symmetry of the action (see [41] for details), and its zero-component is related to the trapping potential $V(t, \vec{r})$ and the chemical potential μ of the condensate by

$$A_0(t, \vec{r}) = \left(V(t, \vec{r}) - \mu\right)/\hbar \ . \tag{4.2}$$

For a vanishing chemical potential and $\vec{A} = 0$, the equation of motion for this action is the Gross-Pitaevski equation eq. (2.1) reduced to two dimensions. The Gross-Pitaevski equation describes the dynamics of a BEC in the limit of classical fields, and its solutions were discussed in more detail in chapter 2. It can be brought in a fluid-like form by using the Madelung representation, [49] which splits the background field into contributions of the density n_0 and the phase S_0

$$\phi_0(t, \vec{r}) = \sqrt{n_0(t, \vec{r})}\, e^{iS_0(t,\vec{r})} \ . \tag{4.3}$$

In the acoustic limit, the Gross-Pitaevski equation takes the form of a continuity and Euler equation

$$\partial_t n_0 + \vec{\nabla}(n_0 \vec{v}) = 0 \ , \quad \hbar\partial_t S_0 + V + \lambda n_0 + \frac{\hbar^2}{2m}(\vec{\nabla} S_0)^2 = 0 \ , \tag{4.4}$$

were the gradient of the phase can be defined as the velocity $\vec{v} = \frac{\hbar}{m}\vec{\nabla} S_0$. In the Euler equation, the quantum pressure term

$$q = -\frac{\hbar^2}{2m}\frac{\vec{\nabla}^2\sqrt{n_0}}{\sqrt{n_0}}, \tag{4.5}$$

was already neglected. This is plausible if the curvature of the wave function is small compared to its amplitude which is true for long-wavelength modes. As is described in section 2.3, long-wavelength perturbations have a linear dispersion relation. Thus neglecting the quantum-pressure term is equivalent to being in the acoustic regime.

In a second step, perturbations are added on top of the classical field solution. In previous works [32, 50], perturbations have been introduced as density and phase perturbations which can be directly inserted into the hydrodynamic equations. For

this work, a different choice of perturbation is used: The field ϕ is decomposed into the background field ϕ_0 and the two real-valued perturbations ϕ_1 and ϕ_2 defined as

$$\Phi(t,\vec{r}) = \phi_0(t,\vec{r}) + \frac{1}{\sqrt{2}}\left[\phi_1(t,\vec{r}) + i\phi_2(t,\vec{r})\right] \ . \tag{4.6}$$

To characterize the dynamics of the fluctuation, the action 4.1is expanded around the classical field limit up to second order in these perturbations. It takes the form $\Gamma[\Phi] = \Gamma[\phi_0] + \Gamma_2[\phi_1,\phi_2]$, where $\Gamma[\phi_0]$ describes the dynamics of the background field which were already discussed above. $\Gamma_2[\phi_1,\phi_2]$ only contains terms quadratic in the perturbations. It reads

$$\begin{aligned}\Gamma_2[\phi_1,\phi_2] = \int \mathrm{d}t\,\mathrm{d}^2r \Bigg\{ & \hbar\phi_2\partial_t\phi_1 - \frac{\hbar^2}{4m}\left[(\vec{\nabla}\phi_1)^2 + (\vec{\nabla}\phi_2)^2\right] \\ & -\frac{1}{2}\left(\hbar A_0 + \hbar^2\frac{\vec{A}^2}{2m}\right)(\phi_1^2+\phi_2^2) - \frac{\hbar^2}{2m}\vec{A}(\phi_1\vec{\nabla}\phi_2 - \phi_2\vec{\nabla}\phi_1) \\ & -\frac{\lambda}{2}(\phi_1,\phi_2)\begin{pmatrix} n_0 + \frac{1}{2}(\phi_0^*+\phi_0)^2 & \frac{1}{2}(\phi_0^*+\phi_0)(i\phi_0^*-i\phi_0) \\ \frac{1}{2}(\phi_0^*+\phi_0)(i\phi_0^*-i\phi_0) & n_0 + \frac{1}{2}(i\phi_0^*-i\phi_0)^2 \end{pmatrix}\begin{pmatrix}\phi_1\\ \phi_2\end{pmatrix}\Bigg\}.\end{aligned} \tag{4.7}$$

Since all terms linear in the perturbations cancel around the classical field limit, Γ_2 is the leading order term and defines the dynamics of the fluctuations. In the following, we will show that Γ_2 in the acoustic limit is equivalent to the action of a scalar field in a curved spacetime. The detailed derivation can be found in [41]; here, we only sketch the different steps and assumptions:

- An equivalent of the Madelung representation is introduced by the transformation

$$\phi_0 + \frac{1}{\sqrt{2}}\left[\phi_1 + i\phi_2\right] \to e^{-iS_0}\left(\phi_0 + \frac{1}{\sqrt{2}}\left[\phi_1 + i\phi_2\right]\right), \tag{4.8}$$

  which is inserted into eq. (4.7). At the same time, A_0 and $\vec{A}$ are adjusted such, that the transformation of Γ_2 is a local U(1) gauge transformation. In this gauge, the background field ϕ_0 becomes real. Note, that the perturbations ϕ_1 and ϕ_2 were defined as real fields before but become complex in this gauge. The hydrodynamic equations for the background field eq. (4.4) are used for further simplifications. After these steps Γ_2 is independent of the trapping potential and only the density and phase of the background field appear.

- For the implementation of the FLRW metric, we introduce an additional restriction on the density of the background field. Namely, that the density

of the background is static, i.e. that the velocity of the background field vanishes $\vec{v} = 0 = \vec{\nabla} S_0$. The more general case is discussed in [41]. With these assumptions, the effective action for the perturbations becomes

$$\Gamma_2[\phi_1, \phi_2] = \int \mathrm{d}t\, \mathrm{d}^2 r \left\{ -\frac{\hbar^2}{4m} (\vec{\nabla}\phi_2)^2 - \frac{1}{2}\phi_1 \left(2\lambda n_0 - \hbar^2 \frac{\vec{\nabla}^2}{2m} \right) \phi_1 - \hbar \phi_1 \partial_t \phi_2 \right\}. \tag{4.9}$$

- The acoustic approximation enters in the form $2\lambda n_0\, \phi_1^2 \gg \hbar^2/2m\, \phi_1 \nabla^2 \phi_1$ which is valid for small momenta/long wavelength. In this regime, the latter term, which is the kinetic term for ϕ_1, can be neglected. Then, thee action does not contain any derivatives of the field ϕ_1 which makes the next step possible.

- In the acoustic approximation, the field ϕ_1 can be integrated out with a Gaussian integral.[1] With defining the field $\phi \equiv \phi_2/\sqrt{2m}$, the action takes its final form

$$\Gamma_2[\phi] = \frac{\hbar^2}{2} \int \mathrm{d}t\, \mathrm{d}^2 r \left\{ \frac{1}{c_s^2} (\partial_t \phi)^2 - (\vec{\nabla}\phi)^2 \right\}, \tag{4.10}$$

  where we identified the time and radius-dependent speed of sound (see section 2.3 for comparison)

$$c_s^2(t, r) = \frac{\lambda(t)\, n_0(t, \vec{r})}{m}\ . \tag{4.11}$$

  The integral also defines a relation between ϕ_1 and ϕ_2

$$\phi_1 = -\frac{\hbar}{2\lambda(t) n_0(r)} \partial_t \phi_2 = -\frac{\hbar}{2\lambda(t) n_0(r)} \frac{1}{\sqrt{2m}} \dot{\phi}\ , \tag{4.12}$$

  which connects ϕ_1 to the time derivative of the scalar field $\dot{\phi}$. This will become important for deriving suitable experimental observables in chapter 10.

The action 4.10 is equivalent to the action of a free, mass-less, relativistic scalar field in a curved spacetime

$$\Gamma_2[\phi] = -\frac{\hbar^2}{2} \int \mathrm{d}t\, \mathrm{d}^2 r\ \sqrt{g}\, g^{\mu\nu} \partial_\mu \phi\, \partial_\nu \phi\ , \tag{4.13}$$

[1] The integration is performed in the partition function $Z \propto e^{i\Gamma_2}$ from which observables are derived. The integration over ϕ_1 will lead to an additional factor in front of the partition function. However, all observables need to be normalized by the partition function and this factor is be canceled.

with the acoustic metric

$$\left(g_{\mu\nu}\right) = \begin{pmatrix} -1 & 0 \\ 0 & \frac{1}{c_s^2}\delta_{ij} \end{pmatrix} , \tag{4.14}$$

and $g = g_{\mu\nu}\, g^{\mu\nu}$. Thus, the perturbations ϕ of a background condensate exhibit the same dynamics as a quantum field in a curved spacetime. It remains to be checked that the correct commutation relations are fulfilled between the field ϕ and its conjugate momentum

$$\pi(t, u, \varphi) = \frac{\delta\Gamma_2[\phi]}{\delta\dot{\phi}} = \hbar^2 \sqrt{g}\dot{\phi} \, . \tag{4.15}$$

The commutation relations define the quantization of the action. In an experiment, we can only simulate quantum effects, if the fluctuation of the condensate indeed fulfill this quantization. Here, we will only state that the commutation relations are indeed correct and refer once more to [41] for the calculation.

Later we will work with a circular symmetric condensate, for which polar coordinates are a natural choice. In these coordinates, the line element of the acoustic metric is

$$\begin{aligned} \mathrm{d}s^2 = g_{\mu\nu}\mathrm{d}x^\mu \mathrm{d}x^\nu &= -\mathrm{d}t^2 + \frac{1}{c_s^2(t,r)}\left(\mathrm{d}r^2 + r^2\mathrm{d}\varphi^2\right) \\ &= -\mathrm{d}t^2 + \frac{m}{\lambda(t)\, n_0(r)}\left(\mathrm{d}r^2 + r^2\mathrm{d}\varphi^2\right) \, . \end{aligned} \tag{4.16}$$

The metric can be made time-dependent via the coupling $\lambda(t)$ and thus the s-wave scattering length. This is used to realize an expanding spacetime in chapter 10. The curvature of the spatial part of the metric can be designed using the radial dependence of the density profile $n_0(r)$ as is discussed in chapter 8.

4.2 Limitations of analog models

Simulating an FLRW metric in a Bose-Einstein condensate is an enticing tool. However, it has its limitations, and it is crucial to keep in mind what such a simulation can and cannot achieve. First of all, it cannot implement general relativity as was already discussed in chapter 3 since the back-reaction of matter on the curvature of spacetime is not contained in the analog systems. Furthermore, the analogy between the universal speed of light in a spacetime and the propagation speed of excitations in the analog system is imperfect. Excitations travel at a uniform speed only in

the limit of large wavelengths in the acoustic regime. For larger wavelengths, the excitations of a condensate are no longer collective phononic excitations. Instead, they are particle-like with a quadratic dispersion relation (see section 2.3). For these high-momentum modes, the analogy between the dynamics of excitations in a condensate and the dynamics of a scalar field breaks down. Later in this work, when simulating particle-pair creation in an expanding spacetime in chapter 10, this must be taken into account for choosing suitable experimental parameters.

CHAPTER 5

Atoms, light, and magnetic fields - the experimental toolkit

Atoms can be trapped, cooled, and controlled using laser light and magnetic fields. This chapter introduces the underlying physical processes and describes how they are used experimentally. It is based on [51, 52] if not mentioned otherwise. A strong focus is on the atom species used for the experiments in this work, potassium-39.

The first section introduces the basic properties of potassium-39 including its level structure. Section 5.4 then describes the property that makes potassium-39 so desirable as an atom: its broad Feshbach resonance. Afterwards section 5.2 and section 5.3 discuss light and magnetic forces, and section 5.5 gives a general overview of how these forces are used experimentally. Section 5.6 and section 5.7 describe the types of conservative traps in more detail, namely magnetic traps and dipole traps. The latter section also introduces the trap geometries relevant for this work - a focused Gaussian beams and a pancake trap. The remaining chapters cover the different cooling methods needed to creation of a Bose-Einstein condensate of potassium-39. These are magneto-optical traps in section 5.8, Sisyphus cooling and grey molasses cooling in in section 5.9 and section 5.10 and evaporative cooling in section 5.11. Finally, section 5.12 and section 5.13 describe imaging of the atomic density distribution in general and for the special case of potassium-39 at high magnetic fields.

5.1 Basic properties of potassium-39

Potassium-39 is a bosonic alkali atom with a nuclear spin of $I = 3/2$ and the typical level structure shown in fig. 5.1. Its ground state is the $^2S_{1/2}$ state. The first excited state is divided by the fine structure splitting into the $^2P_{1/2}$ and $^2P_{3/2}$ states. The transition frequencies between the ground state and these excited states are 770.108 nm (D1-line) and 766.70 nm (D2-line), respectively. The coupling between nuclear spin I and electron spin J to a total spin F leads to the further hyperfine splitting of ground and excited states. The ground state is split into the $F = 1$ and $F = 2$ states with a frequency splitting of 461.7 MHz. The excited states are also split in two ($F = 1$, $F = 2$ for $^2P_{1/2}$) and four hyperfine states ($F = 0$ till $F = 3$ for $^2P_{3/2}$). A special property of potassium is that the hyperfine splitting of the excited states – especially of the $^2\mathrm{P}_{3/2}$ state – is on the order of the natural linewidth of the transitions $\Gamma/2\pi \approx 6\,\mathrm{MHz}$ [53, 54]. It is impossible to address a single hyperfine level by an optical transition selectively. This has immediate consequences for the cooling in a magneto-optical trap (MOT) and an optical molasses as is discussed in section 5.8 and section 5.10. In analogy to Rubidium, the transition from the $F = 2$ ground state to one of the excited states is called *cooling transition* and the transition from the $F = 1$ ground state *repumping transition*. Lasers with these frequencies are be called *cooler* and *repumper* in the scope of this work.

5.2 Breit-Rabi diagram and magnetic forces

Neutral atoms often have an intrinsic magnetic dipole moment, responsible for the Zeeman splitting of the atomic levels in a magnetic field B. For non-vanishing magnetic fields, a level with total spin F is split into $2F + 1$ magnetic substates with $m_F \in [-F \dots F]$, as their degeneracy is broken. Depending on the magnetic substate, the atom's energy level is either lowered, unaffected, or increased by the presence of the magnetic field. The Zeeman splitting is approximately linear in B in weak magnetic fields. For stronger magnetic fields, the interplay between nuclear spin I, the total angular momentum of the electron J, and magnetic field changes. At very high fields, the electron spin and nuclear spin couple independently to the magnetic field (Paschen-Back regime) instead of first forming a total spin F. At intermediate magnetic fields, the atom is in neither of the regimes. At such intermediate fields, neither m_F nor m_I and m_J are good quantum numbers as they do not coincide with eigenenergy states of the atom. The energy states can be derived by diagonalization of the full interaction Hamiltonian, resulting in the Breit-Rabi formula [53, 55–57]. The corresponding eigenvectors indicate the decomposition of the energy states into

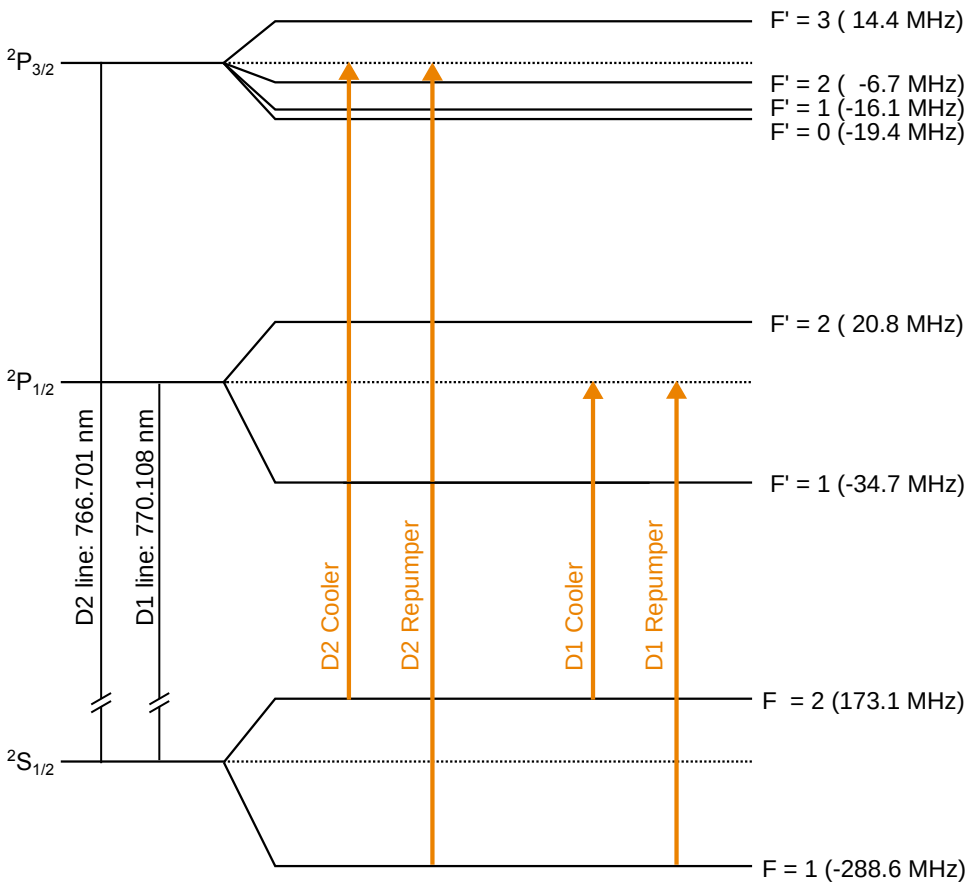

Figure 5.1: Potassium level scheme The ground state of potassium is the $2S_{1/2}$ state. The electron spin-orbit coupling leads to the fine structure splitting of the excited state into $^2P_{3/2}$ and $^2P_{1/2}$; the respective transitions are called D2 and D1 lines. The coupling between electron angular momentum and nuclear spin $I = 3/2$ leads to a further splitting, the hyperfine splitting. The two fine-structure levels of the ground state are split by 461.7 MHz, the excited states show only a small splitting compared to the natural linewidth of 6 MHz. In analogy to the cooling lights of Rubidium in a magneto-optical trap, the transitions from the upper/lower ground state level to the excited states are called cooler/repumper transitions.

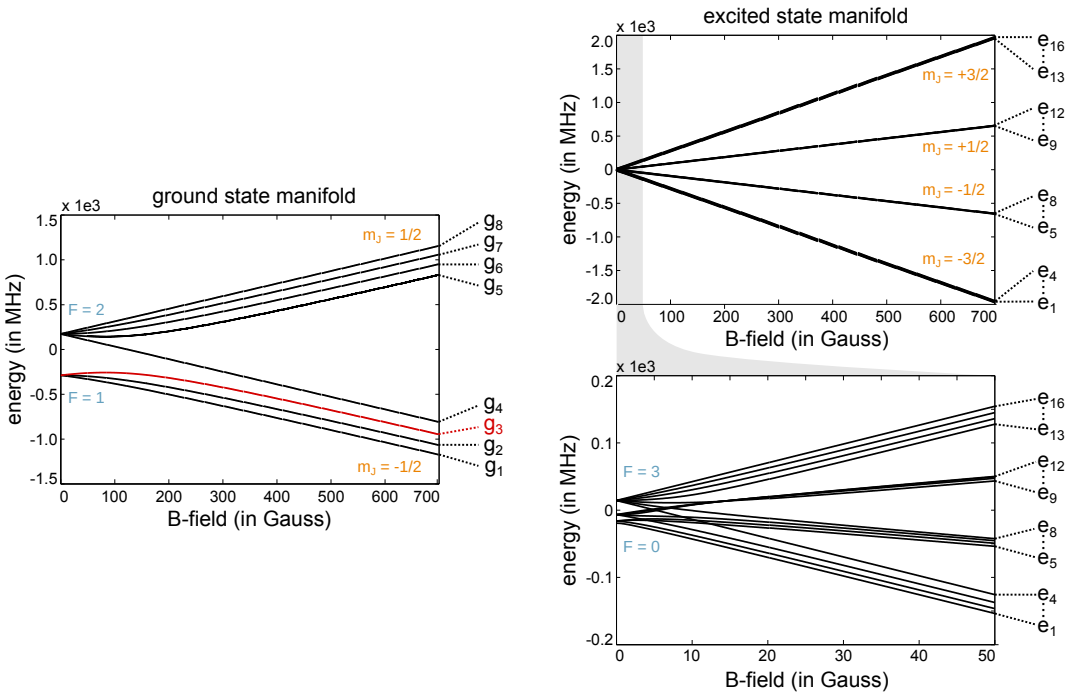

Figure 5.2: Breit-Rabi diagram. Under the influence of a magnetic field, the magnetic substates are no longer degenerate. Their energy splitting is shown for the ground state manifold (left-hand side) and the $^2P_{3/2}$ excited state (right-hand side). At zero magnetic field, the eigenenergy states g_1 to g_8 and e_1 to e_16 are $|F, m_F\rangle$ states. At high magnetic field (Paschen-Back regime), the eigenenergy states are $|m_J, m_I\rangle$ states. This regime is already reached for the excited state at the magnetic fields shown here; for the ground state manifold, this is only the case for higher magnetic fields. In between regimes, the eigenenergy states are a superposition on either basis. The Bose-Einstein condensate discussed in this work is in the g_3 ground state (red) which is the $F = 1, m_F = -1$ state and becomes the $m_J = -1/2, m_I = +1/2$ at very high magnetic fields.

the $|F, m_F\rangle$ or $|m_J, m_I\rangle$ states.

Figure 5.2 shows the Breit-Rabi diagram – the level structure of potassium-39 in dependence on the magnetic field – for the ground state manifold and the $^2P_{3/2}$ excited state manifold (D2 line). The states have the general names g_1 to g_8 and e_1 to e_{16} since they cannot be associated with quantum numbers over the entire range of the magnetic field. At zero magnetic field the states g_1 to g_3 correspond to the states with $F = 1$ and $m_F = +1, 0, -1$ state and g_4 till g_8 to the states with $F = 2$ and $m_F = -2, -1, 0, 1, 2$, respectively. At very high magnetic fields, the states g_1 to g_4 correspond to the states $m_J = -1/2$ and $m_I = +3/2, +1/2, -1/2 - 3/2$ and the states g_5 to g_8 to the states $m_J = +1/2$ and $m_I = -3/2, -1/2, +1/2 + 3/2$.[1] In the excited state manifold a similar identification is possible (see fig. 5.2, more details can be found in [58–61]).

In an inhomogeneous magnetic field, the level structure of an atom becomes position-dependent. This directly translates into a potential energy landscape in which the atom moves - trading kinetic energy against the potential energy of its internal state. Gradients in the potential result in a force

$$\vec{F} = \vec{\nabla}\left(\vec{\mu} \cdot \vec{B}\right) , \tag{5.1}$$

with $\vec{\mu}$ the magnetic dipole moment of the atomic substate. The magnetic moment is given by the slope of the Breit-Rabi diagram at the respective magnetic field. The sign of the slope determines whether an atom is pulled into regions of high magnetic fields (*high field seeker*) or pushed into regions of low magnetic field (*low field seeker*). If the state's energy decreases with a higher magnetic field, it is a high-field-seeking state and vice versa.

5.3 Atom-light interaction and light forces

The interaction of atoms with light can be conceptually separated into off-resonant and resonant interactions. Close to the resonance, the light induces transitions between the internal states of the atom. Far away from resonance, the interaction mainly results in a shift of the internal energy levels. A semi-classical model already provides a complete mathematical treatment. Here, the atom is quantized and a classical oscillating electric field describes the light. For a two-level system, this results in the optical Bloch equations (see for example [52]), which contain both resonant and off-resonant interactions. However, an intuitive understanding is more

[1] Note, that $m_F = m_I + m_J$ is always fulfilled. This is very helpful for tracing states from low to high magnetic fields.

easily reached in separate pictures for the two forces. For the off-resonant interaction, the main features can be understood with a classical driven harmonic oscillator. The resonant interaction can be best visualized with the absorption and emission of photons by the atom.

Before taking a closer look at these two regimes, we first take a look at the conditions for a resonance. The first condition concerns the frequency of the light. The energy of a photon must be the same as the energy difference between the ground and excited state. In addition, the ground and excited state need to have a non-vanishing transition dipole element. A third condition poses requirements on the light's angular momentum, which is essential if the magnetic-substates are non-degenerate. The magnetic substates themselves correspond to an angular momentum of the atom's internal state. The difference in angular momentum between ground and excited states needs to be provided by the angular momentum of the absorbed photon and thus the light's polarization. The latter two requirements are reflected in the transition rules. The strength of a transition – and whether it is allowed at all – is determined by the transition dipole element and the angular-momentum addition rules described by the Clebsch-Gordon coefficients. Transition strengths at zero magnetic field are listed in standard textbooks on atomic physics [52]. For potassium-39, detailed calculations of the allowed transitions at higher magnetic fields can be found in [58, 60]. These rules will become important again for the imaging scheme described in section 5.13. With the occurrence of resonances defined, we can begin the discussion of the forces caused by atom-light interaction.

Close to resonance, the atom-light interaction is dominated by the absorption and emission of photons. Whenever a photon is absorbed, its momentum $p = \hbar\vec{k}$ is transferred to the atom due to momentum conservation. During the emission of a photon, the atom receives a momentum opposite to the one of the photon. For absorption and consecutive stimulated emission, the effect of both processes cancels, and the atom remains unaffected. However, if the emission is spontaneous, the photon is emitted in a random direction. For many absorption and spontaneous emission cycles, absorption results in a net momentum transfer, while the momentum kicks due to spontaneous emissions average to zero. The combination of absorption and spontaneous emission thus leads to an effective force directed in the propagation direction of the laser beam. This force is called *light pressure force* or *scattering force*.

A side-effect of the scattering force is a heating effect. The momentum kicks due to spontaneous emission can be interpreted as a random walk in momentum space. This broadens the velocity distribution of an atom cloud similar to an increase in temperature. This heating process sets a lower limit to temperatures achievable by

methods using the scattering force. A lower fundamental temperature limit is set by the energy of a single photon kick, called the *recoil limit*.

Far away from a resonance, in a purely classical picture, the oscillating electric field of the light polarizes the atom by inducing an electric dipole moment. The interaction between the light field and the induced dipole changes the energy of the combined system. This energy shift can be positive or negative, depending on the relative orientation between the external field and the induced electric dipole in the atom. The orientation can be understood by the dynamics of a driven harmonic oscillator. The eigenfrequency of the oscillator is the frequency of the atomic resonance ω_0, and the frequency of the light ω sets the driving force. For red-detuned light – light with a frequency below the atomic resonance – the induced electric dipole can perfectly follow the driving, leading to a decrease in energy. For blue-detuned light – light with a frequency above the atomic resonance – the induced dipole moment lags behind the driving force by phase of π; its orientation is always opposite to the 'ideal' one, leading to an increase in energy. In both cases, the energy shift is proportional to the intensity of the irradiating light.

In an inhomogeneous light field, this creates a potential landscape called the *dipole potential*. The negative gradient of the potential is the corresponding *dipole force*. A quantitative analysis within the harmonic oscillator picture can be found in [62] and semi-classical treatment yields in the same result. The dipole potential is

$$U_{\mathrm{dip}}(\vec{x}) = -\frac{3\pi c^2}{2\omega_0^3}\frac{\Gamma}{\Delta}I(\vec{x}) \,, \tag{5.2}$$

with $\Delta = \omega_0 - \omega$ the detuning, $I(\vec{x})$ the intensity of the light, and Γ the damping of the harmonic oscillator. The origin of the damping cannot be understood in the classical picture. For a quantum system, it is the natural linewidth of the transition due to spontaneous decay. Also, a real atom has more than one resonance, which must be considered. For potassium-39, for optical and infrared light, the relevant transitions are the D1 and D2 lines (see section 5.1). For linearly polarized light, the dipole potential is

$$U_{\mathrm{dip}}(\vec{x}) = -\frac{\pi c^2 \Gamma}{2\omega_0^3}\left(\frac{2}{\Delta_2} + \frac{1}{\Delta_1}\right)I(\vec{x}) \,, \tag{5.3}$$

with Δ_2 and Δ_1 the detunings from the D2 and D1 line, respectively [62].

5.4 Atom-atom interaction and Feshbach resonances

Next to magnetic and light forces, one more tool is available to manipulate atoms. That is the interaction between the atoms themselves. A detailed discussion of the scattering can be found in [51]. For a neutral atom, the interaction consists of the attractive van der Waals interaction and the repulsion between the atomic nuclei at small distances. These effects lead to the combined potential for the atom interaction shown in fig. 5.3. The scattering process between two atoms is described by the solutions of the Schrödinger equation in this potential. The solutions are a superposition of an ingoing plane wave and outgoing waves. The latter are decomposed into spherical harmonics to capture the spherical symmetry of the atomic potential. For ultracold atoms, only the spherical harmonic with vanishing angular momentum (s-wave) has a relevant contribution. It is parametrized by a single parameter a_s – the s-wave scattering length – related to the relative phase between the ingoing and outgoing wave. In this regime, the scattering problem is equivalent to an interaction with a delta function that leads to the same phase shift as the atomic potential.

The scattering process is reduced to the phase change of the wave function during the interaction. It depends on the exact shape of the atomic interaction potentials and the internal magnetic states of the interacting atoms. These parameters determine the background scattering length a_{bg} of the interaction. The scattering length changes drastically at specific magnetic fields, a phenomenon known as a Feshbach resonance. A detailed treatment can be found in [63]. The underlying phenomenon is related to the bound states (molecular states) in the interaction potential. Two initially unbound atoms are forbidden from permanently entering into these states due to momentum and energy conservation. However, if their energy is close to the molecular state, they can form a temporary bound state before separating. In the wave picture, this temporary bound state strongly influences the phase of the outgoing wave and hence the s-wave scattering length. For ultracold atoms, the combined energy of the atoms is always close to zero. The energy of the molecular state depends on the magnetic field and can be shifted by applying such a field. Feshbach resonances occur at the magnetic field value B_0 where the energy level of the molecular state is the same as the energy of the initially free incoming atoms. Around the resonance, the s-wave scattering length changes as

$$a_s(B) = a_{s,bg}\left(1 - \frac{\Delta}{B - B_0}\right), \tag{5.4}$$

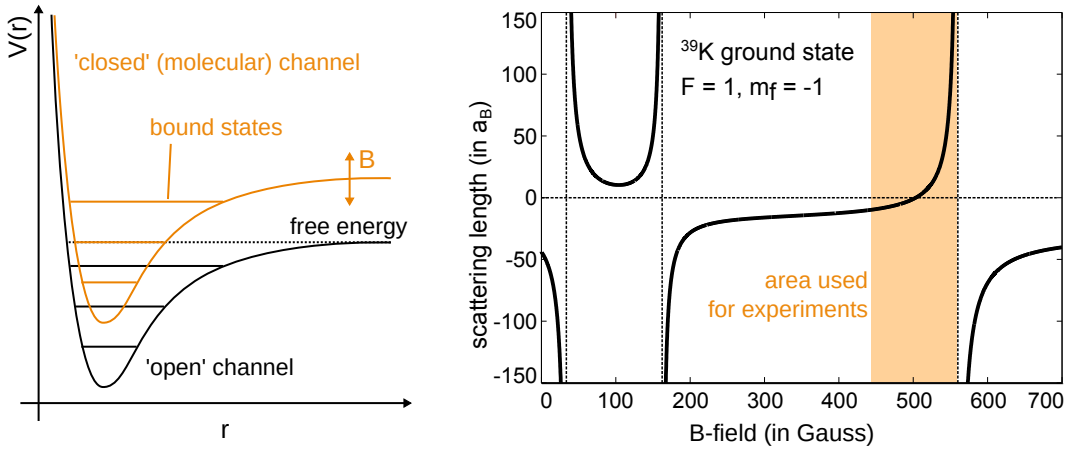

Figure 5.3: Feshbach resonances - mechanism and potassium-39 resonances. The left-hand side shows the interaction potential between two neutral atoms. The interaction potential of two unbound atoms is the open channel (black potential). The closed channel describes a molecular state of the atoms (orange potential). A magnetic field shifts the relative energies between the open and the closed channel. When the energy of a bound state in the closed channel coincides with the combined energy of the free atoms, a Feshbach resonance appears. Even though the atom pair can not enter the molecular state due to momentum conservation, it can form a temporary bound state. This prolonged interaction changes the phase of the wave function during the interaction and thus the s-wave scattering length. The right-hand side shows the Feshbach resonances for the $F = 1, m_F = -1$ state (at low magnetic field) of potassium-39. Especially the broad resonance at 562 G allows a fine adjustment of the scattering length. Within the area marked in orange, adjustments of the scattering length between large positive values and negative values are possible.

with a_{bg} and B_0 the aforementioned background scattering length and magnetic field position of the resonance and Δ the width of the resonance.

The $F = 1$ ground state of potassium-39 has three Feshbach resonances at moderate magnetic fields, two of which are broad. The existence of these resonances is the property that makes potassium-39 a versatile candidate for ultra-cold atom experiments. The exact location of the resonances is slightly different for the different magnetic substates. The intra-species Feshbach resonances for the $|\, F = 1, m_F = -1 \,\rangle$ states (at zero magnetic field) are shown in fig. 5.3. Experiments will be performed on the low-magnetic field side of the resonance at $B_0 = 562.2$G. Due to its width of $\Delta = 55$G, a fine experimental adjustment of the scattering length is possible in a range from slightly negative to large positive values.

5.5 Assembling the tool kit

In ultracold atom experiments, forces on atoms are used for trapping and cooling. Both the magnetic and the dipole force can only be used for trapping. They both lead to a conservative energy landscape where the atoms can be confined. Heating effects in this trap are minimal since the forces do not depend on the scattering of photons. Thus, these traps can store atomic clouds with temperatures far below the recoil limit. Especially blue-detuned dipole traps combine complex trap geometries with minimal heating. The third force, the scattering force, has a dissipative component used for cooling. Cooling schemes employ this force by making photon absorption dependent on the atom's velocity. Combinations of cooling and trapping with the scattering force are possible if the photon absorption becomes position-dependent. More advanced cooling schemes combine dipole or magnetic forces with photon scattering and manage even to break the recoil limit. Finally, there is one cooling scheme – evaporative cooling – that depends only on atom-atom interaction and has no fundamental physical limit on achievable temperatures. The following sections will describe both magnetic and dipole traps and a selection of cooling schemes necessary to create a potassium-39 Bose-Einstein condensate.

5.6 Magnetic traps

Magnetic traps are solely based on the magnetic force described earlier in section 5.2. The traps consist of an inhomogeneous magnetic field in which the atoms are confined. The internal magnetic moment of the atomic state determines whether an atom is pulled into regions of high magnetic field (high-field seekers) or pushed into regions of low magnetic field (low-field seekers, see section 5.2). In principle, Earnshaw's theorem forbids the stable, static trapping of charges by magnetic fields, and the theorem can be extended to magnetic dipoles. However, stable trajectories are possible around a magnetic minimum, and low-field seekers can be trapped. For the $F = 1$ ground state of potassium at small magnetic fields, the $m_F = 1$ (g_1) and $m_F = 0$ (g_2) states are high-field seekers and the $m_F = -1$ (g_3) state is a low-field seeker (see fig. 5.2). Thus, only the $m_F = -1$ state will be caught in a magnetic trap.

A rudimentary magnetic trap is created by a pair of coils with opposite currents, similar to an anti-Helmholtz pair. Magnetic traps are typically not deep enough to catch room-temperature atoms for experimentally realistic coil geometries and electrical currents. However, atoms pre-cooled by a magneto-optical trap (see section 5.8) or even an optical or grey molasses (see section 5.10) can be caught. The anti-Helmholtz configuration has a significant disadvantage: the magnetic field

strength vanishes at the trap's center. At that point, the magnetic substates of an atom become degenerate, and flips from one state to the other are possible. In particular, an atom might switch from being in a low field seeking state to being a high field seeker (Majorana spin-flip). Such a flip results in the atom being ejected from the trap. For atoms loaded from a MOT or molasses, this effect is small. But it becomes a significant loss channel if temperatures are further decreased, and densities rise around the magnetic zero-point. More complex magnetic traps avoid the zero-point by adding a rotating magnetic field (TOP trap). This time-dependent offset field moves the zero point around a time-averaged center of the trap. Alternatively, more refined coil geometries add a bias field to the field gradient (Ioffe-Pritchard traps or Cloverleaf traps) [64].

For cooling of potassium-39, the anti-Helmholtz configuration is sufficient. Very high densities in a magnetic trap cannot be reached because evaporative cooling in the magnetic trap is not possible for potassium-39 (see section 5.11 for details). The trap is only used for temporary confinement, selection of one atomic state, and compression of the cloud. For this, the magnetic zero-point of the anti-Helmholtz configuration is not restricting.

5.7 Dipole traps

Just like magnetic traps are based on the magnetic force in an inhomogeneous magnetic field, dipole traps are based on the dipole force in an inhomogeneous light field far detuned from an atomic resonance (see section 5.3). Dipole traps can realize much smaller structures and thus more complex trap geometries than the broad and smooth magnetic traps. The simplest trap geometry is a focused *Gaussian laser beam*. For red-detuned light, atoms are caught in the region of the highest intensity around the focus. Due to the wave properties of light, a small focus (strong localization) leads to a momentum uncertainty and hence divergence of the beam on both sides of the focus. The intensity profile of such a beam is depicted in fig. 5.4. In cylindrical coordinates (r, φ, z) it is described by

$$I(r,z) = I_0 \left(\frac{w_0}{w(z)}\right)^2 \exp\left(-\frac{2r^2}{w(z)^2}\right) , \tag{5.5}$$

where $w(z)$ characterizes the radial size of the beam at position z, and w_0 is the radial size at the position of the focus, called *beam waist*. It is the only free parameter in a Gaussian beam. Along the beam, in the z direction, the size of the focus region is

described by the *Rayleigh range*

$$z_R = \frac{\pi w_0^2}{\lambda} , \tag{5.6}$$

defined as the distance z at which $w(r) = \sqrt{2}\, w_0$. For small waists, the Rayleigh range is sufficiently small that a single beam can confine atoms in all three dimensions. The Rayleigh range is large for broader waists, and atoms can escape the trap along the beam direction. In this case, trapping in three dimensions is commonly achieved by crossing two or more beams. Experimentally, a laser beam emitted from an optical single-mode fiber has a Gaussian shape, [2] and a single lens creates the focus. The focal length and size of the initial beam determine the beam waist; a tight focus is reached with a small focal length or a large initial beam. Asymmetric focus geometries are also possible. For example, a cylindrical telescope can broaden the initial beam along one direction before the beam is focused. The focus region is tighter along the initially broadened direction but remains unchanged in the orthogonal direction. Achievable waists sizes are limited by aberrations of the lenses and deviations from the Gaussian beam profile. For this work, beam waists down to $5\,\mu$m are realized with Gaussian beams.

A trap with tight confinement in only one direction can be achieved by the interference of two laser beams. For that purpose, two collimated, coherent laser beams are crossed under an angle α (see fig. 5.4). In the overlap region, the beams interfere and form a characteristic pattern. Without loss of generality, the propagation direction of the two beams is described by the k-vectors

$$\vec{k}_1 = \frac{2\pi}{\lambda}\left(\cos\left(\frac{\alpha}{2}\right)\vec{e}_z + \sin\left(\frac{\alpha}{2}\right)\vec{e}_x\right) , \tag{5.7}$$

$$\vec{k}_2 = \frac{2\pi}{\lambda}\left(\cos\left(\frac{\alpha}{2}\right)\vec{e}_z - \sin\left(\frac{\alpha}{2}\right)\vec{e}_x\right) . \tag{5.8}$$

The collimated laser beams can be approximated by plane waves, which results in the intensity field

$$I(x,z,\varphi) = \left|\sqrt{I_1}\,\exp\left(i(\omega t - \vec{k}_1\vec{x})\right) + \sqrt{I_2}\,\exp\left(i(\omega t - \vec{k}_2\vec{x} + \varphi)\right)\right|^2 \tag{5.9}$$

$$= I_1 + I_2 + 2\sqrt{I_1 I_2}\cos\left[\frac{4\pi}{\lambda}\sin\left(\frac{\alpha}{2}\right)x + \varphi\right] , \tag{5.10}$$

[2] The Gaussian mode is the lowest mode of the electrical field in the fiber. For single-mode fibers, all other modes are suppressed.

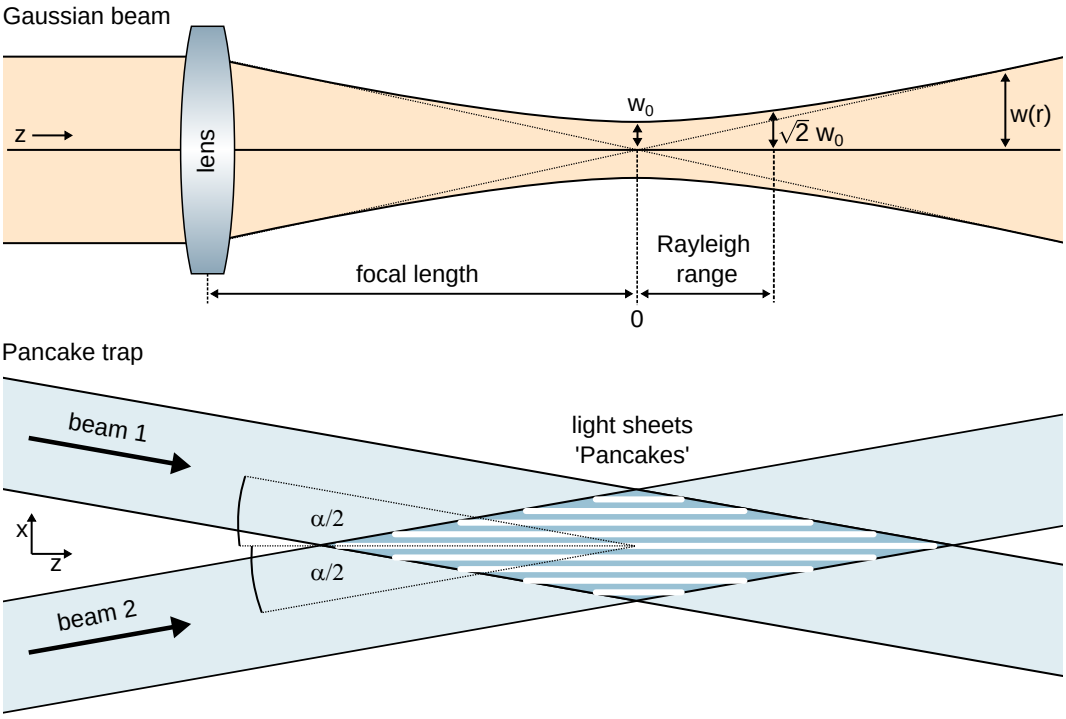

Figure 5.4: Dipole trap geometries Dipole traps are often realized by a focused laser beam (orange beam). The size of the inital collimated beam and the focal length of the focusing lens determine the beam waist w_0 at the focus. Along the propagation direction of the beam, the Rayleigh range is defined as the distance where the beam size increased to $\sqrt{2}w_0$. It thus characterizes the divergence of the beam. A trap with tight confinement in only one direction can be realized with a pancake interferometer (blue beams). Two coherent laser beams are crossed under an angle α. In the overlap region, the light interferes and forms light sheets stacked along the x direction, similar to a stack of pancakes. In such a trap, only the x direction is tightly confined.

with I_1 and I_2 the intensities of the single beams and φ the phase difference between both beams. This intensity pattern describes sheets of lights extended in the y-z plane and stacked in the x-direction. These sheets resemble a stack of pancakes and, consequently, this trap is often called a *pancake trap*. The spacing Δx between sheets depends on the wavelength of the trapping light and the angle between the beams

$$\Delta x = \frac{\lambda}{2} \frac{1}{\sin(\alpha/2)} \, . \tag{5.11}$$

In the limit of counter-propagating beams, $\alpha = \pi$, the spacing is $\Delta x = \lambda/2$ as expected from a standing wave or lattice configuration. For smaller angles, the spacing increases. For light red-detuned to an atomic resonance, atoms are caught in the intensity maxima of the light sheets; for blue-detuned light, atoms are caught between the sheets. The latter has the advantage that the atom cloud is confined in a low-intensity region. The intensity even drops to zero if the beams have equal intensity $I_1 = I_2$. In such a region, residual photon scattering is minimal, and heating effects are reduced significantly.

The relative phase φ between beams shifts the interference pattern along the z-axis. Experimentally, the phase is used for precise adjustment of the position of the light sheets. However, the phase is also prone to disturbances ranging from temperature changes in optical fibers to air fluctuations along the beam path. Phase noise results in a random shaking of the light sheets, which heats the atom cloud. Luckily, the relevant quantity is not noise on a global phase but the noise on the relative phase between the two beams. Relative noise is reduced in a compact, free-space, symmetric interferometer setup located as close to the trap region as possible. In such a setup, most of the phase noise simultaneously influences both beams such that the relative phase remains unaffected.

For both Gaussian beams and the pancake trap, a region around the potential minimum is well approximated by a harmonic trap with trap frequency $\omega = 2\pi f$. To characterise traps, these frequencies can be measured experimentally.

Especially versatile traps are realized with a Digital Micromirror Devise (DMD), which projects arbitrary two-dimensional light patterns [61, 65, 66]. Such a trap is not described in detail here as it is not used in the experiments described in this work. However, it is an essential tool for future experiments on the dynamics of quantum fields in analog curved spacetimes.

5.8 Magneto-optical trap

A magneto-optical trap (MOT) is the first stage of a cold atom experiment. It can cool and confine atoms that are initially at room temperature or even higher temperatures. An MOT uses the scattering force to combine a cooling process with spatial confinement. For cooling, the force needs to counteract the atoms' movement. In one dimension, this is realized in a setup of two counter-propagating laser beams, which are red-detuned to an atomic resonance. The movement of an atom leads to a Doppler-shift that is opposite for the two beams. Suppose the atom moves with the propagation direction of the laser, the frequency shifts away from resonance. The other way around, if the atom moves against the propagation direction of the laser, the frequency is shifted towards the resonance. Thus, the atom scatters more photons from the laser counter-propagating to its movement, resulting in a force opposite to its velocity. By combining three pairs of counter-propagating lasers, atoms can be slowed in all three spatial directions. This cooling process is called *Doppler cooling*. In the absence of spatial confinement, such a cooling setup is called *optical molasses*, inspired by the velocity dependence of the force similar to friction.

Spatial trapping is achieved by a carefully chosen combination of magnetic fields and polarisation of the laser lights. The working principle is best understood for an atomic transition from a ground state with a vanishing magnetic moment $F = 0$ to an excited state with a magnetic moment of $F = 1$ (see fig. 5.5). A magnetic field with a zero-point at the center is added to the previously described one-dimensional setup with two counter-propagating, red-detuned laser beams. From the center, the magnetic field strength increases outwards with the field's orientation pointing away from the center. The Zeeman shift splits the magnetic substates of the excited state. The splitting increases with the magnetic field strength away from the center. The energy of the $m_F = -1$ substate decreases, and the light of the red-detuned laser is closer to resonance. The energy increases for the $m_F = +1$ substate, and the laser light is further detuned. A spatially dependent scattering force arises if one laser beam mainly drives transitions to $m_F = +1$ state and the other beam mainly drives the transition to $m_F = -1$. This results in an imbalance of scattered photons from the two beams and hence a force. Since the two transitions mentioned above are a σ^- and a σ^+ transition, the selective addressing can be achieved by a circular polarisation of the laser light. Here, both beams have the same handedness relative to their propagation direction[3]. The resulting force always points towards the trap's center because the magnetic field switches directions there. Thus the role of the two

[3]Unfortunately, there are different conventions for defining left-handed and right-handed polarization. We will avoid this terminology here

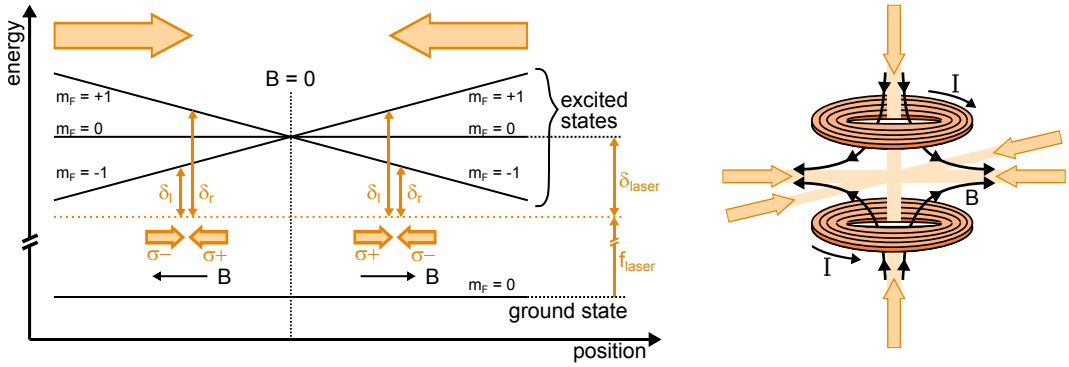

Figure 5.5: Working principle of a magneto-optical trap. A magneto-optical trap (MOT) achieves simultaneous cooling and trapping of atoms; the trapping is illustrated in the left-hand side of the figure for one spatial dimension. The model system for a MOT is a ground state with $m_F = 0$ and an excited state, which is split into three magnetic substates $m_F = [-1, 0, 1]$. A magnetic field gradient makes the substate energies spatially dependent. For trapping, the magnetic field – and thus the magnetic substates' energy shifts– requires a particular form, with a magnetic zero-point at a center and increasing field strength in both directions. Two circular-polarized laser beams (with the same handedness) are crossed with opposite propagation directions (large arrows). On the left of the magnetic field gradient, the laser beam from the left is σ^- polarized with respect to the magnetic field and drives the transition from the ground state to the $m_F = -1$ excited state. The laser from the right is σ^+ polarized and drives the transition to the $m_F = +1$ excited state (see small arrows). Due to the energy shifts of the levels in the magnetic field, the σ^- transition (left laser) is closer to resonance, and more photons are scattered from the left laser. The net scattering force accelerates the atoms towards the center of the trap. At the right side of $B = 0$, the transitions of the laser beams are reversed. An atom will again be accelerated towards the center and trapped there. The setup for three-dimensional MOT is shown on the right-hand side. Two magnetic coils in anti-Helmholtz configuration create a magnetic quadrupole field with a zero point at the center. Three pairs of counter-propagating laser beams create the cooling forces. For the horizontal beams, the handedness of the polarization must be opposite to the handedness of the vertical beams. This is caused by the orientation of the magnetic field relative to the propagation direction of the beams, which is opposite for the horizontal and vertical beams.

laser beams a reversed on the two sides of the zero-point. For spatial trapping in three dimensions, the spatial forces are achieved with a quadrupole magnetic field, as is illustrated in fig. 5.5. The magnetic field points away from the center in the horizontal directions for the depicted configuration. This is the situation described in the above one-dimensional configuration. The magnetic field points towards the center in the vertical direction, and the handedness of the light's polarisation needs to be reversed. This results in the same σ^+ and σ^- polarisation of the beams.

The great advantage of a magneto-optical trap is the large range of atom velocities that can be captured. This trapping range cannot only be explained by the Doppler shift. For potassium-39, the Doppler-shift at the D2 line is $1.2\,\mathrm{MHz/(m/s)}$. For a typical laser detuning of a few 10 MHz at maximum, only slow atoms can be cooled. Typical velocities for a room temperature atomic gas are around $300\,\mathrm{m/s}$. However, due to the magnetic forces and optical pumping of atoms between the magnetic substates, atoms can be considerably slowed while crossing the trapping region until they enter the velocity range of the Doppler cooling. Thus, a magneto-optical trap can capture and cool a significant amount of atoms already from a room-temperature atomic gas. The constant scattering of photons limits the final temperature of the atoms in the trap. A fundamental temperature limit is set by the natural linewidth Γ of the optical transition, which determines the scattering rate. This temperature is called the Doppler limit with the Doppler temperature $T = \hbar\Gamma/2k_B$. For potassium-39, temperatures of the atomic cloud in the MOT are typically on the order of several hundred micro Kelvin.

A special property of potassium-39 is the poorly resolved hyperfine manifold. This makes it impossible to address a single hyperfine level by an optical transition selectively, which has a direct consequence for the magneto-optical trap. For potassium-39, a MOT is realized on the D2 line with the $|F = 2\rangle \rightarrow F' = 3$ transition (see section 5.1). The polarization-setup of the MOT beams pumps atoms in the $|F = 2, m_F = 2\rangle$ /$|F = 2, m_F - 2\rangle$ state and drive the transition to the $|F' = 3, m_F = 3\rangle$ /$|F' = 3, m_F - 3\rangle$ state. The excited state can only decay back to this particular ground state, leading to a closed transition. However, the other excited states are excited off-resonantly, and can decay back into the $F = 1$ ground state. Atoms in this state are no longer cooled and lost from the MOT. They must be re-excited into the cooling cycle by adding a second laser with the appropriate frequency – a repumper laser. Atom-loss is a minor effect for some atomic species – like rubidium – and only small repumping intensities are needed. For potassium-39, a decay to the $F = 1$ ground state occurs with almost 50% probability. Consequently, cooling and repumping lights must be overlapped in all MOT beams with approximately equal intensity since both lights significantly contribute to the cooling forces.

5.9 Sub-Doppler cooling

For a laser-cooled atomic sample, temperatures can be lowered by increasing the cooling force relative to the scattering rate or by trapping very cold atoms in a dark state where they do not scatter photons anymore. Sisyphus cooling and polarization gradient cooling [67] in an optical molasses belongs to the first category, while grey molasses cooling (following section) falls into the second category.

Sisyphus cooling is realized in the light field of two counter-propagating, linearly polarized laser beams with their polarization orthogonal to each other (lin $\perp$ lin configuration). The resulting light field has a constant intensity, but its polarisation changes from linear to σ^+ polarized, to linear polarized, to σ^- polarized on the length of half a wavelength (see fig. 5.6). In the atomic level structure shown on the left-hand side of that figure, the different states are affected by the presence of the light field. The eigenenergy states of the atom-light system are a superposition of the unperturbed ground states. These eigenenergy states are called dressed states. The exact decomposition and the energy of the dressed states depend on the light field's polarisation. Thus, the polarisation gradient created by the 'lin $\perp$ lin' configuration leads to a position-dependent energy shift and thus to an effective potential landscape. The two ground states have an opposite modulation, as depicted in fig. 5.6.

To understand the cooling process, we start with an atom in one of the two dressed states. As it moves along the potential landscape, it slows whenever 'climbing a hill' as kinetic energy is converted into internal energy. The other way around, it accelerates when 'rolling down a hill.' Cooling occurs if the atom climbs hills much more often than it rolls down. For that purpose, the atom must be optically pumped between the two states at the right moment. This is the case for red-detuned laser light. The 'top of the hill' is then closer to resonance, and a photon is more likely to be absorbed in that position. Spontaneous emission may occur into the other ground state, which has a valley at that position. The energy difference between the two states is radiated away by the emitted photon. Following its remaining momentum, the atom climbs the next hill, which initiates the next scattering event. Inspired by Greek mythology, these cycles of hill-climbing and scattering to a valley are called *Sisyphus cycles* and the cooling process *Sisyphus cooling*. The cooling is most effective if the next scattering event occurs once the atom reaches the next hilltop, i.e., if the atom travels a distance of $\lambda/4$ on the time scale of a scattering event. For potassium-39, with the transition at 770 nm and a natural linewidth of $\Gamma = 2\pi \cdot 6\,\mathrm{MHz}$ this is the case for a speed of approximately 7 m/s. Thus, Sisyphus cooling is only effective for precooled atomic clouds. Increasing the laser detuning reduces the scattering rate, which moves the most effective cooling to smaller velocities. A steady increase of the detuning collects atoms and sweeps them to ever lower momenta. At the

same time, a lowered scattering rate also reduces the heating caused by spontaneous emission. In combination, temperatures far below the Doppler limit are possible. For potassium-39, the minimum temperature is limited by the poor resolution of the hyperfine manifold, which in turn limits the maximal detuning. Nonetheless, temperatures as low as 25 μK have been reached [68–70].

Sub-Doppler cooling is often realized not in the lin $\perp$ lin configuration but in a configuration with counter-propagating σ^+ and σ^- beams. While the setup seems similar to Sisyphus cooling, the underlying physical process is entirely different. The light field of the σ^+–σ^- configuration is always linearly polarized, with the polarization rotating in space. This polarization pattern can be described by a rotating quantization axis. For a moving atom, this amounts to an effective rotating frame that constantly redistributes populations and builds up an imbalance in the ground state populations. Since the scattering rates of the ground states are different for σ^+ and σ^- light, photon scattering is more effective from one of the counter-propagating laser beams. A quantitative treatment (see for example[67]) shows that this indeed results in a velocity-dependent force and temperatures comparable to Sisyphus cooling. The σ^+–σ^- configuration has the advantage that the polarisation of the laser beams is the same as in a magneto-optical trap. A direct transition from an MOT to sub-Doppler cooling is possible simply by switching off the magnetic fields.

5.10 Grey molasses cooling

Grey molasses cooling combines Sisyphus-like cooling cycles with a coherent dark state. Experimentally, this scheme requires much more effort than Sisyphus cooling since it cannot simply reuse the laser setup from a magneto-optical trap. However, for potassium-39, grey molasses cooling reaches lower temperatures than Sisyphus cooling.

The model system for this type of cooling is a Λ-system shown in fig. 5.6 with two ground states $|g_1\rangle$ and $|g_2\rangle$ connected to an excited state $|e\rangle$ via a σ^+ and σ^- transition. The system is irradiated with light of two frequencies in a Raman condition, i.e., the two frequencies have the same detuning δ to their respective transitions. In the Raman condition, there is destructive interference between the two transitions, as is the case in electromagnetically induced transparency (EIT) [71]. The interference is reflected in the dressed state picture, where a superposition of the original states describes the eigenenergy states of the combined atom-light system. For an atom at rest, the ground state manifold is divided into a bright state $|b\rangle$ and a dark state $|d\rangle$. An atom in the bright state still scatters photons and experiences light pressure forces and heating due to spontaneous emission. However, an atom

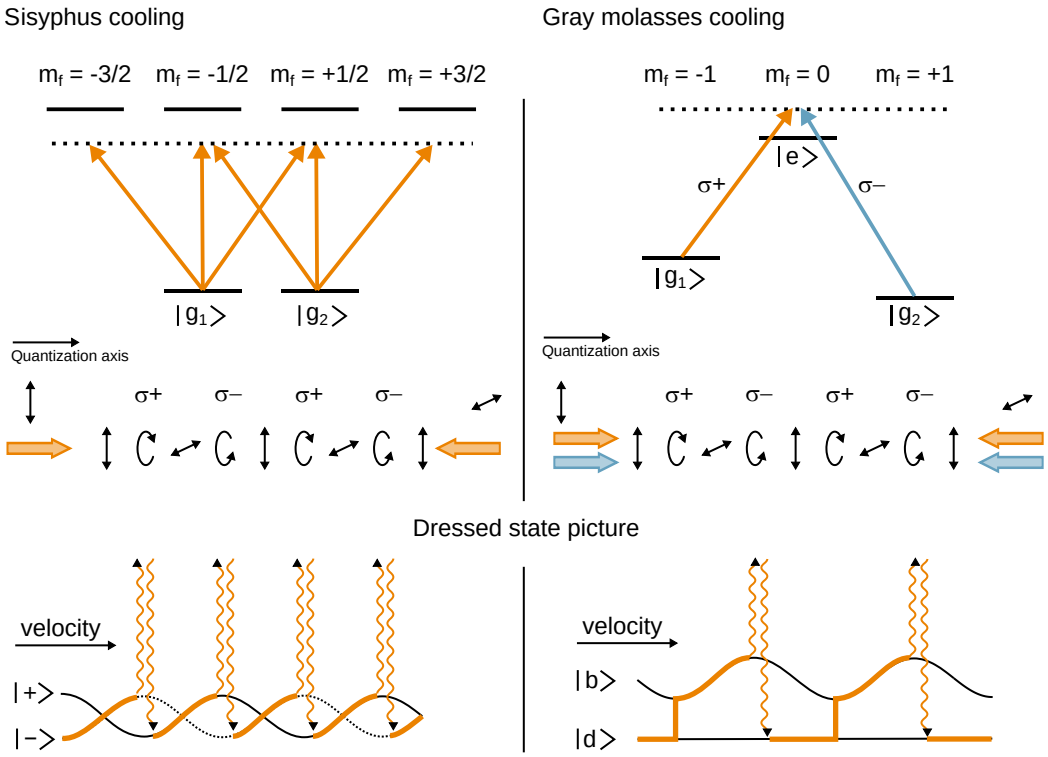

Figure 5.6: Sisyphus and grey molasses cooling. The minimal atom model for Sisyphus cooling (left-hand side) has two ground and four excited states. It is irradiated by two counter-propagating, red-detuned laser beams in the 'lin⊥lin' configuration. The resulting polarization gradient shifts from linear polarization to σ^+, to linear, to σ^-, and so on. Depending on the polarisation, different transitions between the ground and excited states are possible. In the dressed state picture, this results in a spatial modulation of the eigenenergy states $|+\rangle$ and $|-\rangle$ of the combined atom-light system. The energy modulation is an effective potential landscape. As the atom moves, it undergoes Sysiphus-cycles depicted in the lower-left part. In each cycle, the atom moves up a potential hill and slows down as kinetic energy is converted into internal energy. The increased internal energy is radiated away in a scattering event to the second ground state. Similar scattering cycles are realized in gray molasses cooling (right-hand side). Here the atom model requires two ground states and an excited state in a Λ-configuration. It is again radiated with counter-propagating beams in the 'lin⊥lin' configuration and experiences the resulting polarization gradient. In this case, however, both beams contain two frequencies in a Raman condition and are blue-detuned to their respective transition. The Raman condition creates a dark state $|d\rangle$ and a bright state $|b\rangle$ with the energy of the bright state modulated in the polarization gradient. By motional coupling, atoms cross from the dark to the bright state. They then convert kinetic to internal energy while climbing the potential hill. A scattering event brings the atom back into the dark states and radiates the difference in internal energy.

in the dark state no longer interacts with the light. In particular, it will no longer be heated by photon scattering. If the atom is at rest in the dark state, it will remain there indefinitely. For a moving atom, there is a non-zero probability of changing from the dark state into the bright state (*motional coupling*). The faster the atom, the higher is the probability of a transition into the bright state. Once the atom is in the bright state, it scatters photons, and its velocity changes with each scattering event. Every spontaneous decay might bring it back into the dark state. If the atom is slow after that last scattering, it will remain trapped in a dark state. If it is fast, it will once again couple to the bright state and repeat the cycle. Over time, a population of slow atoms accumulates in the dark state. This phenomenon is known as *velocity-selective coherent population trapping (VSCPT)*. The temperature of the collected atom sample can be even below the recoil limit since the last random photon emission might leave the atom below the recoil velocity [72].

Grey molasses cooling combines the trapping in a dark state with an active cooling force [73]. For that purpose, laser beams are arranged in a 'lin $\perp$ lin' configuration, creating a polarization gradient as described in the previous section. In this case, however, the laser beams contain the frequencies of both transitions in the Raman condition. The energy level of the dark state is unaffected by the polarization gradient, but the bright state is modulated as shown in fig. 5.6. In the potential of the bright-state, Sisyphus-like cooling cycles take place. An atom initially in the dark state couples to the bright state due to its motion. The transition is most probable at a potential minimum of the bright state, where dark and bright states are closest together. Once in the bright state, the atom slows as it moves in the potential landscape to higher potential energies. A scattering event may bring it back into the dark state. It is most probable at the potential maximum of the bright state, where the overlap with the excited state is largest. The scattering event radiates the energy converted from kinetic to potential energy. For an average over many cycles, atoms are actively cooled into the dark state, where they remain unaffected by heating processes caused by photon scattering. Note that the level structure shown in fig. 5.6 is only achieved for blue-detuned light. For a red detuning, the energy of the dark state will be above the energy of the bright state. In this case, motional coupling is most likely at a potential maximum of the bright state, and atoms are heated instead of cooled.

In potassium-39, grey molasses cooling can be realized on the D1 transition. The D1 cooler and D1 repumper (see section 5.1 for the naming convention) are the two laser lights necessary for the cooling scheme. Both lights need to be blue detuned to the entire excited state manifold. The level structure of potassium-39 is much more complicated than the Λ model system described above. For a complete treatment,

all levels need to be considered when calculating the eigenstates of the dressed state picture. For lithium-6, which has a similar level structure as potassium-39, a complete calculation can be found in [74]. For this complex level structure, there are no dark states but *grey states* instead. The name of the cooling scheme is derived from these states. Grey states couple only weakly to the excited state and are thus only very lightly modulated by the polarization gradient. Between the grey states and the strongly modulated bright states, Sysiphus-like cooling cycles take place. Atoms cooled into a grey state still scatter photons but with a low enough probability that very low temperatures become possible. In three dimensions, the necessary polarization gradient can also be created with three pairs of counter-propagating laser beams in the σ^+–σ^- configuration. In such a setup, temperatures down to $6\,\mu$K have been reached for potassium-39 [75, 76].

5.11 Evaporative cooling

All optical cooling schemes are ultimately limited by heating due to (residual) photon scattering. Reachable temperatures are typically on the order of a few micro Kelvin, which is still far above the temperature needed for Bose-Einstein condensation, normally around $50 - 100\,$nK. The only currently known way to reach these low temperatures is evaporative cooling. This method takes advantage of the fact that, in a thermal cloud, most of the ensemble's energy is carried by few fast atoms. By discarding these fast atoms, energy can be effectively removed. Initially, the remaining atoms are not in thermal distribution since the high-energy tail is missing. Scattering processes between the atoms redistribute energies until the distribution is once again thermal. In particular, the high-energy tail needs to form, and, once again, few atoms receive a lot of energy. This energy must be provided by the bulk of the ensemble. Thus, most of the atoms lose energy during thermalization, and the temperature of the ensemble decreases. By repeating this process – removing the high-energy tail and letting the remaining atoms thermalize – ever lower temperature can be reached. This process is only limited by the number of atoms that can be discarded.

Evaporative cooling can only take place if the atoms can rethermalize effectively. For this to happen, atoms need to have a high collision rate and thus a high s-wave scattering length. For some atom species, like rubidium, this is naturally the case at zero magnetic field; for others, including potassium-39, it is not. In these species, evaporative cooling can only be performed in combination with interaction-tuning at a Feshbach resonance (see section 5.4). This implies that evaporative cooling is not possible in a magnetic trap. Instead, trapping must be realized in a dipole trap

combined with a strong homogeneous magnetic field for Feshbach-tuning. In a dipole trap, cooling is initiated by a slow and continuous lowering of the trap's intensity and thus the trap depth. The most energetic atoms escape from the trap, and the remaining atoms become colder. Lowering of the trap continues until the temperature gap between optical cooling (around $10\,\mu$K) and Bose-Einstein condensation (around $50 - 100\,$nK) is bridges and a condensate forms. More than 99.9% of the atoms are lost during that process.

5.12 Fluorescence and absorption imaging

A direct observable in ultra-cold atom experiments is the density distribution of the atoms. It can be measured both by absorption and fluorescence imaging. For this work, absorption imaging is used for the main experiments. Fluorescence imaging only is employed for monitoring a magneto-optical trap.

For both types of imaging, atoms are irradiated with a resonant laser. Absorption and spontaneous emission lead to the scattering of photons from the imaging beam into random directions. Fluorescence imaging detects the scattered photons. For that purpose, a camera is placed such that it does not see the imaging beam itself. With the help of lenses, the atom plane is imaged on the camera's CCD chip. The intensity of detected light reflects the atomic density. For absorption imaging, the camera is placed such that the imaging beam falls onto its chip. Again the atomic plane is imaged onto the camera's CCD chip. Using a saturated absorber model, the density distribution of the atoms can be inferred from the absence of light compared to a reference image of the unperturbed laser beam [77]. Both fluorescence and absorption imaging are destructive measurements since the scattering of photons heats and thus destroys the condensate. Therefore, the entire cooling cycle and the experiment must be repeated for every image.

For optimal imaging, the atoms need to scatter as many photons as possible in a short time. Hence, the imaging laser should thus be resonant to the atomic transition. In addition, atoms need to remain in states addressed by the laser. If there is a decay channel to a different state, atoms need to be re-excited into the imaging cycle by adding a corresponding second laser frequency. For potassium-39 at zero magnetic field, imaging light should contain an equal amount of D2 cooling and D2 repumping light. Imaging becomes more involved at higher magnetic fields. This includes imaging at the magnetic field strength of the Feshbach resonance at 562G where the experiments described later in this work take place.

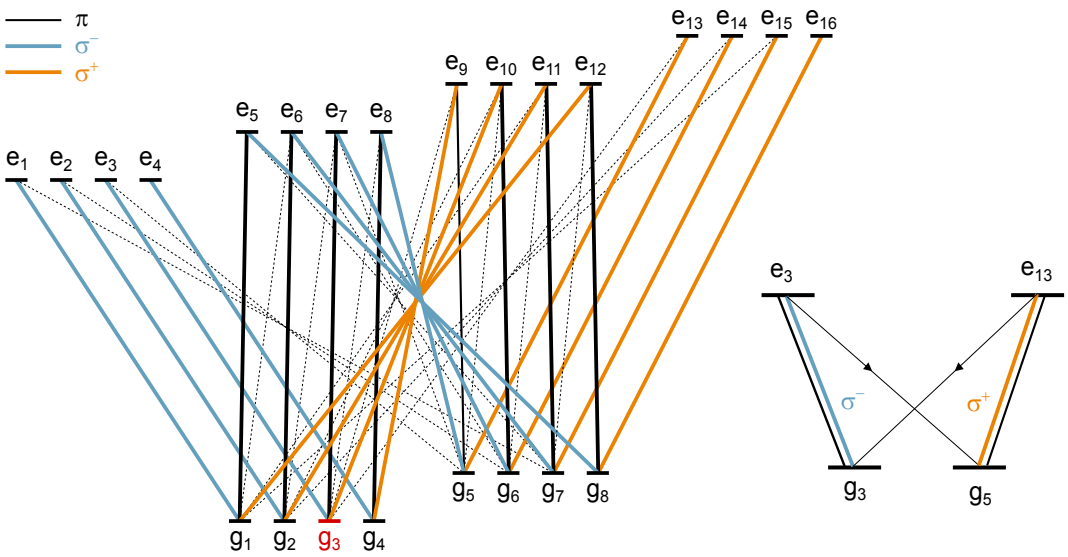

Figure 5.7: Imaging scheme at high magnetic fields. At magnetic fields close to the Feshbach resonance, around 550 – 560 G, only view transitions are still allowed between the eight ground state and the 16 excited states of potassium-39 (see section 5.2 for a definition of the states). The solid lines indicate allowed transitions, and different colors encode the polarization of the respective transition. The dashed lines show additional (weak) decay channels. In the experiment, atoms are initially in the g_3 ground state (red) which corresponds to $F = 1, m_F = -1$ state at zero magnetic field. For imaging, the transition $g_3 \rightarrow e_3$ is used. From this excited state, atoms decay back to g_3, but a residual decay is possible to g_5. An additional laser light excites atoms from g_5 to e_{13}. Here, decay occurs back to g_5; and the original ground state g_3. This leads to a closed imaging scheme in a reduced form on the right-hand side. This figure is adapted from [60].

5.13 Imaging of potassium-39 at moderate to high magnetic fields

The experiments described later in this work take place at magnetic fields around the Feshbach resonance at 562 G, and imaging of the atomic density needs to be performed at these fields. For that, the level structure of potassium-39 at high magnetic fields needs to be taken into account. At these fields, all eight ground states of potassium-39 have distinct energies. They are named $|g_1\rangle$ to $|g_8\rangle$. The same is true for the 16 excited states $|e_1\rangle$ to $|e_{16}\rangle$ (see section 5.2 or fig. 5.2 for the levels). At the magnetic field strength of the Feshbach resonance, the eigenenergy states of the atoms are best described in the $|m_J, m_I\rangle$ basis. Here $I = 3/2$ is the nuclear spin, J the total electron spin and m_I and m_J the respective magnetic quantum numbers. In

this basis, the excited states only have a single $|m_J, m_I\rangle$-component. However, most ground states are in a superposition of two basis states. They consist to 98% percent of a main $|m_J, m_I\rangle$ state but have a 2% admixture of a second state. This influences the allowed optical transitions shown in fig. 5.7. In the $|m_J, m_I\rangle$ basis, optical transitions are allowed that change m_J by $+1$, 0 or -1 for σ^+, π or σ^- polarized light. The solid lines show the transitions allowed for each state's dominant component. The dashed lines mark the additional transitions caused by the 2% admixture of a second $|m_J, m_I\rangle$ to the ground states. If the atoms are imaged with only one frequency, these additional decay channels result in atom loss to a dark state. A closed imaging cycle can be reached using a two-frequency scheme [60, 78, 79].

For this work, atoms are caught in the $|\, F = 1, m_F = -1 \,\rangle$ state at low magnetic field, corresponding to the $|g_3\rangle$ ground state. At high magnetic fields they are imaged with the $|g_3\rangle \rightarrow |e_3\rangle$ transition [58]. While most atoms decay back into the $|g_3\rangle$ ground state, a significant fraction instead decays into the $|g_5\rangle$ state, which is a dark state. If the transition is saturated, half the atoms will be lost to this dark state on a time scale of $2.2\,\mu$s [79] which limits the absorption signal. To increase the signal, a second laser light is added, which drives the $|g_5\rangle \rightarrow |e_{13}\rangle$ transition to a second excited state. From this excited state, atoms can only decay back into the same two ground states $|g_3\rangle$ and $|g_5\rangle$. This leads to the closed imaging cycle depicted on the right-hand side of fig. 5.7. With this imaging scheme, only 2% of the atoms are lost to dark states for a typical imaging pulse of $10\,\mu$s. The residual losses are caused by the remaining admixture of the excited states in the $|m_J, m_I\rangle$ (on the order of 10^{-4}). In our experimental setup, an optimal signal to noise at a high magnetic field is reached for equal intensities of both imaging lights. More details on this four-level scheme together with an atom-number calibration for the imaging can be found in [79] and [61].

Chapter 6

Experimental system and setup

This chapter describes our experimental setup that creates and controls a quasi-two-dimensional Bose-Einstein condensate (BEC) of potassium-39. To construct the setup and implement the different traps and cooling schemes, we could build upon results and experiences from previous BEC experiments [70, 76, 80–82].

After a brief overview of the cooling and trapping scheme of our setup in section 6.1, section 6.2 describes the experiment control, section 6.3 the vacuum system, and section 6.4 the setup of magnetic field coils and their calibration. The different imaging setups that monitor the different cooling stages and record experimental results are explained in section 6.5. The following sections describe the setups for the different cooling stages. These include the magneto-optical traps section 6.6, the grey molasses section 6.7, a magnetic trap section 6.8 and dipole traps section 6.9. The latter includes the dipole traps used for evaporation and the final trap that shapes the quasi-two-dimensional BEC. Finally, section 6.10 shows the laser systems needed for the different stages of the experiment.

6.1 In a nutshell

A Bose-Einstein condensate forms once the phase-space density of the atomic cloud surpasses a critical value.[1] Thus, for the experimental realization of a BEC, an atomic cloud must be first caught and then simultaneously compressed and cooled until the critical phase-space density is reached.

[1] The critical phase-space density is given by $n\lambda_{dB}^3 \geq \zeta(2/3) \approx 2.6$ [52], with n the density, λ_{dB} the thermal deBroglie wavelength and ζ the Riemann zeta function.

In our setup, the trapping and cooling of the atoms starts with a two-dimensional magneto-optical trap (MOT) loaded from a background vapor of potassium. The $2d$-MOT creates an atom beam that loads a $3d$-MOT in a region of lower vapor pressure. A short compressed MOT terminates this first stage and increases the density of the atom cloud. Afterward, the magnetic fields switch off to allow for a stage of grey molasses cooling using the D1 transition. A subsequent magnetic trap catches a single magnetic substate and further compresses the cloud adiabatically. Due to the small negative scattering length of potassium-39 at a low magnetic field, evaporative cooling within the magnetic trap is not possible. Instead, the atoms are directly loaded into a dipole trap. In this optical trap, the scattering length is adjusted by applying a homogeneous magnetic field with its field strength close to a Feshbach resonance of potassium-39. Lowering of the trap's depth initializes evaporative cooling, which proceeds until the atoms reach degeneracy.

After condensation, the cloud is levitated by a magnetic field gradient counteracting the gravitational force, compressed in gravity direction, and loaded into a single sheet of a pancake trap. Radial trapping is achieved by a Gaussian beam perpendicular to the pancake trap. At this point, the atoms form a quasi-two-dimensional, radially symmetric condensate whose radial size and scattering length can be controlled via the laser power in the radial trap and the magnetic field strength around the Feshbach resonance, respectively. This is the starting point for the experimental runs.

At the end of each run, an absorption image is taken at the high magnetic field using a four-level scheme with two distinct laser frequencies.

6.2 Experiment control

In order to cool a cloud of atoms to degeneracy and perform a measurement, many subsequent steps are necessary at exact timings down to sub-millisecond precision. Their control requires a digital-to-analog interface that translates a programmed experimental sequence into voltage signals that regulate the different components of the experiment. For our machine, the interface consists of five National Instrument cards[2] with a total of 32 analog and 80 digital output channels. The digital channels switch between voltages of 0 V and 5 V signifying logical 0 and 1 in a transistor-transistor logic (TTL). These channels are used to switch components between two states. The analog channels support voltages between -10 V and $+10$ V with a resolution of 0.3 mV. They are used to regulate continuous variables like the

[2] four PXI-6733 and one PXI-6254

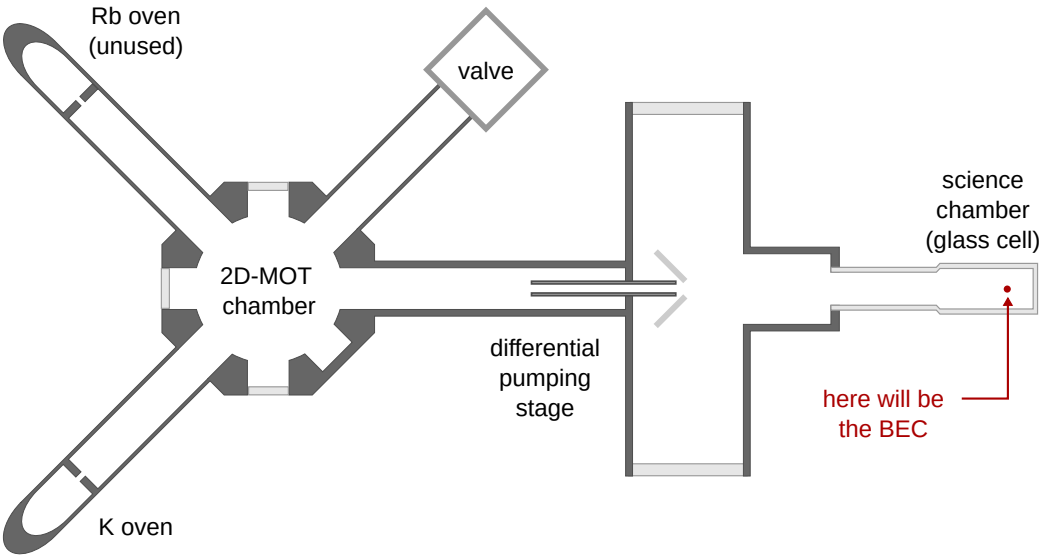

Figure 6.1: Top view of the vacuum system. On the left-hand side, a potassium oven fills the 2*d*-MOT chamber with a thin gas of potassium. A differential pumping stage separates this region of relatively high pressure (10^{-8} mbar) from the science chamber with a pressure of 10^{-11} mbar on the right. Here the condensate is created and experiments performed.

power of a laser beam or the frequency applied to an acousto-optic modulator. In our setup, each channel can be programmed with a time resolution of 50 μs. Their synchronization and programming is described in [83].

6.3 Vacuum system

The vacuum system is divided into two parts connected by a long and narrow tube (see Fig 6.1). The tube serves as a differential pumping stage; different pressures can be maintained on each side. On the low-pressure side, an ion pump maintains a pressure around 10^{-11} mbar. On this side, a glass cell – the *science chamber* – is attached in which an atom cloud is initially caught in a magneto-optical trap (MOT) and cooled till degeneracy in each experimental run. To reduce the heating of the atom cloud during experiments, the pressure on this side needs to be as low as possible. The downside of the low pressure is that not enough atoms are available for a sufficient loading of the initial magneto-optical trap. Instead, the MOT must be loaded from the vacuum chamber's 'high' pressure side. This chamber is also constantly pumped but additionally connected to a potassium oven. A second oven

containing Rubidium is connected but not active. The potassium oven is heated to a temperature of $\sim 70°C$ and fills the chamber with a potassium vapor at a pressure of 10^{-8} mbar. At this pressure, enough potassium atoms are distributed around the vacuum chamber to load a 2d-MOT from the background gas efficiently. The $2d$-MOT creates a directed atom beam that passes through the differential pumping stage and loads the $3d$-MOT. With this setup, fast loading of the 3d-MOT can be combined with low pressure in the glass cell. A more detailed description of the vacuum system and its components can be found in [84, 85].

6.4 Magnetic fields and coil setup

Different magnetic field configurations or even the absence of magnetic fields are essential for several steps in cooling the atoms and Feshbach-tuning during measurements.

On the high-pressure side of the vacuum, only a single configuration is needed for the $2d$-MOT. This is a quadrupole field with a gradient of $\approx 14\text{G/cm}$. It is realized by a set of two elongated coils (see fig. 6.2). These coils have a large enough distance from the final condensate that their current can be permanently turned on; any residual influence on the atoms is easily compensated.

Different field configurations are needed on the low-pressure side, and fast switching between them is necessary during the experimental sequence. These configurations are

- A three-dimensional quadrupole field with a gradient of $\sim 8 - 15\text{G/cm}$ for the MOT and with a gradient of $\sim 60\,\text{G/cm}$ for the magnetic trap
- Vanishing magnetic field for the grey molasses cooling
- Homogeneous magnetic field around 560 G for the tuning of the s-wave scattering length near the Feshbach-resonance for both evaporative cooling and the experimental measurements
- Magnetic field gradient in gravity direction (z direction), canceling the gravitational force in the homogeneous field configuration
- Vanishing magnetic field gradients along the horizontal direction in the homogeneous field configuration

These requirements are met by the coil setup shown in fig. 6.2. Both the quadrupole field and the homogeneous field are created by the pair of large coils at the center,

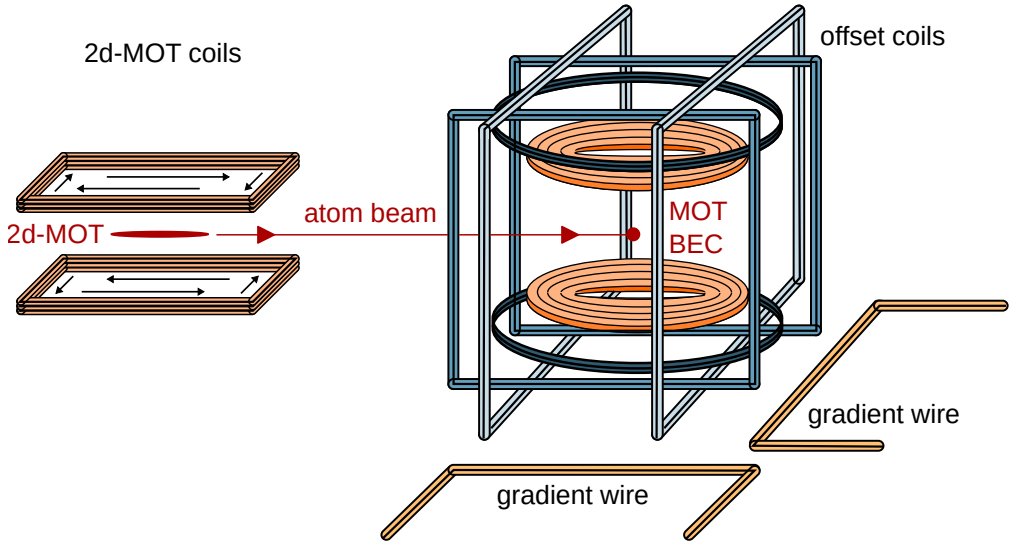

Figure 6.2: Coil setup for all magnetic field configurations. The elongated quadrupole field for the 2d-MOT is created by a dedicated set of coils with opposite current flow through the coils (left-hand side). The right-hand side shows the coil setup around the region of the MOT, magnetic trap, and finally, the condensate. The large coils at the center (orange coils) are used in two different configurations. If the current flows in opposite directions in the two coils, they create the quadrupole field for MOT and magnetic trap. For current flowing in the same direction, they create a homogeneous field. Switching between the two configurations is achieved by reversing the current in the upper coil. A gradient in gravity direction can be created with a larger current through the upper coil in the homogeneous field configuration. The coils depicted in blue are three Helmholtz pairs that create homogeneous offset fields in all three spatial directions. Together with the two gradient wires, they are used for the compensation of residual fields and field gradients.

which is described in detail in [86]. The distance between the coils is a compromise between an Anti-Helmholtz and a Helmholtz configuration. The upper coil of this pair is connected to an H-bridge circuit (see fig. 6.3), which can reverse the direction of the current flow (see again [86] for details). As illustrated in the figure, this permits switching between a quadrupole field (right-hand side) and a homogeneous field (left-hand side). The strength of the current is regulated by two passbanks (for the passbank design, see also [86]). Opening of passpank ‘one’ in fig. 6.3 allows equal current flow through both upper and lower coil. It thus creates either a quadrupole or a homogeneous field. The second pass bank is only used in the homogeneous field configuration. It allows additional current flow through the upper coil but bypasses the lower one. This creates a magnetic field gradient in addition to the homogeneous field. Since the upper coil carries more current, the field is stronger there. For atoms

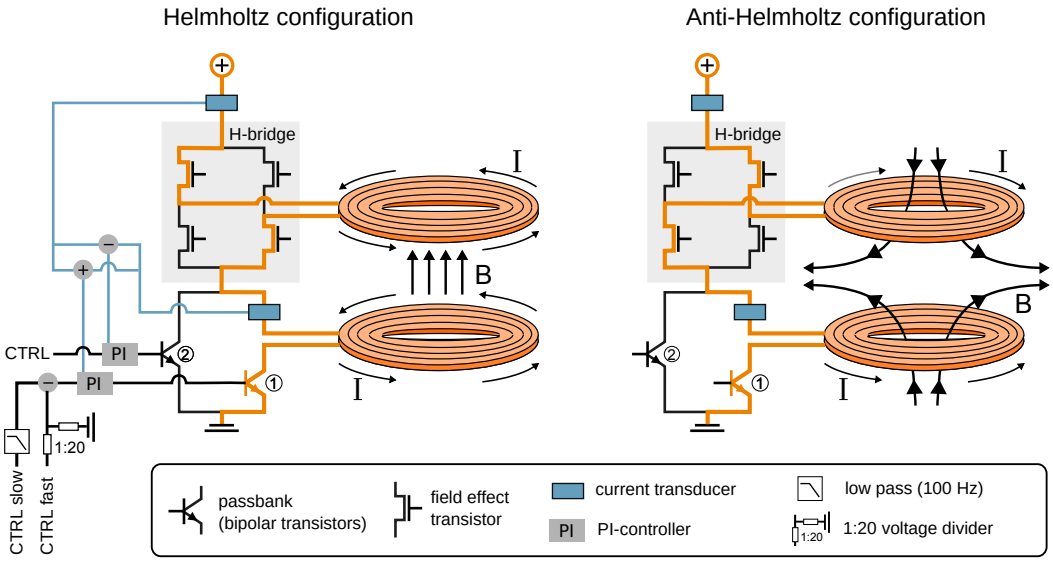

Figure 6.3: Control circuit for the large coils. The large coils can create either a homogeneous field for Feshbach-tuning or a gradient field for MOT and magnetic trap. Switching between the two configurations is achieved with an H-bridge. Two passbanks regulate the current through the coils. Passbank one creates a current that flows simultaneously through both coils; passbank two adds a current only to the upper coil but bypasses the lower. A larger current in the upper coil creates a magnetic field gradient that can levitate atoms against gravity.

in a high-field-seeking state, this results in a magnetic force counteracting gravity. By careful adjustments, an exact cancellation of the gravitational and magnetic force is possible, and the atoms are levitated.

Both passbanks are regulated via proportional-integral control loops (PI loops). Two low-noise current transducers[3] measure the current through the upper coil and lower coil, respectively. The difference between the two sensors is a measure for the gradient and is the input signal for controlling the gradient passbank. The sum of the currents is proportional to the strength of the homogeneous field and is the input for the main passbank. The set value for the latter control circuit is split into a fast and a slow channel to reduce noise from the experimental control. High-frequency noise is removed from the slow channel by a low-pass filter. The fast channel is attenuated by a factor of 20, reducing the noise by the same factor. This channel permits fast (but comparably small) changes of the magnetic field, which are required for the Feshbach tuning during measurements.

[3]Current Transducer: LEM, IT 400-S ULTRASTAB

The remaining coils shown in fig. 6.2 are three Helmholtz pairs (see [87] for details) called *offset coils*. Their primary purpose is to cancel residual magnetic fields during the stage of grey molasses cooling. Additionally, they shift the zero point of the quadrupole field during the magnetic trap to correct for long-term drifts in the position of the molasses and the dipole traps. The current in these coils can be adjusted via the experimental control but is not actively stabilized.

Two gradient wires complete the magnetic field setup. They create a magnetic field gradient in the two horizontal directions. At a high magnetic field, they cancel parasitic gradients from the supply wires of the large coils and other non-identified residual gradients. Just as for the offset coils, the current for the gradient wires can be adjusted but is not externally stabilized.

With the gradients compensated, the leading order deviation from a homogeneous magnetic field is a quadratic contribution from the large coils, called the curvature of the coils. At the typical field strength for Feshbach-tuning, slightly below 560 G, it creates a rotational symmetric attractive harmonic trap in the horizontal plane with a trap frequency of $\omega = 2\pi \cdot 5.5\text{Hz}$. This trap is not very relevant for this particular work since optical traps always provide stronger confinement. In the context of other experiments, this trap is used to measure the momentum distributions of a condensate similar to [88].

6.4.1 Calibration of the homogeneous field

To adjust the scattering length via Feshbach-tuning, precise control of the magnetic field strength at the position of the atoms is necessary. For this purpose, coil-currents must be calibrated against measurements of the homogeneous magnetic field. The most precise magnetic field sensor are the atoms in the condensate themselves. Their eigenenergy states depend on the magnetic field (see section 5.2), and a spectroscopy of the transition frequency between two states is a precise measurement of the magnetic field strength. The transitions between the ground state and excited state manifold of potassium-39 are optical (see section 5.2). Due to their natural linewidth of $\Gamma = 6\,\text{MHz}$, they are not optimal transition for an exact measurement. Instead, we use a transition within the ground-state manifold. These are microwave-frequency (MF) transitions with a negligible natural linewidth. In the Bose-Einstein condensate, atoms are in the g_3 ground state, which is also the state detected by absorption imaging. For MF-spectroscopy, the transition from that state to the g_6 ground state is used, which flips the electron spin but leaves the nuclear spin unchanged (see section 5.2). The transition is driven by an additional small coil placed directly at the glass cell. The current through the coil is

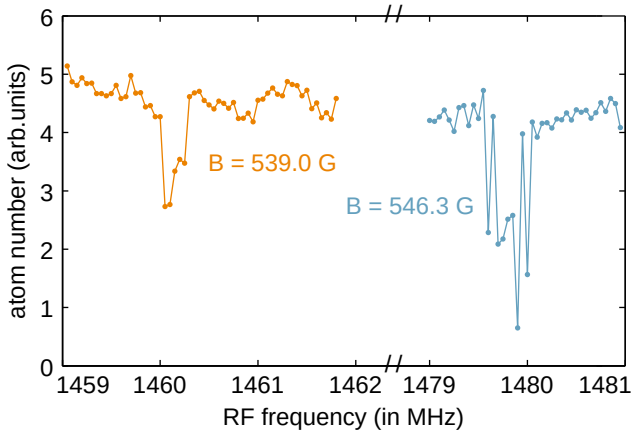

Figure 6.4: Microwave spectroscopy for magnetic field calibration. A transition in the ground-state manifold of the atoms is driven with an oscillating magnetic field. At the resonance, atoms are removed from the imaged state. The frequency at which the frequency occurs is a measurement of the magnetic field.

modulated with the microwave frequencies around the resonance. On resonance, atoms will be removed from the g_3 ground state, which results in a clear loss signal in the atom number. By repeating such a measurement at different magnetic field strengths, precise calibration of the magnetic field and the corresponding coil current is possible.

Two typical measurements at field values close to the Feshbach resonance are shown in fig. 6.4. The width of the measured resonances is below 0.5 MHz. At these high fields, the resonance frequency of the transition changes with 2.67 MHz/G. A conservative estimate for the error of the magnetic field calibration is thus $\Delta B \sim 0.2$ G. With this precision of the calibration, the main uncertainty for Feshbach-tuning is the position of the resonance with an error of 1.5 G [89].

6.5 Imaging setups

The experimental setup includes several imaging paths to monitor the atomic cloud during the experimental sequence and to detect the atomic density distribution at the end of each measurement run. This includes two cameras and a photodiode that detects the fluorescence signal of the magneto-optical trap shown in fig. 6.5. The cameras are not exactly in the horizontal plane; one is above it and one below. Combined, this gives a three-dimensional impression of the shape of the atomic cloud. Together with the fast signal from a photodiode, the alignment of the MOT

beams and the power balancing between beams can be optimized.

Figure 6.5 additionally shows two imaging paths in the horizontal plane, which take absorption images from the side. These are used to optimize the cooling stages and the loading of the traps. They also allow time-of-flight measurements at different stages to detect the temperature of the atomic cloud. The light frequencies can be switched between resonant light at zero and at high magnetic field in all three absorption beams. Section 6.10.2 describes how this is achieved.

The first imaging path is a comparably simple setup. A single lens images the atom plane onto a Guppy camera[4] with a magnification of approximately 0.9 (de-magnification). This setup is used to monitor and optimize the earlier stages of the experimental sequence, namely the compressed MOT, grey molasses, the magnetic trap, and the beginning of evaporative cooling. The second absorption imaging from the side reaches a magnification of ~ 29. It uses a combination of a home-build objective with an effective focal length of $f \sim 35\,\mathrm{mm}$ in combination with a secondary lens with $f = 1000\,\mathrm{mm}$. At its correct position for imaging, the objective blocks the beams of the magneto-optical trap. It is thus mounted on an automatic stage and is moved away from the glass cell for the early stages of the experimental sequence (or if not in use).

The main absorption imaging is used for the experimental measurements. It resolves the density distribution of the quasi-two-dimensional condensate. The condensate extends in the horizontal plane and is restricted along the gravity direction. Thus, the imaging beam is oriented along the gravity direction as shown in fig. 6.6. The figure also shows the vertical beams of the magneto-optical trap (in orange), which must share the same axis. They are described in detail in section 6.6. For imaging, the optical components marked in orange (a lens and a mirror) are removed from the path. The atoms are illuminated by the imaging beam from the top (blue beam). The atoms (red dot) scatter photons and thus remove light from the beam. As shown in fig. 6.12, the absorption signal is collected and collimated by an objective[5] with an effective focal length of $f = 35.0\,\mathrm{mm}$ and a numerical aperture $NA = 0.5$. A secondary lens with a focal length of $f = 1000$ focuses the signal onto the CCD chip of the main camera[6]. Note that the beam path after the atoms (light blue) depicts the absorption signal, i.e., the signal of a point source in the imaging plane (it does not show the imaging beam itself). The secondary lens is mounted on a piezo stage[7]

[4]Guppy camera, Allied Vision

[5]Custom made objective from 'Special Optics,' see thesis by Maurus Hans [61] for details of the objective, its mounting and adjustment.

[6]ProEM-HS 1024 Bx3, Princeton Instruments

[7]Translation Stage with Resonant Piezoelectric Motors, Thorlabs - ELL20/M

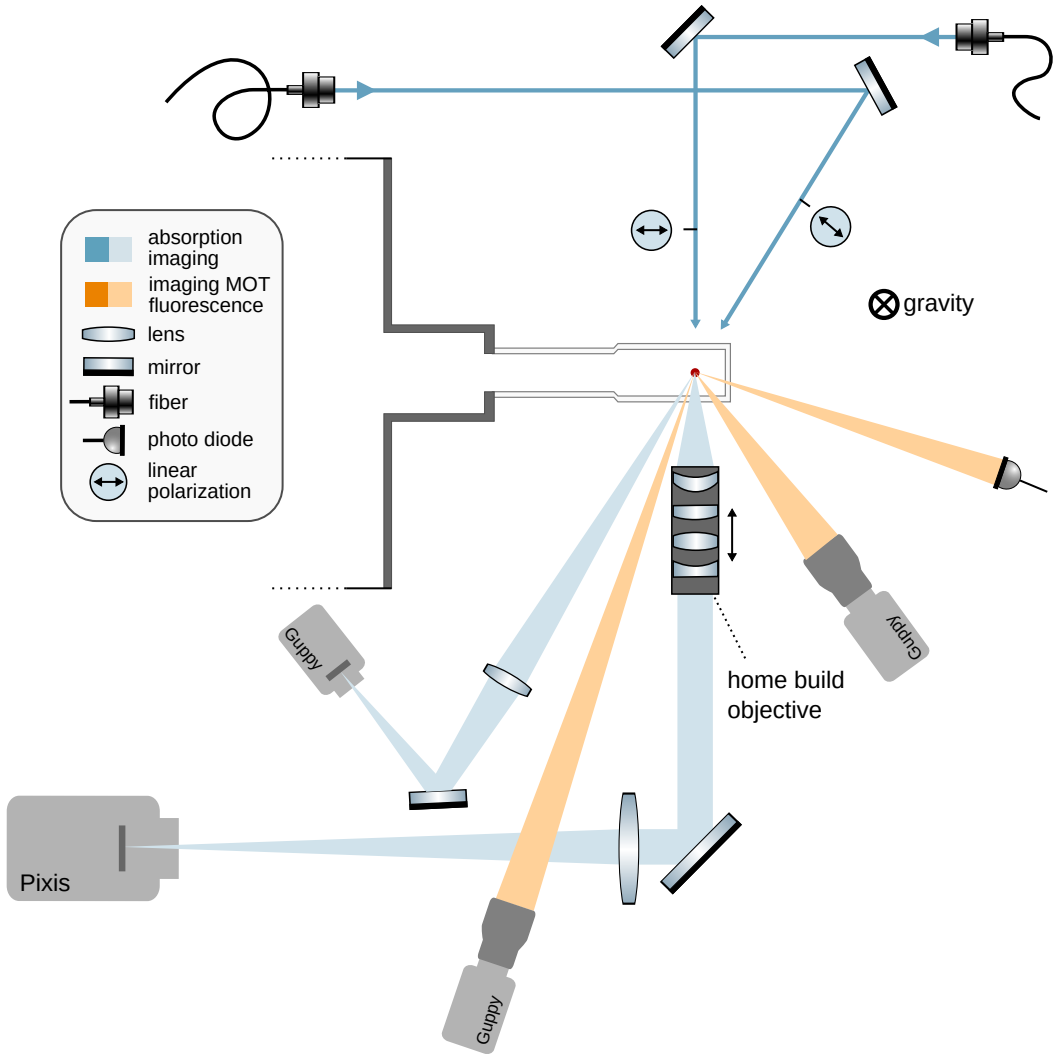

Figure 6.5: Imaging and monitoring setups – top view. During the different stages of cooling and trapping, the atoms are monitored by several fluorescence and absorption imaging setups. Two cameras and a photo-diode detect the MOT fluorescence. The cameras are not exactly in the horizontal plane allowing for a three-dimensional impression of the atomic cloud during the MOT stage. Two absorption imaging systems with a magnification of 0.9 (Guppy camera) and 29.0 (Pixis camera) can show the atomic cloud at the different stages of the experimental sequences. They are used to optimize the cooling and loading of the various traps.

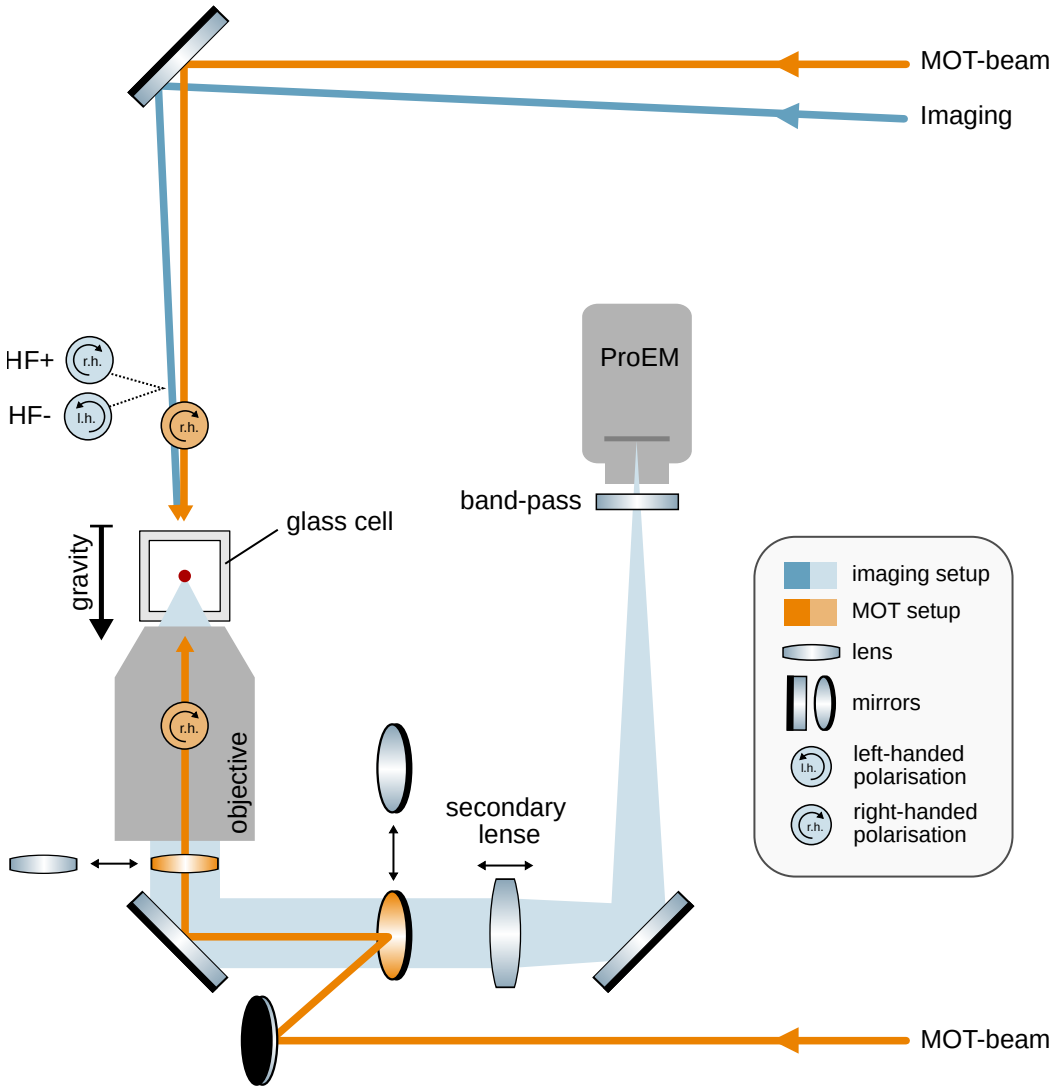

Figure 6.6: Main imaging setup and vertical MOT beams. The main absorption imaging is oriented along the gravity direction to resolve the density distribution of the quasi-two-dimensional condensate extended in the horizontal plane. The imaging beam contains two lights, the high-field σ^+ and high-field σ^- lights described in section 5.13. The vertical beams of the magneto-optical trap follow the same axis, and the lower beam needs to pass through the objective. A mirror and a lens are moved in and out of the imaging path to combine both imaging and MOT setup. They are marked orange for their position during the MOT stage and blue for their position during imaging.

with which the focal plane of the imaging system can be adjusted to the plane of the atoms. The chip of the CCD camera is protected against scattered light by a band path filter and a mechanical shutter [8]. The magnification of the main imaging was measured independently with the dynamics of the atoms after a Bragg pulse. For the Bragg pulse, the condensate is illuminated with a retro-reflected dipole beam. This creates a lattice with the spacing of half the light's wavelength λ. A short pulse of that lattice imprints a phase structure on the condensate which is equivalent to exciting a momentum mode at $p = \hbar k = \frac{4\pi}{\lambda}$. Due to the momentum, part of the atoms are ejected from the condensate with $v = p/m$. Their movement can be traced with time of flight measurements. Since the atoms' velocity is known very precisely from the wavelength of the light, the magnification can be inferred. The magnification is 35-fold magnification, and a single pixel on the camera's CCD chip corresponds to 0.455 μm in the condensate. The optical resolution is around 0.8μm.

6.6 Magneto-optical traps

Cooling of the atoms begins with the magneto-optical traps. In the 'high-pressure' part of the vacuum cell (see section 6.3), a 2d-MOT is loaded from the background vapor pressure. It creates an atom beam that, in turn, loads the 3d-MOT. The 3d-MOT is the starting point for later cooling stages and, ultimately, the Bose-Einstein condensate. For potassium-39, closed cooling cycles in an MOT can be realized for the D2 line with light red-detuned to the $F = 2 \rightarrow F' = 3$ transition. However, due to the poorly resolved hyperfine manifold (see section 5.1), atoms are likely to be lost into the $F = 1$ ground state and need to be re-excited by the repumper transition from the $F = 1$ ground state to the excited state manifold. For optimal cooling, cooler and repumper light must be overlapped in all MOT beams with almost equal intensity such that both lights contribute to the cooling forces (see section 5.8 for details).

6.6.1 Two-dimensional MOT

The 2d-MOT is built as a four-beam (non-retro-reflected), free space setup with an additional push beam. A schematic sketch can be found in fig. 6.7 and appendix A.3 shows the detailed setup. The magnetic quadrupole field for the MOT is created by the dedicated coils described in section 6.4. For the 2d-MOT beams, around 350 mW of mixed D2-cooler and D2-repumper light are used. Both lights are red-detuned to

[8] Uniblitz optical shutter, the camera internal shutter was removed to avoid vibrations

the entire excited state manifold with the exact detunings shown in fig. 6.8. The light is split into the four MOT beams, which are collimated with telescopes to a $1/e^2$-diameters of 15 mm. The polarization of the beams is adjusted with $\lambda/4$-plates to be left-handed circular polarized for the horizontal beams and right-handed circular polarized for the vertical beams in accordance with the orientation of the quadrupole field.[9] This setup creates an elongated cloud of atoms that are cooled and trapped in two spatial directions but can propagate freely in the third direction. A push beam blocks the propagation in one direction such that the atoms move towards the low-pressure region of the vacuum chamber. The light for the push beam arrives at the table in a separate optical fiber. It contains 8 mW cooler light and no repumper light. It has a beamwidth of 2 mm and is adjusted to left-handed polarization. The resulting atom-beam passes through the differential pumping stage described in section 6.3 and loads the 3d-MOT. Loading efficiency can be significantly improved with the power-balancing between counter-propagating beams and the pointing of the push-beam.

6.6.2 Three-dimensional MOT

The 3d-MOT uses a circularly symmetric magnetic quadrupole field created with the large coils described in 6.4. For the MOT, the magnetic field gradient is 7.5 G/cm in gravity direction and 3.8 G/cm in the radial direction. Similar to the 2d-MOT, the 3d-MOT is realized with three pairs of counter-propagating free space beams that overlap at the minimum of the magnetic quadrupole field. In total, the six beams contain a power of 25 mW of D2 cooler and 20 mW of D2 repumper light with a $1/e^2$-beam diameter of 13.5 mm. The horizontal beams are adjusted to a left-handed circular polarization and the vertical beams to right-handed polarization. The schematic setup for the horizontal beams is shown in fig. 6.7 with the details in the appendix appendix A.1. The vertical beams require a more complicated setup because the main imaging setup shares their propagation axis. This places an objective in the path of the lower MOT beam, as is shown in fig. 6.6. The other way around, a MOT mirror blocks the path of the imaging beam. The imaging setup is kept static to minimize shot-to-shot fluctuations and signal loss for the imaging. This means that the optical components of the lower MOT beam must be moved during each experimental cycle. For the MOT phase, a lens is moved into the beam path to compensate for the focusing effect of the objective, and a MOT mirror is moved

[9] There are different conventions for naming the handedness of the polarization. For this work, we use the definition of an observer that looks into the beam (against the propagation direction) following the polarization analyzer used for measurements (Polarization Analyzer SK010PA, Schäfter-Kirchhoff)

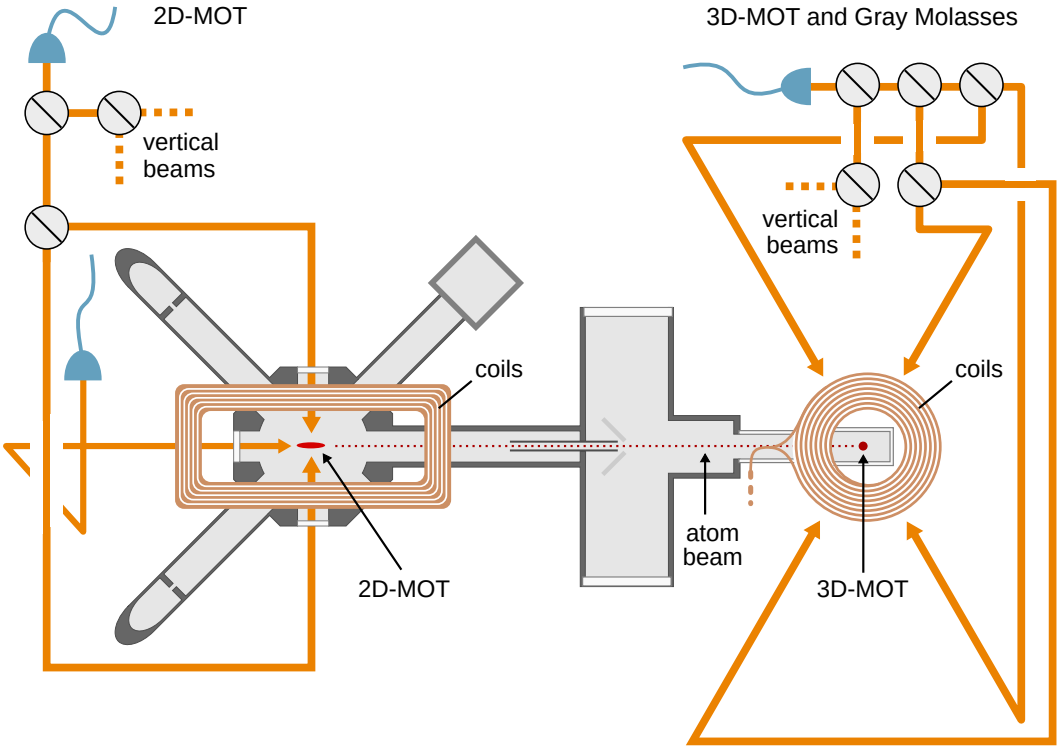

Figure 6.7: Setup for magneto-optical traps. Both 2d-MOT and 3d-MOT are realized in a free space set up with four and six independent beams, respectively. The 2d-MOT has an additional push beam that keeps atoms from escaping the 2d-MOT in the unwanted direction. The atoms then form a beam propagating from the 2d-MOT to the 3d-MOT. The setup of the vertical 3d-MOT beams is in fig. 6.6, and a detailed drawing of the MOT setups can be found in appendix A.1.

out of the imaging path at the end of the molasses phase. Both movable components are mounted on air-pressure-driven stages.[10] The air-pressure stages were chosen because they can move without magnetic components, which could influence the atoms during experiments.

6.6.3 Compressed MOT

The previously described MOT stage is optimized to collect and precool as many atoms as possible. This requires a large trapping region and strong trapping forces.

[10] air pressure mini stage: Festo, DGST-8-80-Y12A (magnetic position indicators are removed), magnetic valve: Festo, VUVG-L10_M52-MT-M5-1R8L. The stage contains a magnet for position sensing, which we removed for our purpose

The density of the atom cloud is limited by photon rescattering and light-assisted collisions, and the temperature of the cloud is limited by the photon scattering itself.

Once the atoms are trapped in the MOT, the cloud's density is increased during a 5 ms compressed MOT. For the compression, the magnetic field gradient is increased by a factor of 4, which results in tighter confinement. The detunings of cooler and repumper light are changed to the configuration shown in fig. 6.8. It results in a more compact and colder cloud. At the end of the stage, the cloud has a temperature of approximately $500\,\mu$K. The temperature is determined with time-of-flight measurements using the Guppy absorption imaging[11]. At the end of the compressed MOT, the D2 lights and the magnetic field are turned off for the grey molasses stage. The MOT stage and compressed MOT are included in the sketch of the experimental sequence fig. 6.9.

6.7 Grey molasses

A grey molasses as described in section 5.10 can be realized in potassium-39 on the D1 transition. It needs cooler and repumper light in a Raman condition and requires a light field with polarization gradients. The beam setup for the magneto-optical trap with three pairs of circularly polarized light creates such a polarization gradient field. Thus, the same beam setup used for the MOT can be reused for molasses. For that purpose, D1 light is coupled into the same optical fiber as the MOT-lights (as described in section 6.10.1). Optimal cooling is achieved for an intensity ratio between cooler and repumper of 3 : 1. In total, we use around 25 mW of D1 cooler light and 8 mW of D1 repumper light, which is distributed between the six beams. The efficiency of the grey molasses is very sensitive to magnetic fields. For cooling to proceed, the gradient field for the MOT is turned off, and residual magnetic fields are compensated with the offset coils (see section 6.4).

While cooling is very efficient during the molasses, this process cannot offer spatial confinement, and the atom cloud expands and loses density. To limit this effect, the entire molasses stage only last 4 ms. In the first 1.5 ms, light intensities and detunings are held at a constant value to achieve high cooling forces. During the next 2.3ms, the frequencies of both lights are swept to larger detuning, and intensities are lowered as illustrated in fig. 6.9. This reduces heating due to photon scattering, and lower final temperatures can be reached. The most critical parameter in the

[11]The time-of-flight measurements are not very precise at this point. There is a necessary time gap between the end of the MOT and imaging to allow the magnetic fields of the MOT to turn off. Due to the still high temperatures, the atom cloud already expands significantly and is already too large in size for the camera setup designed to image colder clouds.

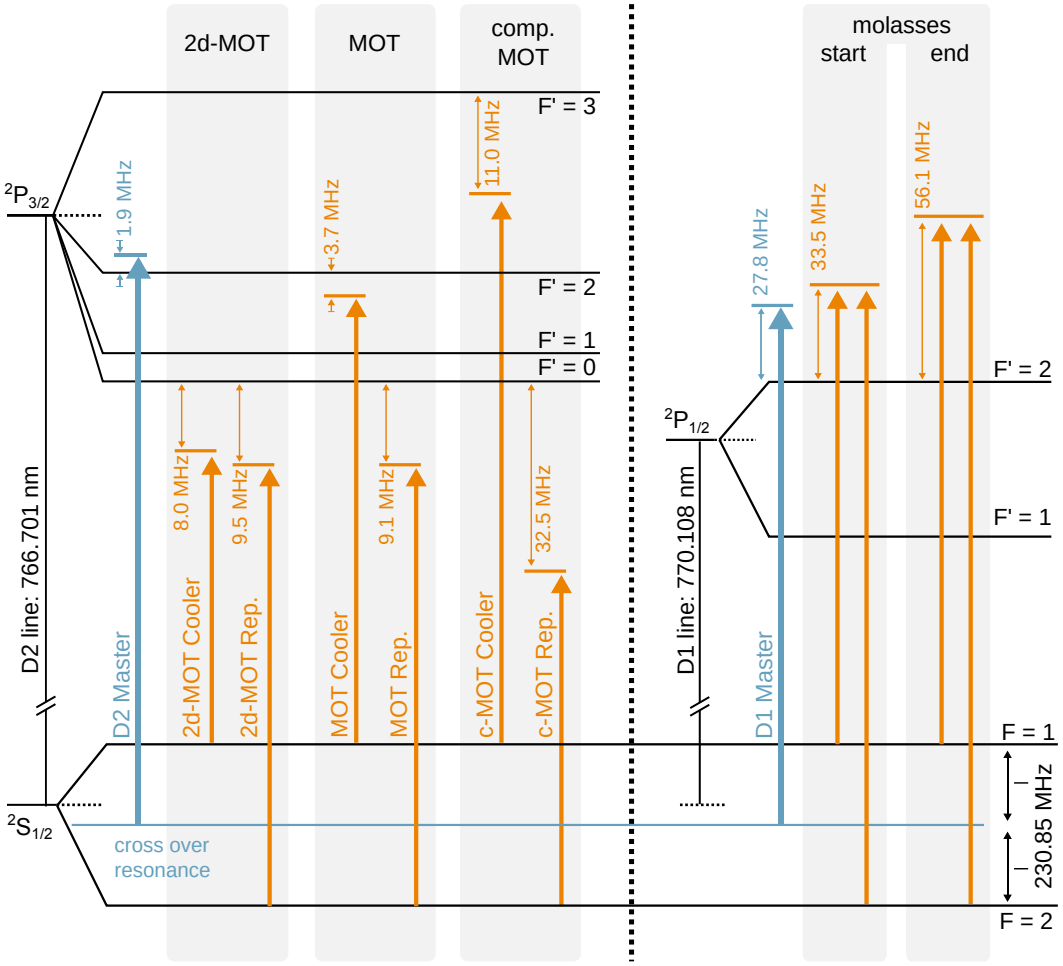

Figure 6.8: Laser detunings for MOT and molasses. The magneto-optical traps use the D2 transition, with different detunings for 2d-MOT, 3d-MOT, and compressed MOT. The frequency of the D2 and D1 master lasers are shown in blue. The grey molasses uses the D1 transition with cooler and repumper in a Raman condition. Optimal cooling is reached by a sweep of the detunings, the start and end values of which are indicated.

molasses is the Raman condition. Special care is taken to keep this condition fulfilled during the frequency sweeps. This is described in detail in the section on the laser system section 6.10.1. Temperatures down to around $6\,\mu$K have been achieved in our experiment, and even without frequent adjustments, temperatures are reliably between $6\,\mu\text{K} - 10\,\mu\text{K}$. In the last 0.2 ms of the molasses stage, the D1 cooler light is turned off, which transfers the atoms to the $F = 1$ ground state.

The end of the molasses marks the end of the cooling processes using resonant light. For the following cooling stages, resonant light must be blocked from the experimental chamber since already very low intensities of resonant light lead to significant heating during the long evaporative ramps. For that reason, the resonant laser system is located on a separate, shielded optical table, and the light reaches the table only via optical fibers. At this point in the sequence, mechanical shutters close before the 2d-MOT and 3d-MOT fibers and effectively prevent resonant light from reaching the atoms.

6.8 Magnetic trap

The magnetic trap selects a single atomic sub-state. Additionally, it is used as a transition trap to catch and hold the atoms after the molasses and help the loading of the dipole traps described in the following section[12].

The depumping at the end of the grey molasses leaves the atoms in the $F = 1$ ground state with equal populations in the three $m_F = [-1, 0, 1]$ sub-states. The magnetic trap catches the $m_F = -1$ state, which is a magnetic low-field seeker (see section 5.2) and is thus trapped in the magnetic field minimum of the magnetic quadrupole field. The other two states are anti-trapped, the $m_F = 1$ state already due to the linear Zeeman effect and the $m_F = 0$ state due to the quadratic Zeeman shift. This means that two-thirds of the carefully collected and cooled atoms are lost and fall under the influence of gravity. The remaining third, however, is a one-component atomic gas needed for evaporative cooling and the final condensate.

The offset coils are used to shift the magnetic field minimum to the position of the molasses cloud. Slow ramps of the offset field move the magnetic field to the position of the dipole traps. The magnetic trap can compensate for slight misalignment between molasses and dipole traps.

[12]Loading the dipole traps directly from the grey molasses is difficult due to the light shift induced by the dipole traps themselves. The light shift changes the detuning of the D1 lights at the position of the dipole beams. For deep traps, the detuning might even change from blue-detuned to red-detuned. The atom cloud will then be cooled outside of the traps but heated in the traps.

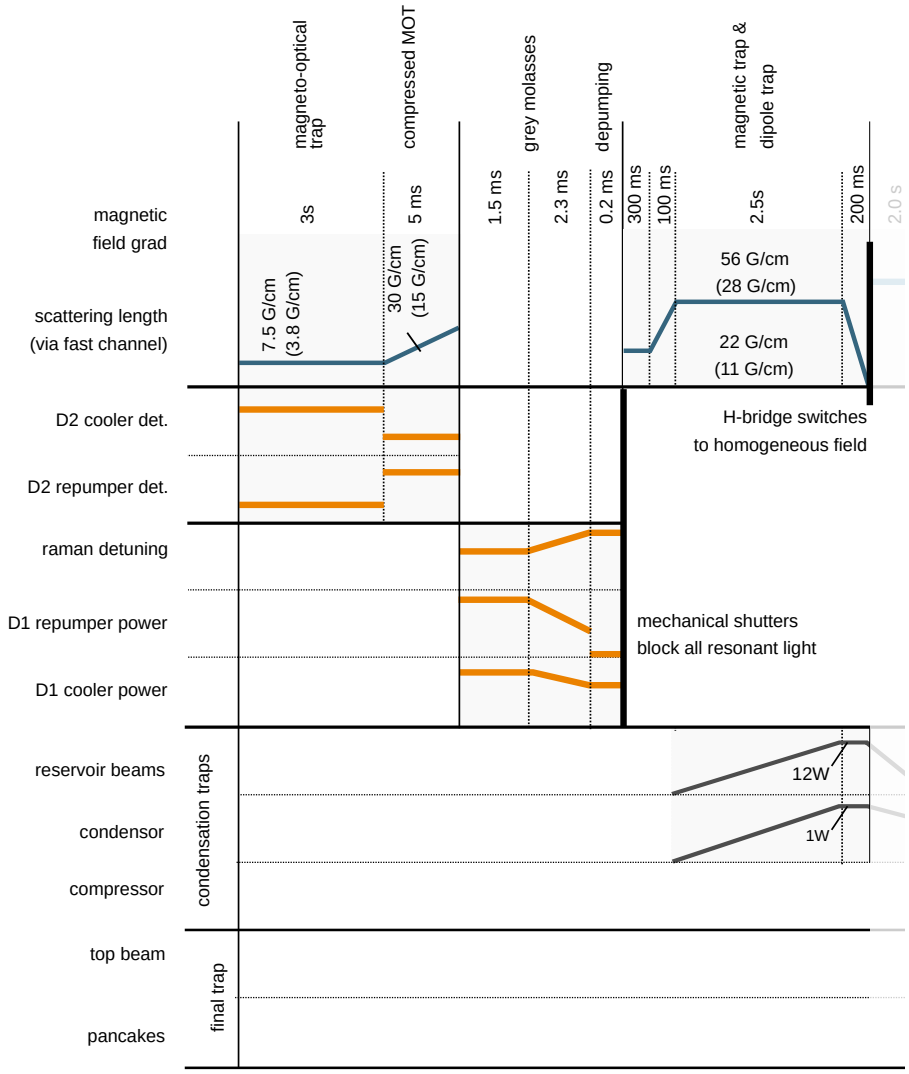

Figure 6.9: Experimental sequence - MOT, molasses, magnetic trap and loading of the dipole trap. The sequence starts with an MOT followed by a compressed MOT. For the latter, the frequencies switch to the values indicated in fig. 6.8, and the magnetic field gradient increases linearly. For the grey molasses, detunings and power of D1 cooler and repumper are first held static. A sweep to higher detunings and lower intensities further decreases the temperature of the atomic cloud. The repumper switches off 0.2 ms before the cooler to transfer all atoms into the $F = 1$ ground state. A magnetic trap catches and compresses atoms in the $F = 1$, $m_F = -1$ state. A transfer of the atoms into the dipole traps is achieved by a slow increase of the power in the reservoir beams and the condenser. Once they reached full power, the magnetic trap ramps down and turns off.

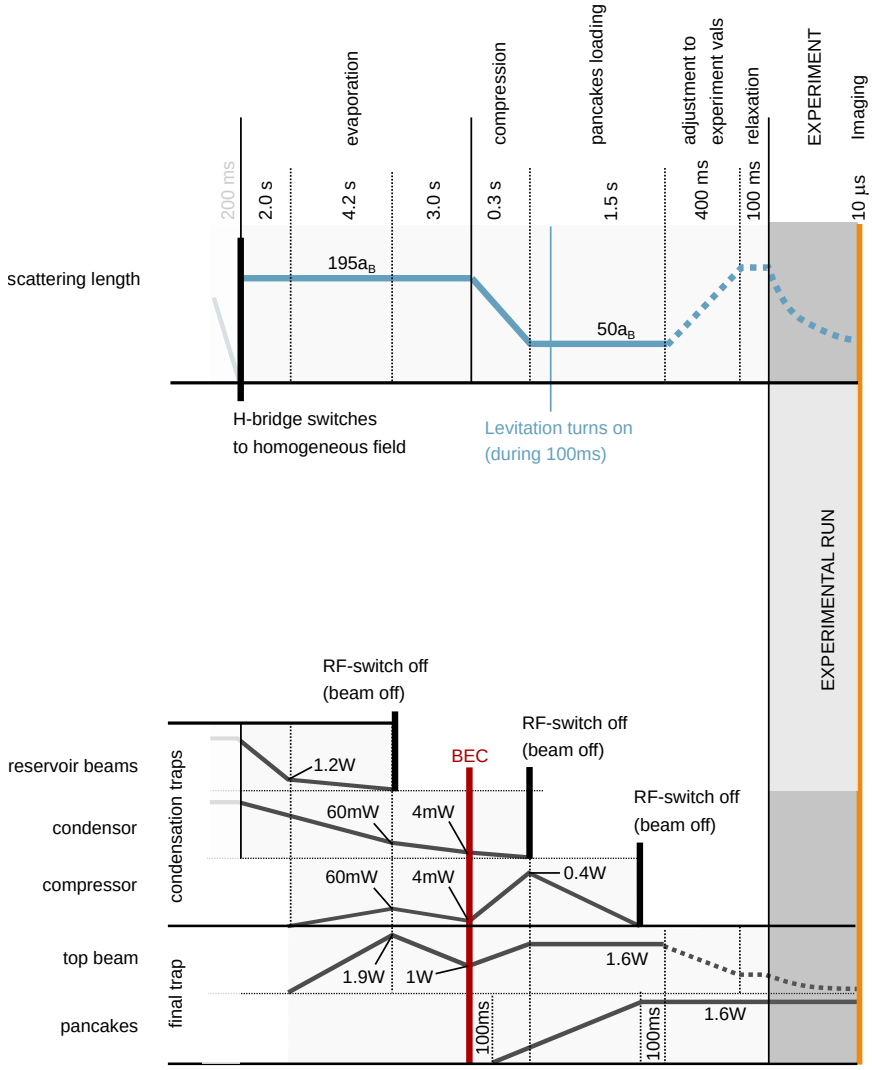

Figure 6.10: Experimental sequence - evaporation and loading of the final trap. Once the dipole traps are loaded, the magnetic field switches to the Helmholtz configuration for a homogeneous field. Evaporation proceeds at a scattering length of 195 a_B. The ramps of different dipole beams are optimized for cooling while maintaining high densities within the cloud. Once the condensate has formed, it is compressed in gravity direction by increasing the compressor's power and then loaded into the pancake trap. The atoms are then only held between the top beam and the pancakes, which results in the desired quasi-two-dimensional, circular symmetric condensate. Finally, the top beam and scattering length are adjusted to the values of the experimental run.

Once the magnetic trap is loaded, a slow increase of the gradient of the quadrupole field compresses the atomic cloud adiabatically (see fig. 6.9), which leads to a higher density but also increases the temperature to typically $50 - 60\,\mu$K. After the compression, the atoms are transferred into a dipole trap described in more detail in the following section. While the magnetic trap is held static, the intensity of the dipole trap is slowly increased during a 2 s period. The majority of the atoms are then confined by the dipole traps, and a slow turnoff of the magnetic trap concludes the transfer. Once the atoms are trapped in the light-field of the dipole traps, the orientation of the large coils is switched from the gradient configuration to the homogeneous field configuration. The homogeneous field is necessary for Feshbach-tuning during evaporative cooling.

6.9 Dipole traps

In our setup, dipole traps fulfill different purposes. First, they provide confinement during evaporative cooling until the phase transition to the Bose-Einstein condensate takes place. Second, dipole traps create the trap geometry that holds the quasi-two-dimensional, rotational symmetric condensate. Finally, a tightly-focused repulsive Gaussian beam is used for curvature measurements described in chapter 8 to introduce a local under-density in the condensate.

The evaporation trap is formed by overlapping several red-detuned, attractive Gaussian beams with a wavelength of 1064 nm as described in section 5.7. The power of the beams is actively stabilized (see 6.10) and can be dynamically adjusted via the experiment control. For the final trap, the tight confinement in gravity direction is achieved with a repulsive pancake interferometer at 532 nm. Radial confinement is provided by an additional attractive Gaussian beam perpendicular to the pancakes.

6.9.1 Evaporation traps

For evaporative cooling, a trap needs to initially hold a large cloud of atoms. It thus requires a large trapping volume and a good overlap with the magnetic trap from where it loads the atoms. Additionally, the initial dipole trap needs to be deep enough to confine atoms at the corresponding temperature. During evaporative cooling, the intensity in the trapping light field beams must be decreased. This will lead to a more shallow trap which in turn lowers the density of the atoms. This effect is unwanted since evaporation is more efficient at high densities. Also, a high density is crucial for condensation itself, which occurs a critical phase-space density.

To combine a large initial cloud with high densities during the cooling process, the evaporation trap consists of a large trap region, called *reservoir trap*, overlapped by a tighter trap. The reservoir is created by two attractive Gaussian beams that are crossed under an angle of 10° degrees (see fig. 6.11). Lenses with a focal length of $f = 600\,\mathrm{mm}$ focus both beams to a beam waist of $50\,\mu\mathrm{m}$. Each beam contains up to 12 W of laser power. Both beams combined a trap with approximately 700 nK trap depth. Since a single-mode optical fiber cannot transport such high powers, the reservoir beams are free-space beams. The tighter trap is again formed by two crossed laser beams called *condenser* and *compressor*. The beams are in the same vertical plane and intersect at the positions of the atoms under a 10° angle. Hereby, the compressor is in the horizontal plane and the condenser tilted downwards at the specified angle. Both beams are fiber coupled with a maximal power of 2 W each. The compressor is spherically shaped with a beam waist of $35\,\mu\mathrm{m}$. The compressor is flattened in vertical direction, with a beam waist of $17\,\mu\mathrm{m}$ and $51\,\mu\mathrm{m}$, respectively (surfboard geometry). The tighter waist in the vertical direction facilitates the loading of the final trap. Figure 6.13 shows recorded cross-sections of the light field of the compressor and condenser in comparison to the pancake trap.

The evaporation sequence is illustrated on the left-hand side of fig. 6.10. In a 2 s-ramp, the power of the reservoir trap decreases to 10% of its original power while the condenser remains at full loading power. The cooling atom cloud collapses into the trap minimum around the condenser, increasing the density of the atoms. During a second 4.2 s ramp, the reservoir traps turns off completely. Simultaneously, the compressor ramps up to ensure tight confinement despite the lowered trap depth. At the same time, a beam of the final trap turns on already - the *top beam* (see following section). The top beam is not necessary for condensation. However, loading of the final trap is easier if this beam already contributes to the evaporation. If turned on, it already moves the trap minimum to the correct position for later loading. Compressor, condenser, and top beam decrease their power in a third and final ramp until the atoms reach degeneracy.

6.9.2 Final trap

To create a quasi-two-dimensional, circular symmetric condensate, the final trap needs circular symmetric confinement in the horizontal plane and tight confinement in the gravity direction. The latter is achieved with a repulsive pancake trap (see 5.7). In our setup, the interferometer is realized with blue-detuned $\lambda = 532\mathrm{nm}$ light. To reach a spacing between the pancake sheets of $\Delta z = 5\mu\mathrm{m}$, two beams are crossed at an angle of 6°. They are Gaussian beams with a $1/e^2$-diameter of

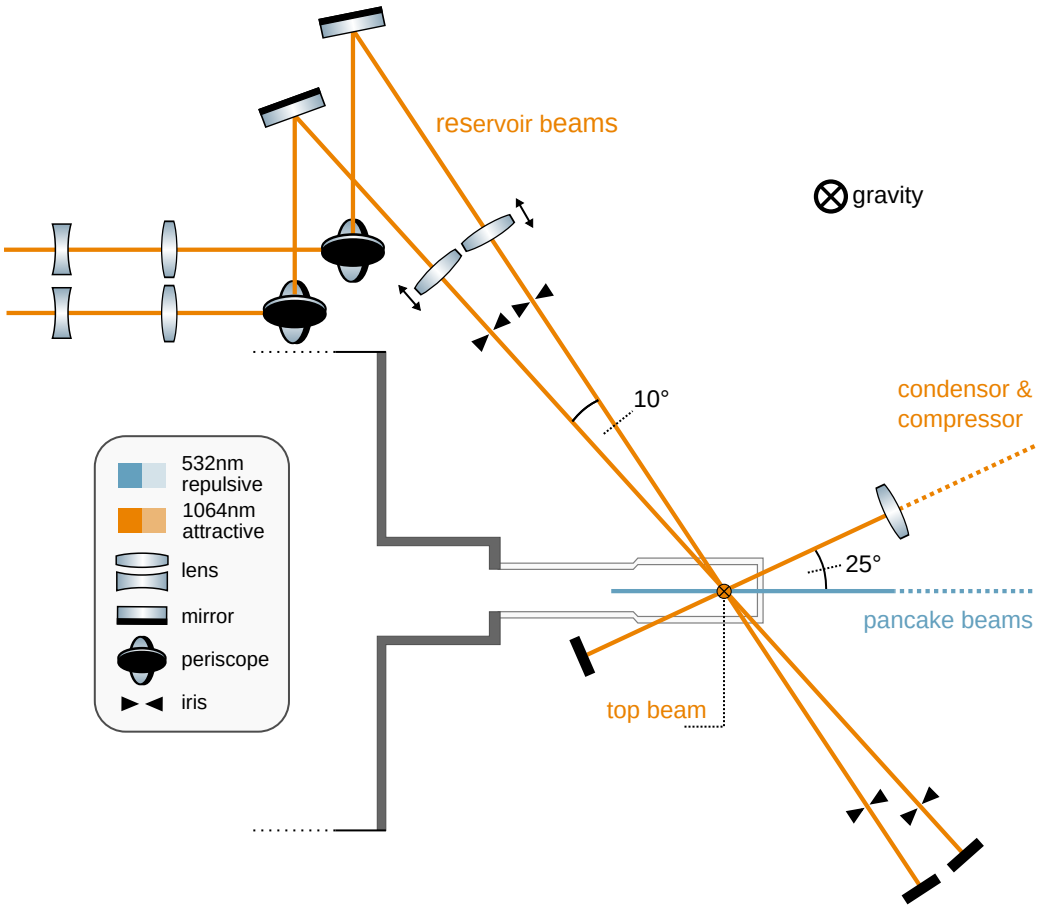

Figure 6.11: Dipole traps - view from the top. The two reservoir beams form a large and deep trap for loading a large atomic cloud from the magnetic trap. During evaporation, the condenser and compressor beams provide a locally tighter trap which increases the density of the cloud. The final trap is created by the pancake interferometer and the top beam.

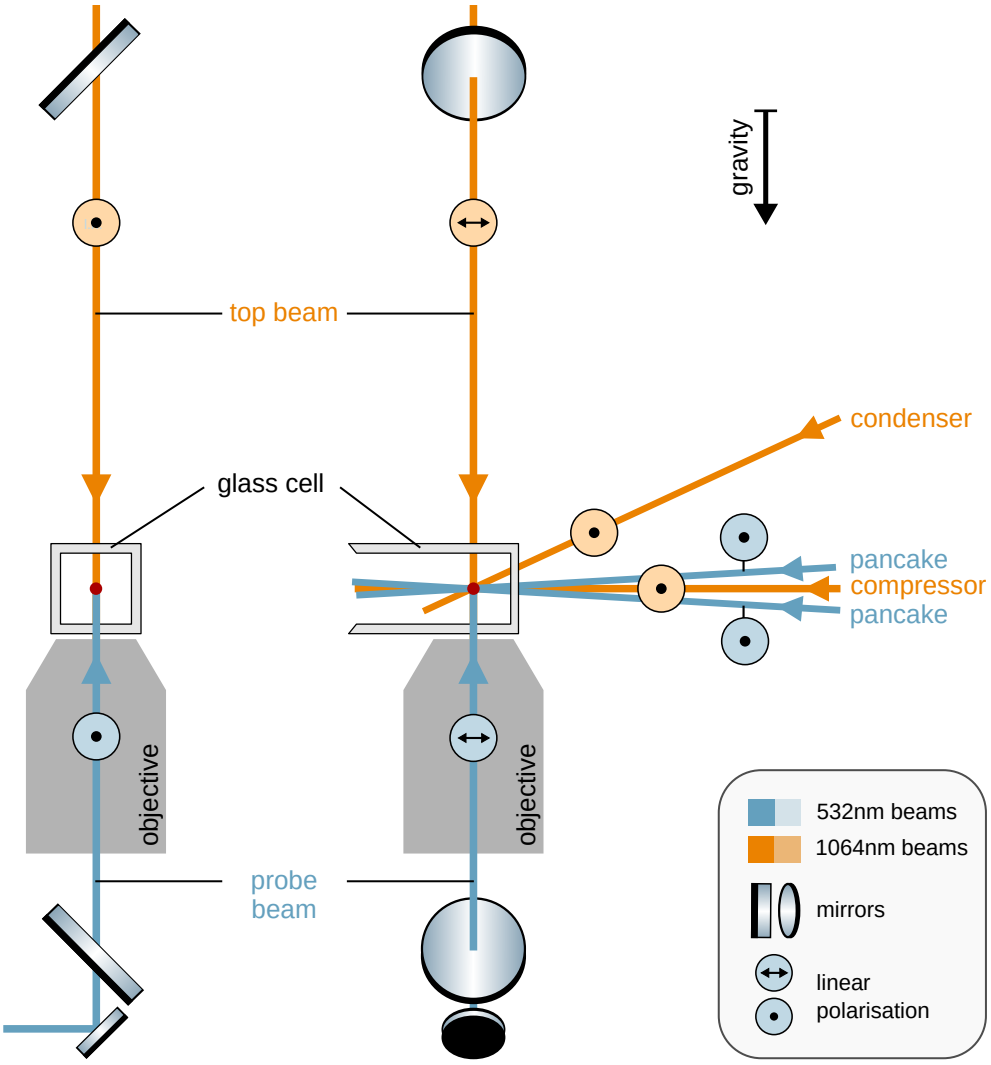

Figure 6.12: Dipole traps - view from the front and the side. This view shows the orientation of the pancake interferometer and the attractive beams. The top beam passes through a mirror which reflects the imaging and MOT light. From the bottom enters the probe beam, again through a mirror for the MOT and imaging lights. The reservoir beams are not shown in this depiction; they would be in the horizontal plane.

1 mm. The maximal (stable) total power in the interferometer is $P = 1.6$W which is divided evenly between the two arms of the interferometer. This results in a trapping frequency in z-direction of $\omega_z = 2\pi \cdot 1.6\,\mathrm{kHz}$. In x and y direction, the trap is slightly repulsive due to the finite size of the beams. Numerical calculations of the horizontal trap frequencies are $\omega_x = 2\pi \cdot 0.5\,\mathrm{Hz}$ and $\omega_y = 2\pi \cdot 8\,\mathrm{Hz}$, for perfectly aligned beams. The true values are probably lower due to minor misalignment of the beams.

The radial confinement in the final trap is provided by an attractive Gaussian beam called *top beam*. In future versions of the experiment, this beam will be replaced by a digital micromirror device to shape arbitrary potentials [61, 66]. The top beam was implemented as a makeshift solution, and its exact size at the focus is unknown. It has a maximum power of 2 W. The important parameter of the radial trap - the trap frequency - is determined experimentally (see section 6.9.4).

For a better loading of the final trap from the evaporation trap, the top beam is already turned on during the final evaporation ramp. For the loading itself, first, the power of the compressor is increased, and the condenser is turned off, as is depicted in fig. 6.10. This flattens the BEC along gravity direction and allows to load a single pancake, i.e., to transfer all atoms between two light sheets of the pancake trap. Figure 6.14 shows an absorption image of the atoms taken from the side with the Pixis imaging (see section 6.5) without the stage of compression. Here, several pancakes are loaded. Only with the compression stage the loading of a single pancake becomes possible. Once the pancake trap is at full power, the compressor power slowly decreases to zero, and the beam turns off. The atoms are now held only in the top beam and the pancake trap. The condensate preparation is concluded by a waiting time of 100 ms to let the atoms settle into the trap. The condensate is now ready for experiments.

6.9.3 Stability of the dipole traps - the wedge

For loading a single pancake, the minimum between two light sheets must coincide with the position of the atoms in the evaporation trap. For that purpose, the relative position between the compressor, condenser, and the sheets of the pancake trap must be precisely adjusted. Additionally, the beams must be very stable with respect to each other. In our setup, stability is achieved by mounting the beam setups on a solid and heavy block of aluminum. The block itself is connected to the optical table by only three spheres to decouple it from vibrations of the table (see fig. 6.15). The block is cut in the shape of a wedge with an angle of 25°. On both sides, 2 cm thick aluminum plates are attached. The first plate carries the setup for the pancake interferometer. The plate's position can be coarsely adjusted and is then fixed to the

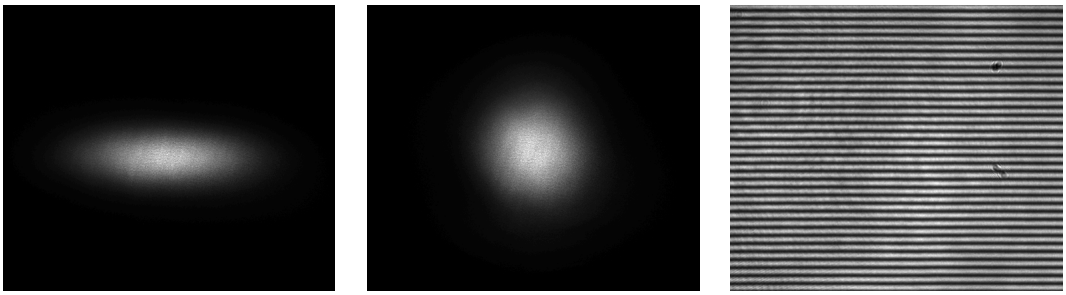

Figure 6.13: Beam profiles of the compressor, condenser, and pancake trap. The light distribution of the three beams is recorded at the position of their overlap. These are the three beams mounted on the wedge (see section 6.9.3). The images were taken before installing the wedge in the experiment. For each image, only one of the beams is turned on. From left to right: compressor, condenser, and the pancake trap's interference pattern. The spacing of the light-sheets is approximately 5 μm. (The ring-structures appearing on the pancake trap are dust artifacts.)

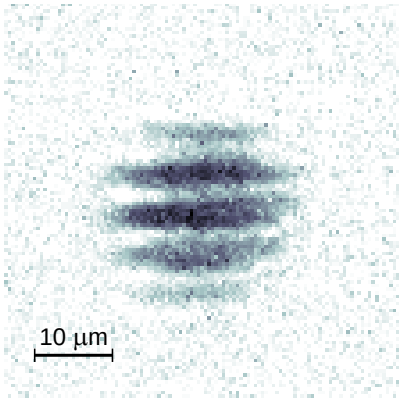

Figure 6.14: Atoms in the pancake trap without compression. Density distribution of the atoms in the final trap inferred from absorption image with the Pixis camera. Regions of higher density are darker. Without compression, several pancakes are loaded as shown here. With the compression stage, only one pancake is loaded.

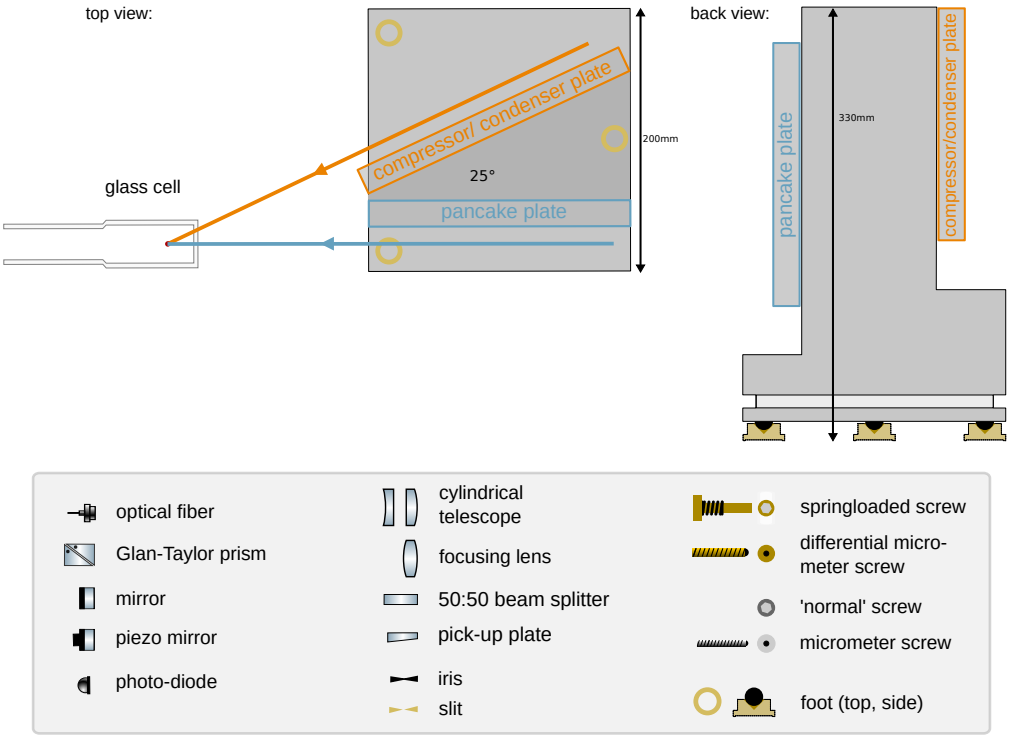

Figure 6.15: Mounting of pancake trap, compressor, and condenser. To ensure the stability of the final trap and its loading, the pancake interferometer and the compressor and condenser beams are mounted on a solid block of aluminum. The block itself is cut into a wedge shape and is connected to the table only by three press-fitted spheres into the aluminum block. Each sphere rests on a custom-made foot with a v-shaped cutout which can be fixed to the table with a clamp. This decouples the aluminum block from vibrations of the table. Plates are mounted on each side of the block. They carry the setups for the pancake interferometer, and the compressor and condenser, respectively. The wedge is cut such that all beams overlap in the region of the atoms in the glass cell. The following page shows the detailed setup of both plates. The insets indicate the direction of view (black arrows).

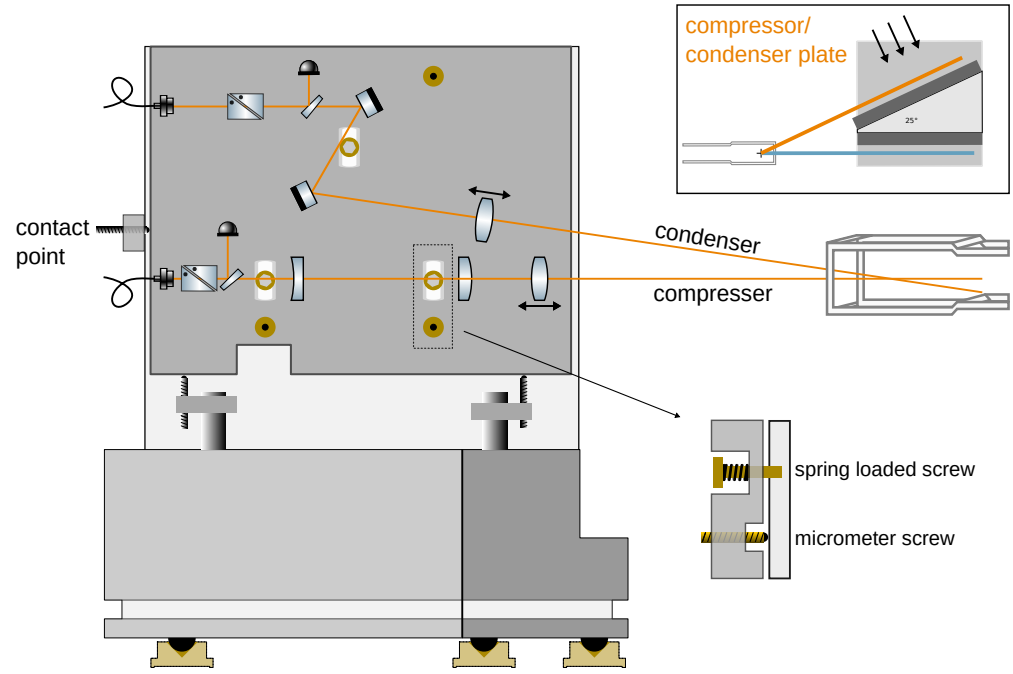
compressor/
condenser plate
25°
contact
point
condenser
compresser
spring loaded screw
micrometer screw

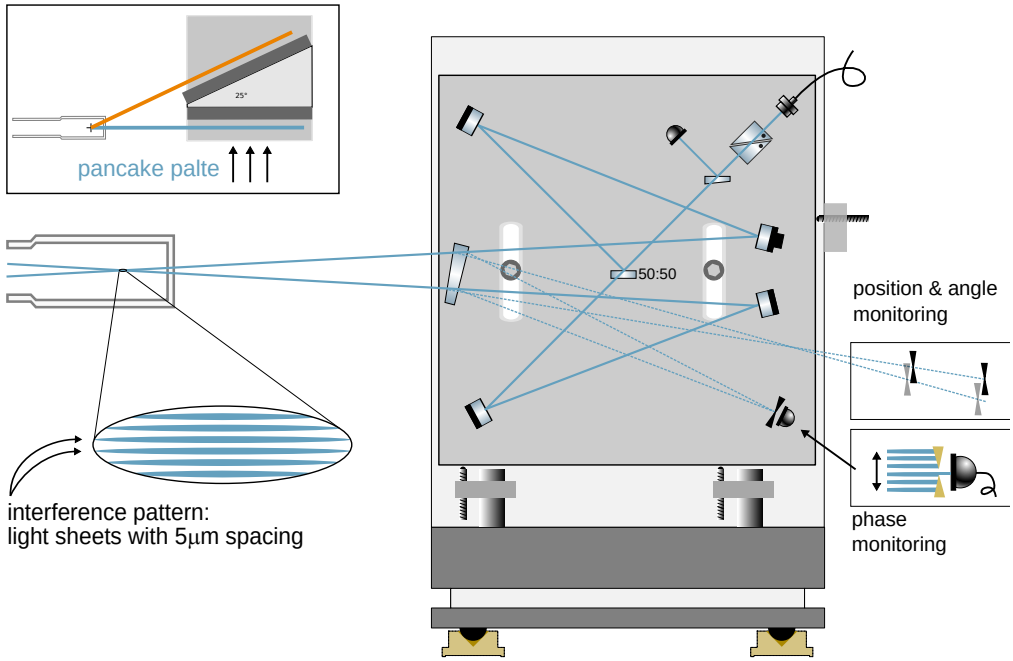
25°
pancake palte
50:50
position & angle
monitoring
phase
monitoring
interference pattern:
light sheets with 5µm spacing

wedge with the two central screws. Fine adjustment is achieved with the mirrors of the interferometer. The path length of one of the beams can be changed by a piezo mirror. This permits a precise adjustment of the relative phase between the arms of the interferometer, which shifts the interference pattern up and down (see section 5.7). The minimum between two light sheets is centered on the atomic cloud by a fine adjustment of the piezo mirror.

The second plate contains the setup for the compressor and condenser. The position and angle of the wedge are chosen such that the beams overlap with the pancake trap in the region of the atoms. For fine adjustments, the entire mounting plate can be moved. The plate rests on two micromirror screws[13] which allow vertical movement and tilt. For the remaining two axes, movements and tilts are realized by a combination of spring-loaded screws that push the plate towards the wedge and differential micrometer screws[14] that act against that push. Adjustments of the micrometer screws thus move and tilt the plate. This is similar to the front plate of a mirror holder. A contact point at the back of the plate completes the setup. Additionally, the condenser can be adjusted with mirrors to overlap the two beams of this plate. Also, their focus positions are adjusted independently via the focusing lenses, which are mounted on small manual translation stages[15].

The setup is passively stable. Only on the time scale of several weeks a readjustment of the piezo mirror is necessary to correct for relative drifts in the position of the pancakes relative to the atoms.

6.9.4 Characterization of the final trap

For the experiments described in chapter 8 and chapter 10, the parameters of the final trap, namely the trap frequencies, are important. They are best measured by once again using the condensate itself. For measuring the frequencies in the radial directions, a short pulse with the magnetic gradient wires (see section 6.4) displaces the atoms from the center of the trap. Afterward, the condensate oscillates with the trap frequency. Such a measurement is shown in fig. 6.16 at a high intensity of the top beam of $I = 1\,\mathrm{W}$. For lower intensities, the trap frequency decreases approximately with the square root of the intensity.

For measuring the trap frequency in the gravity direction, direct oscillations are hard to observe in the tight trap. The amplitude of the oscillations is too low to be well resolved by the imaging. Instead, we modulated the pancake trap at different

[13] Thorlabs: APM03/M - adjustable kinematic positioner
[14] Thorlabs: DM10 - differential adjuster for translation stages, 1/2" Travel
[15] Thorlabs: MS1S/M - 6.5 mm travel single-axis translation stage

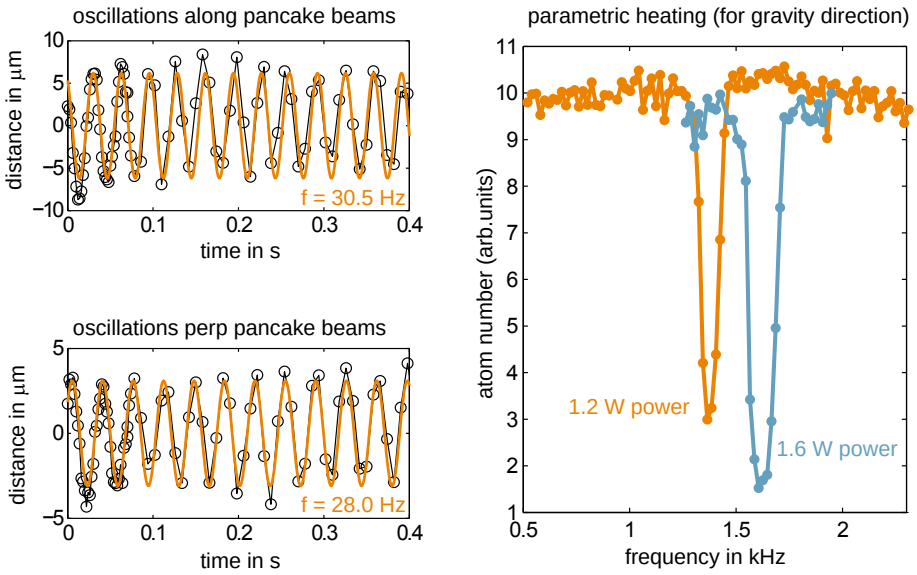

Figure 6.16: Trap frequency measurements for the final trap. For the trap frequency measurement in radial directions, a short pulse with the magnetic field gradients displaces the atoms inside the trap, and the subsequent oscillations are recorded (left-hand side). In gravity direction, the trap frequency is measured with parametric heating. The pancakes are modulated, and atoms are excited and lost from the trap on resonance with the trap frequency The right-hand side shows the resonance for two different powers in the pancake interferometer. For the experiments, the total power of 1.6 W is used (blue line).

frequencies. Resonance at the trap frequency leads to parametric heating, and atoms are lost. If the number of remaining atoms is imaged for different modulation frequencies, the resonance is visible. This is shown on the right-hand side of fig. 6.16 for two different powers in the pancake interferometer. For later measurements, the power of 1.6 W is used, which corresponds to the trap frequency of $\omega = 2\pi \cdot 1.6\,\mathrm{kHz}$.

6.9.5 Probe beam

A final dipole beam will be needed for curvature measurements in chapter 8, where it is used to create a local under-density. The beam is blue-detuned to the potassium-39 resonance with a wavelength of 532 nm and a beam waist of $\sim 5\,\mu$m by design. The beam enters the setup around the glass cell from the very bottom as shown in fig. 6.12 and is focused on the atoms by the imaging objective itself. When in use, the probe beam turns on simultaneously with the pancake trap. In contrast to the other dipole beams, it is not actively power-stabilized.

6.10 Laser systems

The experimental setup comprises a total of four laser systems. Two of them have resonant light. The first creates the light for the magneto-optical traps and the grey molasses, and the second produces the imaging lights. In total, they contain four lasers;[16] two frequency stabilized master lasers for the D1 and D2 line and two imaging lasers which are offset-locked onto the D2 master. The master lasers are the ones used for MOT and molasses. The resonant laser systems are located on a separate, shielded optical table to keep unwanted resonant light away from the atoms. In addition, there are two high-power setups for the dipole traps, one with 1064 nm light[17] for the attractive beams and one with 532 nm light[18] for the repulsive pancake trap which are both located on the main experiment table.

6.10.1 Laser system for MOT and grey molasses

For the magneto-optical trap and the grey molasses, two master lasers are locked on the D2 and D1 transitions at 770 nm and 766 nm. Frequency stabilization is achieved using Doppler-free absorption spectroscopy [90, 91]. Both lasers are locked on the same spectroscopy cell containing potassium vapor. The exact setup can be found in appendix A.2 and in [92]. An error signal is created by applying a magnetic field to the atoms in the spectroscopy cell. The magnetic field strength is modulated at a frequency of 86 kHz. Lock-in amplifiers selectively enhance the absorption signal at that frequency. For the correct choice of the phase parameter in the lock-in amplifier, this yields the derivative of the absorption signal, which is an error signal. This is used as the input signal for a proportional-integral controller regulating the length of the laser cavity and hence its frequency.

For the D2 line, the separation between the excited states is not large enough to resolve the different levels; all lines blend into one absorption line. In the Doppler-free absorption spectroscopy, the master laser is locked to the minimum of the ground state crossover resonance of that line. Drawn into the potassium level scheme fig. 6.8, this corresponds to a transition from the center between the two ground states to a point 1.9 MHz blue detuned of the $F' = 2$ state. For the D1-line, the laser is locked from the crossover of the ground state to a point 27.8 MHz blue detuned to the $F' = 2$ excited state.[19]

[16] External cavity diode lasers, Toptica, DL Pro

[17] 1064 nm laser: Coherent, Mephisto MOPA 55 W

[18] 532 nm laser: Coherent, Verdi V10

[19] the detuning is half the fine structure splitting of the excited state.

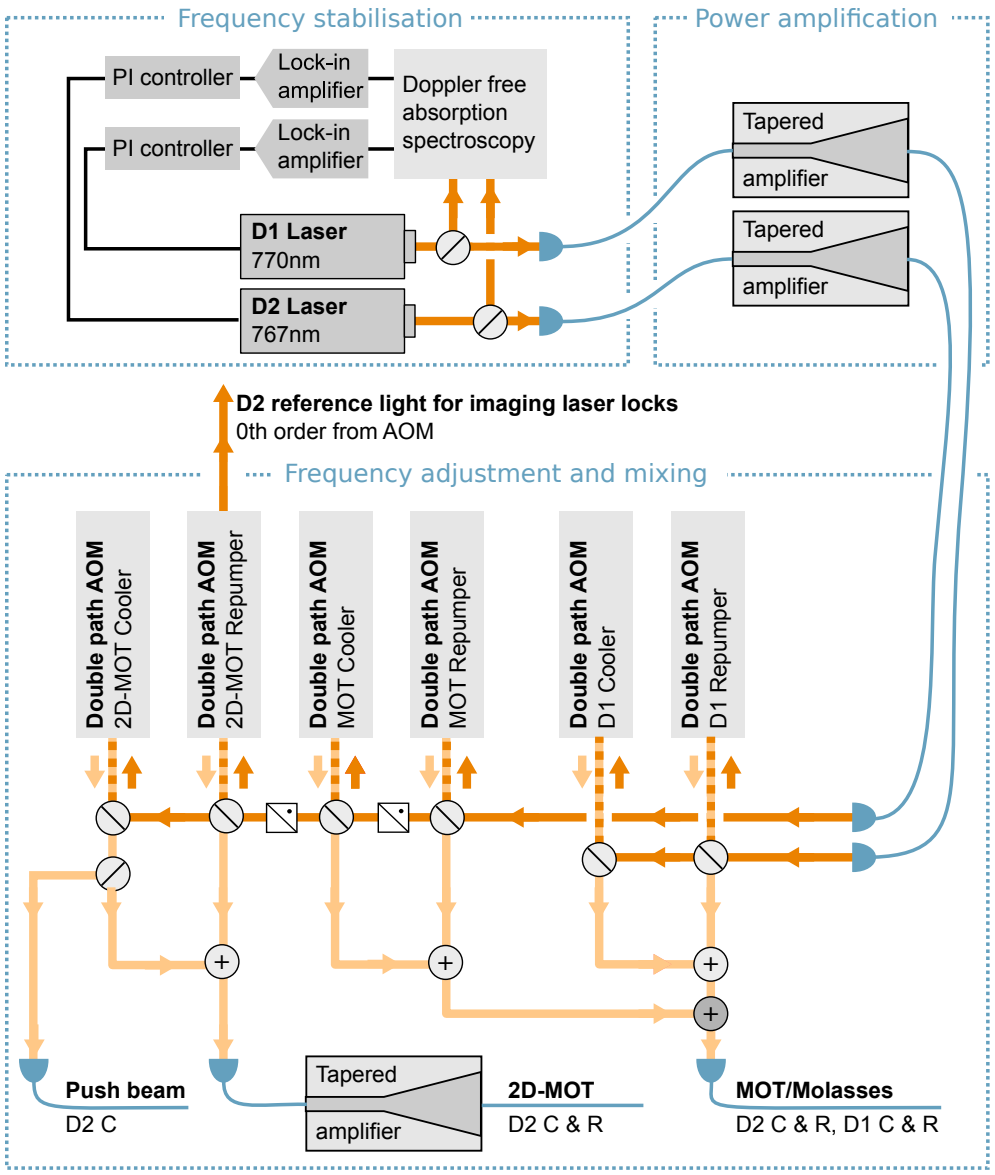

Figure 6.17: Laser system for MOT and molasses. Two master lasers are locked on the D1 and D2 lines, respectively, by Doppler-free absorption spectroscopy. Their light is amplified and the frequencies adjusted with acousto-optic modulators in a double-pass configuration. The cooler and repumper lights for 3d-MOT and molasses are all coupled into the same fiber using a tunable bandpass to combine D1 and D2 light. For the 2d-MOT, cooler and repumper lights are amplified with the same tapered amplifier. A push beam, containing only D2 cooler light, completes the setup. Laser detunings for all lights are illustrated in fig. 6.8 and a detailed drawing of the setup can be found in appendix A.2 and appendix A.3.

Home-built fiber-coupled tapered amplifiers then amplify the laser power of both master lasers (see [93] for the design and [92] an alignment strategy). After amplification, we get 650 mW power of D2 light and of 350 mW for the D1 light.

The fine adjustment of the laser frequencies proceeds with acousto-optic modulators[20] (AOMs) with a center frequency of 110 MHz. To adjust the frequencies for cooler and repumper lights for the 3d-MOT, the 2d-MOT, and the grey molasses, six AOM paths are needed. These are built in a double-pass setup in the cat-eye configuration (similar to [94]), which ensures a high-frequency bandwidth. The detailed setup of all six AOM paths including the consecutive mixing of the lights and coupling into fibers is shown schematically in appendix A.3 and in full detail in fig. 6.17. For 2d-MOT, 3d-MOT, and molasses, the respective cooler and repumper lights are mixed on non-polarizing 50-50 beamsplitters. The lights for the 3d-MOT and grey molasses are again combined on a tunable bandpass,[21] and all four lights are coupled into a single polarization-maintaining single-mode fiber. After the last fiber, we get around 30 mW for the D2 cooler, 20 mW for the D2 repumper, 25 mW for the D1 cooler and 8 mW for the D1 repumper.

For the 2d-MOT, the mixed cooler and repumper light is also coupled into a fiber and further amplified by one of the home-built tapered amplifiers. Simultaneous amplification of both lights is possible and yields stable intensities, as discussed in [92]. The simultaneous amplification creates sidebands that, however, do not seem to perturb the performance of the 2d-MOT. After the tapered amplifier, we get a total of 350 mW power from the fiber, with approximately equal power in cooler and repumper light. Before mixing, part of the 2d-MOT cooler light is split off and coupled into a separate fiber for the 2d-MOT push beam, with an approximate power of 7 mW after the fiber. The different AOM paths are separated by polarizing beamsplitter cubes, shown in the schematic setup. These cubes keep unwanted back-reflections from entering into the 3d-MOT/molasses fiber and significantly contribute to the stability of the experiment.

The frequencies of the AOMs for 3d-MOT and molasses are adjusted during the experimental sequence to yield the laser frequencies shown in fig. 6.8. Special care is taken for the frequency adjustment of the D1 cooler and repumper. These lights must be in a Raman condition for the molasses stage and must remain so during a frequency sweep. If the frequency signal for the cooler and repumper AOM path are created independently, slight differences in electronic components may break that condition during the sweep. This is circumvented by using a reference frequency at half the fine-structure splitting of the two ground states. The frequency for the

[20] Acousto optic modulator: Gooch and Housego, AOM 3110-120

[21] Tunable bandpass, Semrock, TBP01-790/12

molasses repumper AOM is created as the difference between the frequency of the molasses cooler AOM and this reference frequency. Subtraction of the two signals can be achieved by standard electronic radio-frequency components (for details see [95]). For the double-pass configurations of an AOM, the frequency shift on the light is twice the frequency on the AOM. Thus, the frequency difference between cooler and repumper light is always exactly the hyperfine splitting of the ground state. This enforces the Raman condition, independent of the detuning from the atomic resonance.

6.10.2 Laser system for imaging

The imaging lights are created by two separate lasers that are offset-locked [96] onto the D2 master laser. The D2 reference light reuses the 0th order light of an acousto-optic modulator (AOM) path for the 2d-MOT (see fig. 6.17). The reference light is mixed with the light of the two imaging lasers, respectively, as is shown in fig. 6.18 and in full detail in appendix A.5. For each of the lasers, the mixed lights are coupled into a fiber connected to a fast photodiode.[22] The photodiode detects the beating signal caused by the frequency difference between laser and D2 reference light. On the electronic side, the beat signal is mixed again with the signal of a voltage-controlled oscillator (VCO). This results in a new beating signal at a lower frequency. The low frequency signal is used to create an error signal in an interferometric setup. For that purpose, the signal is split in two. One of the signals passes through a delay line before remixing both signals. The amplitude of the signal after the last mixing depends on the frequency of the beating signal and thus on the frequency difference of the laser and the D2 master laser. It is the input signal for a proportional-integral controller that adjusts the cavity length and thus the frequency of the lasers. With this setup, the imaging lasers are stabilized to a fixed frequency difference compared to the D2 master laser. The frequency difference can be adjusted via the VCO. For the detailed setup – including necessary frequency filters – see [59].

The laser light must be switched rapidly for absorption imaging since a typical imaging pulse only lasts $10\,\mu s$. It is way too fast for mechanical shutters. Instead, AOM[23] are used as fast switches and also for frequency adjustment for the lights at zero magnetic field. The setup of the AOM paths is shown in fig. 6.18 and in full detail in appendix A.4.

[22] Thorlabs: DET025AFC/M, 2GHz Fiber-Coupled Si-Detector 400-1100nm

[23] Acousto optic modulator: Gooch and Housego, AOM 3110-120

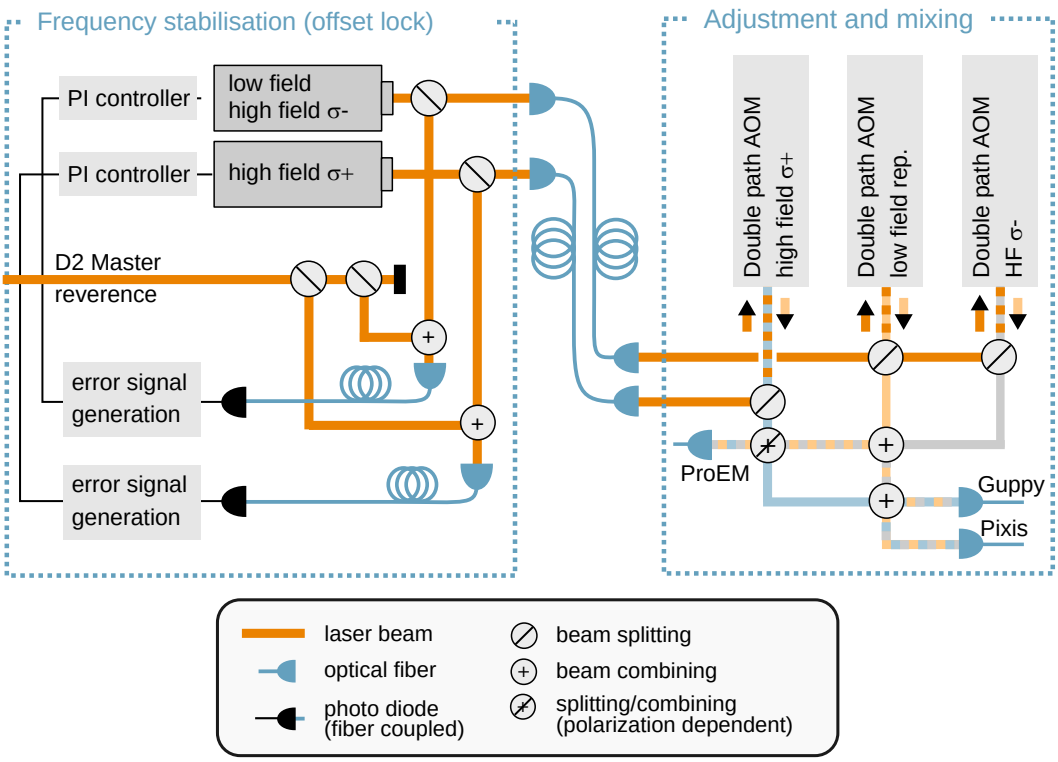

Figure 6.18: Laser system for imaging lights. For the imaging lights, two lasers are offset-locked on the D2-master laser. One laser produces the light for the imaging at zero magnetic field. In a different lock-setting, the same laser produces the $\sigma-$-light for imaging at high magnetic fields. The second laser creates the light for the $\sigma+$-light for imaging at high magnetic field. Switching of light and final frequency adjustment is done with acousto-optical modulators. The lights are mixed and coupled into the fibers for the three absorption imaging setups. All imaging setups can be switched between imaging at zero and at high magnetic field and the polarizations are adjusted to the respective requirements. The detailed setup including the polarization is shown in appendix A.4 and appendix A.5.

For imaging at low magnetic field, only one laser is needed. In the low-field configuration, it is locked to a small frequency offset to the D2 master of only 10 MHz (see [59] for details). Two AOM paths change the frequency of the light such that it is in resonance with the cooler and repumper transition, respectively.

At the magnetic fields close to the Feshbach resonance, the frequency difference between the two imaging lights is too large to be easily reached with AOMs. For example, at a magnetic field of 550 G, the σ^- light has a frequency difference to the D2 master of $\Delta f = -847$ MHz and the $\sigma+$ light of $\Delta f = +845$ MHz. Thus, for imaging at the high magnetic field, the two lights are created by the separate lasers. The frequencies of the offset lock together with the frequency shifts from the AOMs are chosen such that both lights are exactly on resonance at the respective field. For the σ^- light, one of the low-field imaging AOM paths is reused.

To be able to choose between high-field and low-field imaging in all three absorption imaging setups (see section 6.5), the lights are mixed and coupled into the three different optical fibers. In doing so, the polarization of the different lights needs to be taken into account. At the position of the atoms, the homogeneous magnetic field points upwards. The imaging beams for the Guppy and Pixis camera are in the horizontal plane. For this beam setup, both high-field lights need to be horizontal linear polarized. This polarization is an equal superposition of σ^+ and σ^- light. Thus, half of the light is in the necessary polarization which is the best possible fraction for horizontal beams.

For the main imaging with the ProEM camera, the light path is vertical. Optimal signal to noise is reached when the high-field imaging lights have the polarisation they are named after: σ^+ and σ^-. To achieve this, the lights are mixed with their polarisations at a 90° angle with respect to each other. This is possible by mixing with a polarizing beamsplitter. A single $\lambda/4$-plate then creates the desired circular polarization. The exact mixing setup together with the polarization adjustment after the fibers is shown in appendix A.5.

6.10.3 Laser system for attractive dipole traps

There is a total of five attractive dipole beams - the two reservoir beams, compressor and condenser beams, and the top beam - which all get their light from a 55 W laser at 1064 nm[24]. A schematic drawing of the setup is shown in fig. 6.19, and the detailed illustration of the optical setup is in appendix A.6.

The two reservoir beams carry up to 12 W of power each, too much to be carried in a single-mode optical fiber. Thus, the reservoir beams are free-space beams. The

[24]Coherent, Mephisto MOPA 55W

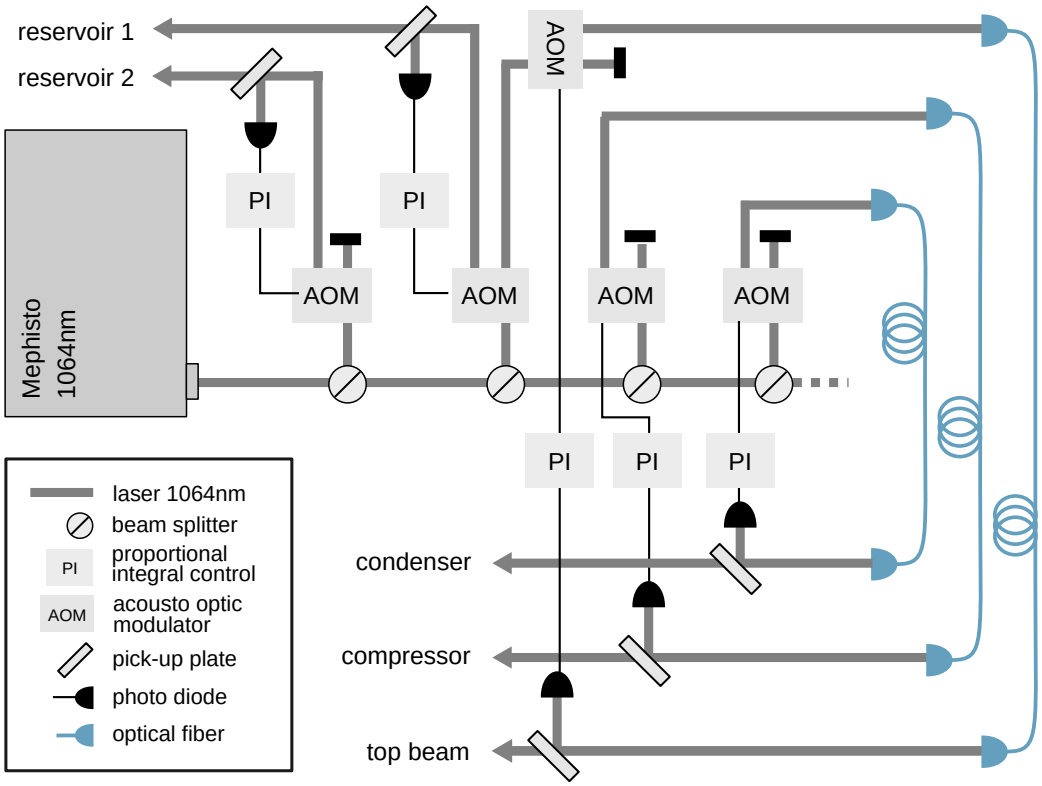

Figure 6.19: High power laser system for attractive dipole traps. A high-power laser provides up to 50 W of 1064 nm light. It is split into five separate dipole beams, which can be switched via acousto-optical modulators. The modulators also regulate the power within the beams. The two reservoir beams are free-space beams, since they carry up to 12 W power each. The remaining three beams have a maximum power of 2 W and are fiber-coupled.

other three beams are all fiber coupled[25] with a maximum power of 2 W after the fiber. The power of each beam is regulated by an AOM[26] (AOM). After the fiber output, pickup-plates reflect about 5% of the beam power onto a photodiode. The photodiode signal is the input for a proportional-integral control loop that actively stabilizes the power in the beam. By changing the set value of the loop, well-controlled power ramps are possible. Beams can be turned off entirely by a radio-frequency switch[27] that interrupts the frequency signal for the AOM. The frequencies of the AOMs are

[25] Schäfter-Kirchhoff, fiber: PMC-E-980-8.5-NA009-3-APC.EC-500-P, coupler: 60FC-4-M15-37
[26] Gooch and Housego: AOM 3080-199, 80 MHz, 1064 nm, Aperture 2.5 mm
[27] Mini Circuits: ZASWA-2-50DRA+

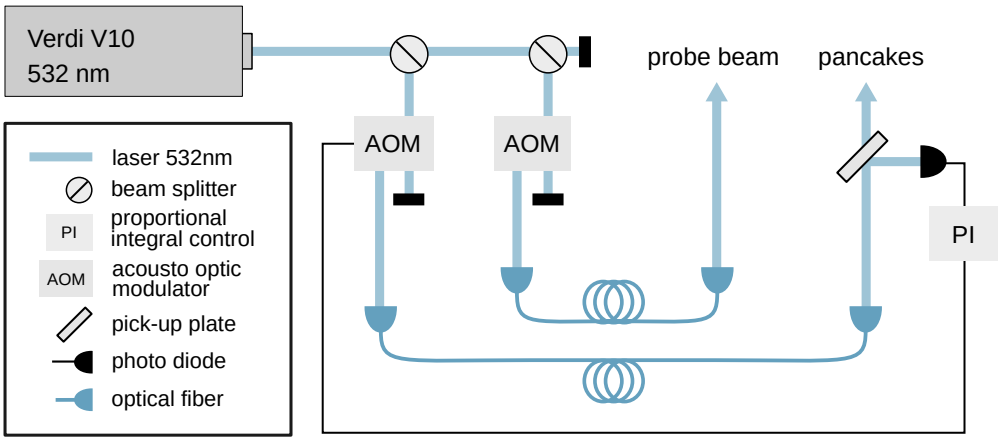

Figure 6.20: Laser system for repulsive dipole traps. Similar to the setup for attractive dipole beams, the laser light is split into the different beams, which can be switched on and off via an AOM. The beam for the pancake-interferometer is power-stabilized and carries up to 2 W. It is coupled into a photonic crystal fiber. The probe beam is not power-stabilized and only needs powers below 1 mW and is thus coupled into a conventional single-mode fiber.

all chosen differently to avoid interference effects between the separate dipole beams.

A final detail is that the top beam uses a zeroth AOM-order from one of the reservoir beams. This is possible since the top beam and the reservoir beam are never used simultaneously at full power.

6.10.4 Laser system for pancake traps and probe beam

The fourth laser system provides the light for the pancake interferometer and for the probe beam which are both repulsive dipole traps. A laser[28] at 532 nm creates a beam of up to 10 W of power which is split in two as illustrated schematically in fig. 6.20 and in full detail in appendix A.7. Both beams pass through AOMs[29] and the first diffraction order is coupled into a fiber. The AOMs are used as fast switches and, in the case of pancake beam, also for active stabilization of the beam power. The probe beam only needs powers around a few Milliwatt and a standard optical fiber can be used. However, for the pancake beam, we need up to 2 W of power after the fiber. For green-light, such high power cannot be carried in a standard single-mode fiber due to stimulated Brioullin scattering [97]. For high intensities, the

[28] Coherent: Verdi V10

[29] Goose and Housego: AOM 3080-1916, 80 MHz, 532nm, 4.0mm aperture (high-power beam)

light itself creates an optical lattice inside the fiber, which in turn back-reflects the light. This effect sets a limit to the maximal intensity inside the fiber. For green light, this maximal intensity is reached at much lower total output power than for light of longer wavelength. This is due to the mode-field diameter inside the single-mode fiber, which is much smaller for green light than for longer wavelengths. Thus, high intensities inside the fiber are already reached at lower output power. However, there exist fibers that can circumvent this limitation: photonic crystal fibers allow for much wider mode diameter and thus lower intensities and are still single-mode and polarization-maintaining. For the pancake beam, we combine a photonic crystal fiber with a special fiber end[30] that dissipates non-coupled light and thus reduces the risk of burning the input facet of the fiber.

[30]NKT Photonics: LMA-PM-10 and fiber ends SMA-905 and FC/APC. The fiber coupler and collimator are from Schäfter-Kirchhoff 60FC-SMA-T-23-A18-01 for the SMA-905 connector and 60FC-4-M10-01 to collimate the pancake beam.

Chapter 7

Mathematical description of curved spaces

With the experimental setup described in the previous chapter, we can now focus on the spacetimes we want to investigate and their realization in the condensate. This chapter concentrates on the theoretical description of spatial curvature in two dimensions. The following chapter then describes its experimental implementation.

While spatial curvature is one of the degrees of freedom in the FLRW metric of an expanding universe (see section 3.3), it can be discussed in a static setting. We will use this simplified setting to introduce different coordinate choices that will become important in the next chapter. As is the case for the FLRW metric, we demand spatial homogeneity and isotropy such that the curvature takes the same constant value at every point of the space. This leaves three different types of geometries: flat (zero curvature), spherical (positive curvature), and hyperbolic (negative curvature). Two-dimensional curved spaces can be visualized by embedding them in three-dimensional space. The two-dimensional spherical space is the surface of a sphere, the hyperbolic space is the surface of a hyperboloid, and flat space is a plane. However, embedding is not necessary. Instead, one can imagine observers that are entirely restricted to their dimensional worlds and determine the curvature by intrinsic measurements. In discussing curved spaces, switching between the intrinsic and embedded descriptions is often useful, depending on the phenomenon one wants to understand. This chapter starts with intrinsic observers that construct the metric of their respective curved spaces. Section 7.2 then introduces two coordinate changes, one that brings the metric to the form commonly used for the FLRW metric and a second coordinate transformation that will later be identified with laboratory coordinates in a Bose-Einstein condensate experiment. Section 7.3 describes and

parametrizes the curved spaces in their three-dimensional embedding, which is used to calculate distances in section 7.4. Using the distances, section 7.5 connects the intrinsic and embedded interpretations. Finally, section 7.6 discusses distortion due to projection effects for different observers.

7.1 Construction of a metric from intrinsic observations

Imagine three different observers living in a flat, spherically curved, and hyperbolically curved space, respectively. These observers only experience the two-dimensional surfaces and know nothing of the embedding. Still, they can characterize their space and determine its curvature. They could look at the tilt of a vector that is parallel transported along a closed curve or measure the sum of internal angles of a triangle. Here, we use a method that depends on the relation between radial and angular distance in a coordinate system with cylindrical symmetry.

We start the discussion with a definition of coordinate distance and physical/proper distance. For our purpose, a unit of physical distance is best defined as the product of the speed of light (or sound in an analog system) multiplied by a unit of time $d = c \cdot t$. The distance is connected to a specific choice of coordinates via the metric. A different choice of coordinates changes the form of the metric. However, the physical distances defined by the line element need to remain the same as they have a direct physical interpretation and reflect the geometry of the underlying space. To determine the curvature of their spaces, the three observers need to characterize this distance structure. To do so, they all choose a coordinate system as illustrated in fig. 7.1 with the following three criteria:

- The observer is at the origin of a spherically symmetric coordinate system with one radial and one angular coordinate.
- The spacing of the radial coordinate ξ is the same as the physical distance, i.e., the distance traveled by light in a unit of time.
- The angular coordinate φ runs from 0 to 2π.

In a second step, each observer measures the circumference of the circle at radius ξ. In flat space, the circumference is $2\pi\xi$, as we are used to from Euclidean geometry. However, this is not the case in the two curved spaces. In spherical space the circumference is lower $2\pi \sin\left(\sqrt{\kappa}\,\xi\right)/\sqrt{\kappa}$, in hyperbolic space it is larger $2\pi \sinh\left(\sqrt{-\kappa}\,\xi\right)/\sqrt{-\kappa}$. Here, κ is the value for the curvature, which is positive for

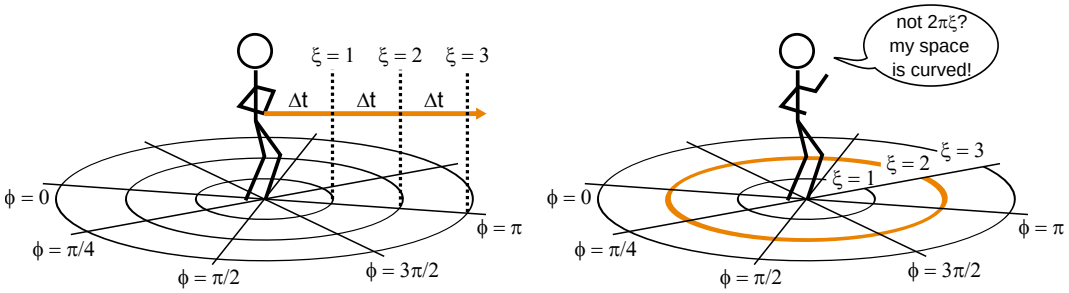

Figure 7.1: Curvature measurement and coordinate construction by an intrinsic observer. An observer restricted to a two-dimensional space can determine the curvature of the space by comparing the radius and circumference of a circle. The left-hand side shows how the observer defines a radial coordinate ξ via the travel distance of light (red arrow) in a time interval. In a second step, she measures the circumference of the circle of radius ξ (right-hand side). For a flat space, the circumference is $2\pi\xi$, smaller for a spherically curved one, and larger for a hyperbolic one.

spherically curved space, negative for the hyperbolic one, and zero for a flat space. This strategy will yield the same result independent of the observer's position for spaces with a homogeneous curvature. While the origin of the coordinate system seems to be a special point, it is arbitrarily chosen, and any point could be the origin. The observers can construct their respective metrics by taking the angular increments corresponding to the circumferences. For the described coordinates, they read

$$\mathrm{d}\vec{x}^2 = \mathrm{d}\xi^2 + \begin{cases} \frac{\sin^2\left(\sqrt{\kappa}\,\xi\right)}{\kappa}\,\mathrm{d}\varphi^2 & ,\kappa > 0 \text{ spherical} \\ \xi^2\,\mathrm{d}\varphi^2 & ,\kappa = 0 \text{ flat} \\ \frac{\sinh^2\left(\sqrt{-\kappa}\,\xi\right)}{-\kappa}\,\mathrm{d}\varphi^2 & ,\kappa < 0 \text{ hyperbolic} \end{cases} . \tag{7.1}$$

7.2 Two new coordinate systems

The metric constructed in the last section corresponds to a particular choice of coordinates, which is only one among many possible ones. In the context of cosmology, it is conventional to use *reduced-circumference polar coordinates* [43]. Here, a new radial coordinate u is redefined such that the influence of curvature shifts from the angular to the radial part of the metric. The new radial coordinate is related

to ξ by

$$u(\xi) = \begin{cases} \frac{\sin(\sqrt{\kappa}\xi)}{\sqrt{\kappa}} & \text{, spherical} \\ \xi & \text{, flat} \\ \frac{\sinh(\sqrt{-\kappa}\xi)}{\sqrt{-\kappa}} & \text{, hyperbolic} \end{cases} \quad \text{and} \quad \mathrm{d}u = \sqrt{1-\kappa u^2}\,\mathrm{d}\xi\,, \tag{7.2}$$

which brings the metric into the compact form

$$\mathrm{d}\vec{x}^2 = \frac{\mathrm{d}u^2}{1-\kappa u^2} + u^2\mathrm{d}\varphi^2\,, \quad \begin{cases} \kappa > 0 & \text{, spherical} \\ \kappa = 0 & \text{, flat} \\ \kappa < 0 & \text{, hyperbolic} \end{cases}. \tag{7.3}$$

For this choice of coordinates, the physical circumference of a circle is $2\pi u$. In the radial direction, the physical distance and coordinate distance are not the same anymore (see fig. 7.2 for illustration).

The third choice of coordinates maps both spherical and hyperbolic space onto a finite-sized disk of radius R and are thus be called *disk coordinates* or – anticipating results from the next chapter – *lab coordinates*. The radial coordinate $r \in [0, R)$ is defined as

$$u(r) = \begin{cases} \frac{r}{1+\frac{r^2}{R^2}} & \text{, spherical} \\ r & \text{, flat} \\ \frac{r}{1-\frac{r^2}{R^2}} & \text{, hyperbolic} \end{cases} \quad \text{with} \quad \frac{\mathrm{d}r^2}{\left(1 \mp \frac{r^2}{R^2}\right)^2} = \frac{\mathrm{d}u^2}{1 \pm 4\frac{u^2}{R^2}}\,. \tag{7.4}$$

The maximal radius R is related to the curvature by $\kappa = 4/R^2$ in the spherical case and $\kappa = -4/R^2$ for a hyperbolic space. The corresponding metric is

$$\mathrm{d}\vec{x}^2 = \begin{cases} \left(1 + \frac{r^2}{R^2}\right)^{-2}(\mathrm{d}r^2 + r^2\mathrm{d}\varphi^2) & \text{, spherical} \\ \mathrm{d}r^2 + r^2\mathrm{d}\varphi^2 & \text{, flat} \\ \left(1 - \frac{r^2}{R^2}\right)^{-2}(\mathrm{d}r^2 + r^2\mathrm{d}\varphi^2) & \text{, hyperbolic} \end{cases}. \tag{7.5}$$

Neither the radial coordinate distance nor the circumference of a circle agrees with physical distances in this choice of coordinates. To visualize the structure of these coordinates, the rightmost panel of fig. 7.2 shows concentric lines that have the same physical distance between them. These circles seem to be further apart with increasing coordinate distance for the spherical case. For the hyperbolic case, the lines come closer together as the radial coordinate r approaches the maximal radius R. At $r = R$, both the physical distance in radial direction and the circumference of the circles diverge. Thus, the infinitely extended two-dimensional hyperbolic space is mapped onto a finite-sized disk, known as the *Poincare disk*.

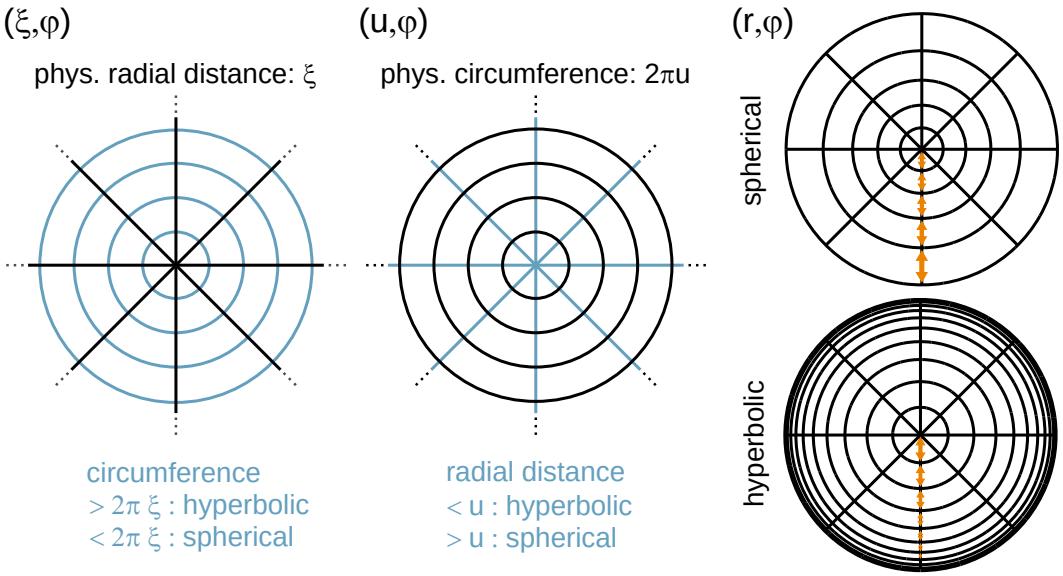

Figure 7.2: Comparison of the three coordinate systems for curved spaces. The left panel shows the coordinate system (ξ, φ) in which radial coordinate and physical distance are the same. The circumference of a circle at radius ξ depends on the curvature of the space. For the coordinates (u, φ) shown in the middle, this is reversed: The circumference of a circle is related to the coordinate by $2\pi u$, but the physical distance is not the same as the coordinate distance u. Neither the circumference nor the radial coordinate distance agrees with the physical distances for the *disk coordinates* (r, φ) shown on the right. Here, the concentric circles are drawn to have equal spacing in the physical distance, i.e., the orange arrows have the same physical length.

7.3 Embedding the curved spaces in three dimensions

For embedding, we consider a three-dimensional space with the three coordinate directions $\vec{x} = (x_1, x_2, x_3)^{\mathrm{T}}$. A two-dimensional positively curved space is the surface of a three-dimensional sphere of radius $\mathcal{R}$, which is described by the parameter equation

$$x_1^2 + x_2^2 + x_3^2 = \mathcal{R}^2 \ . \tag{7.6}$$

The curvature depends on the radius of the sphere $\kappa = 1/\mathcal{R}^2$; a small sphere has a large curvature and the other way around. Similarly, a two-dimensional hyperbolic surface with pseudo radius $\mathcal{R}$ is defined by

$$x_1^2 + x_2^2 - x_3^2 = -\mathcal{R}^2 \ , \tag{7.7}$$

which is a hyperboloid with the curvature $\kappa = -1/\mathcal{R}^2$. While the sphere's surface is finite in size, the hyperboloid is infinitely extended.

The parameter equation for the spherical surface is fulfilled by three-dimensional spherical coordinates with a fixed radius

$$\vec{x} = \mathcal{R} \cdot \begin{pmatrix} \cos\varphi \sin\theta \\ \sin\varphi \sin\theta \\ \cos\theta \end{pmatrix} , \tag{7.8}$$

with the conventional angles $\varphi \in [0, 2\pi)$ and $\theta \in [0, \pi)$ together with the Euclidean scalar product between two position vectors

$$\vec{x} \cdot \vec{y} = x_1 y_1 + x_2 y_2 + x_3 y_3 = |\vec{x}|\,|\vec{y}|\,\cos\alpha \ . \tag{7.9}$$

Here, we defined the direct angle α between the two position vectors.

For a hyperbolic space, a similar parametrization is possible by replacing the azimuthal angle θ by the pseudo-angle $\sigma \in [0, \infty)$ such that

$$\vec{x} = \mathcal{R} \cdot \begin{pmatrix} \cos\varphi \sinh\sigma \\ \sin\varphi \sinh\sigma \\ \cosh\sigma \end{pmatrix} , \tag{7.10}$$

together with the hyperbolic scalar product

$$\vec{x} \circ \vec{y} := x_1 y_1 + x_2 y_2 - x_3 y_3 = |\vec{x}| \cdot |\vec{y}| \cdot \cosh\eta \ , \tag{7.11}$$

where we defined the direct pseudo-angle η.By using $\sinh^2(\sigma) - \cosh^2(\sigma) = -1$, direct calculation shows that the combination of coordinates and scalar product indeed fulfills the parameter equation 7.7.

7.4 Calculating distances

The distance between two points is defined as the distance along a geodesic between those points. For a given metric, the geodesic can be found by solving the geodesic equation (see section 3.2). The distance is then found by integrating the line element along that path. For the highly symmetric spherical and hyperbolic spaces we consider here, the distances between two points can also be derived by using geometric arguments for the embedded spaces.

On the surface of a sphere, geodesics are the great circles, that is, circles with maximal radius. The distance between two points with coordinates (θ, φ) and (θ', φ')

is then given by the fragment of the great circle connecting them. The size of the fragment is determined by direct angle α between the two position vectors eq. (7.9). For the sphere with radius $\mathcal{R}$, the distance is

$$L_{\text{spherical}} = \mathcal{R} \cdot \alpha = \frac{1}{\sqrt{\kappa}} \cos^{-1}\left(\cos\theta\cos\theta' + \sin\theta\sin\theta'\cos(\varphi - \varphi')\right) , \quad (7.12)$$

where we used the relation between radius and curvature as well as $\cos\varphi\cos\varphi' + \sin\varphi\sin\varphi' = \cos(\varphi - \varphi')$ in the derivation of the direct angle.

In analogy, distances between two points on the hyperbolic surface with coordinates (σ, φ) and (σ', φ') are calculated from the direct pseudo-angle of the position vectors eq. (7.11). The distance is

$$L_{\text{hyperbolic}} = \mathcal{R} \cdot \eta = \frac{1}{\sqrt{-\kappa}} \cosh^{-1}\left(\cosh\sigma\cosh\sigma' - \sinh\sigma\sinh\sigma'\cos(\varphi - \varphi')\right) . \quad (7.13)$$

For completeness, we also state the distance in a flat space for the polar coordinates (u, φ). Since geodesic in flat space are straight lines, the distance follows directly from the Pythagorean theorem applied to polar coordinates, which gives

$$L_{\text{flat}} = [u^2 + u'^2 - 2uu'\cos(\varphi - \varphi')]^{1/2} . \quad (7.14)$$

7.5 Connecting intrinsic interpretation and embedding

Many aspects of curved spaces can be understood more quickly in the intrinsic interpretation, and others become clearer for the embedding. To switch between the two interpretations, this section establishes the connection between the disk coordinates and the embeddings. This is straightforward for the angle φ; it is the same in all coordinates and in the parametrization of the embedding. The radial coordinates and the parameters of the embedding are connected via the quantity all interpretations must agree on: the physical distances. In the intrinsic interpretation, the radial coordinate ξ is the physical distance in radial direction. In the embedding, the physical distance in radial direction is given by eq. (7.12) for $\theta' = 0$ in the spherical case and eq. (7.13) for $\sigma' = 0$ in the hyperbolic case

$$\xi = \begin{cases} \frac{\theta}{\sqrt{\kappa}} & \text{, spherical} \\ u & \text{, flat} \\ \frac{\sigma}{\sqrt{-\kappa}} & \text{, hyperbolic} \end{cases} . \quad (7.15)$$

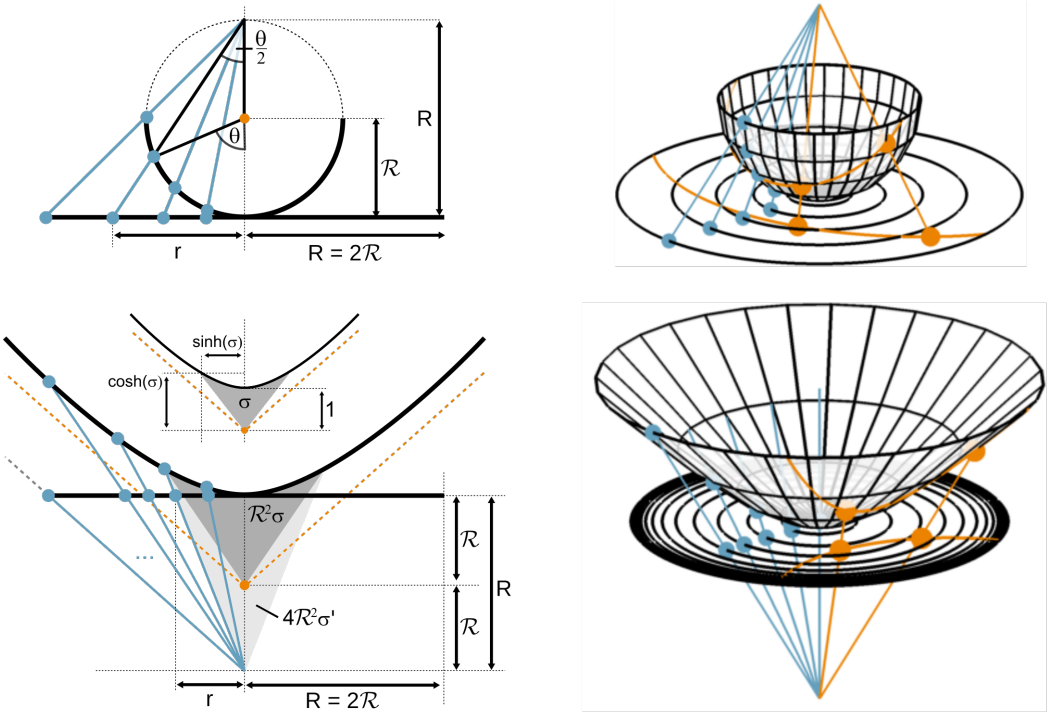

Figure 7.3: Projection between embedded spherical and hyperbolic space and disk coordinates. A half-sphere (upper row) and hyperboloid (lower row) with (pseudo-)radius $\mathcal{R}$ can be projected onto a disk with radius $R = 2\mathcal{R}$. The exact definitions and spacings of the projection are defined in the two-dimensional representation on the left-hand side. The right-hand side shows the same projection in three dimensions. The blue projection lines are the same on the left and the right. For the hyperbolic two-dimensional projection, the inset shows the definition of the hyperbolic sine and cosine, where the pseudo-angle σ is the size of the gray area. The orange dashed lines mark the boundary that the hyperboloid approaches towards infinity. The three-dimensional projections additionally contain a geodesic (orange line) connecting the two points marked by the orange dots. The geodesic is a great circle on the half-sphere and curves towards the center for the disk coordinates in spherical space. In hyperbolic space, it curves towards the edges and intersects the boundary of the disk at a right angle.

Together with eq. (7.2) and 7.4 this relates the lab coordinate r and the reduced circumference coordinate u to the angle and pseudo-angle

$$\theta = \sin^{-1}\left(\sqrt{-\kappa}u\right) = \sin^{-1}\left(2\,\frac{\frac{r}{R}}{1+\frac{r^2}{R^2}}\right) \quad \Leftrightarrow \quad \frac{r}{R} = \tan\frac{\theta}{2}\,, \tag{7.16}$$

$$\sigma = \sinh^{-1}\left(\sqrt{\kappa}u\right) = \sinh^{-1}\left(2\,\frac{\frac{r}{R}}{1-\frac{r^2}{R^2}}\right) \quad \Leftrightarrow \quad \frac{r}{R} = \tanh\frac{\sigma}{2}\,, \tag{7.17}$$

where, we used the curvature κ to connect the radius of the sphere/hyperboloid $\mathcal{R}$ with the parameter R in lab coordinates. The curvature is $4/R^2 = \kappa = 1/\mathcal{R}^2$ and hence $R = 2\mathcal{R}$.

Geometrically, this corresponds to the projections shown in fig. 7.3. The right-hand side of the figure shows the three-dimensional projection from the embedded curved spaces (spherical on top, hyperbolic on the bottom) onto the finite-sized disk of the disk coordinates. The left-hand side shows a cut of the projection, which illustrates the parameters of the projection.

7.6 Coordinate distortions in the projection

For all described spaces, the coordinate systems, as well as the embeddings, are centered around one specific point. It is important to keep in mind that this origin is an arbitrarily chosen point in a homogeneous space.

For the case of a hyperbolic space, this is illustrated in fig. 7.4. Here, two observers live in the same hyperbolically curved space. They both perform the procedure described in section 7.1 to construct a coordinate system with themselves at the origin. Both observers will perceive themselves at the center of a circular symmetric coordinate system. However, if the black observer in fig. 7.4 draws the blue coordinate system, it seems distorted. This is a projection effect which is illustrated for the Poincare disk at the top of the figure. The other way around, the blue observer perceives her own coordinates as symmetric and the black coordinates as distorted. An appropriate transformation allows to change between the frames of two observers. It is calculated via the distances derived above. In the following chapter, we perform such a frame change on experimental data to probe the geometry of analog curved space implemented in the quasi-two-dimensional Bose-Einstein condensate.

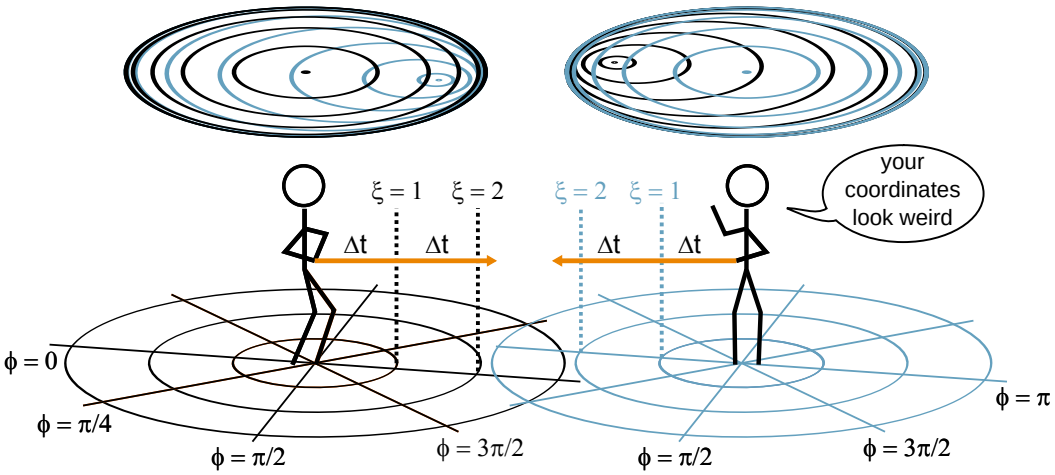

Figure 7.4: Two observers in a hyperbolic space If two observers are located at different points of a hyperbolic space, they can both set up a circular symmetric coordinate system, with themselves at the center. Both coordinate systems will be equivalent due to the homogeneity of the space. Both observers can transform to the coordinates of the Poincare disk. They both see themselves at the center of the disk. Caused by the projection, they perceive the coordinate system of the other observer as distorted.

CHAPTER 8

Implementation of spatial curvature in the two-dimensional BEC

A spatially curved analog space can be implemented in a two-dimensional Bose-Einstein condensate by shaping its density distribution. Based on [41], this chapter first derives the exact density profiles for a homogeneous space with spherical, flat, and hyperbolic curvature in section 8.1 and shows that a harmonically trapped condensate approximates a hyperbolic space. Section 8.2 presents measurements that probe the analog geometry of a harmonically trapped condensate using the propagation of wave packets. These results have been published in [42].

8.1 Density profiles for analog spatial curvature

For the implementation of homogeneous curved spaces in a two-dimensional Bose-Einstein condensate, the spatial dependence of the sound speed in the acoustic metric eq. (4.16) can be adjusted via the spatial dependence of density distribution $n_0(r)$ of the background condensate. The sound velocity structure defines both the geometry and the coordinate system for the analog spacetime. This is different from curved spaces in the context of general relativity, where the coordinate choice has no physical correspondence at all. This gives the freedom to select among the coordinate system introduced in the previous section and choose the one best suited for the analog system. In the real world, a Bose-Einstein condensate is always limited in size. Thus, the coordinates (r, φ) defined in (7.5) are an ideal choice since they parametrize a finite-sized disk. The line element of a homogeneous curved space in

the disk coordinates is

$$\mathrm{d}s^2 = -\mathrm{d}t^2 + \mathrm{d}\vec{x}\,, \quad \mathrm{d}\vec{x}^2 = \begin{cases} \left(1+\frac{r^2}{R^2}\right)^{-2}\left(\mathrm{d}r^2 + r^2\mathrm{d}\varphi^2\right) & \text{, spherical} \\ \mathrm{d}r^2 + r^2\mathrm{d}\varphi^2 & \text{, flat} \\ \left(1-\frac{r^2}{R^2}\right)^{-2}\left(\mathrm{d}r^2 + r^2\mathrm{d}\varphi^2\right) & \text{, hyperbolic} \end{cases} . \tag{8.1}$$

From the comparison with the acoustic metric of static, radially symmetric BEC eq. (4.16)

$$\mathrm{d}s^2 = -\mathrm{d}t^2 + \frac{1}{c_s^2(r,t)}\left(\mathrm{d}r^2 + r^2\mathrm{d}\varphi^2\right)\,, \tag{8.2}$$

one can directly identify the necessary sound speed structure

$$c_s(r,t) = \bar{c}_s(t)\begin{cases} 1+\frac{r^2}{R^2} & \text{, spherical} \\ 1 & \text{, flat} \\ 1-\frac{r^2}{R^2} & \text{, hyperbolic} \end{cases}, \tag{8.3}$$

with $\bar{c}_s(t) = c_s(r=0,t)$ the sound speed at the center of the condensate. For the moment, we demand a time-independent sound speed, corresponding to a static curved space. Since $c_s \propto \sqrt{n_0(r)}$ (see section 2.4), the homogeneous curved spaces can be realized with the density profiles of the condensate

$$n_0(r) = \bar{n}_0\begin{cases} \left(1+\frac{r^2}{R^2}\right)^2 & \text{, spherical} \\ 1 & \text{, flat} \\ \left(1-\frac{r^2}{R^2}\right)^2 & \text{, hyperbolic} \end{cases}, \tag{8.4}$$

which are illustrated in fig. 8.1. Experimentally, the density profiles are shaped by the potential of the trap that holds the condensate (see section 2.1). For dipole traps, the potential is proportional to the light intensities of far-detuned light (see section 5.7). Fine spatial control of the intensities can be achieved with a digital micromirror device (DMD) [98, 99]. However, the installation of a DMD needs a sophisticated optical setup and was not ready in time for this work. Much easier to realize is a harmonic trapping potential around the minimum of an attractive Gaussian beam. In such a trap, the density distribution of a BEC is well described by the parabolic Thomas-Fermi profile $n_{TF}(r)$ which approximates the ideal density profile for the hyperbolic geometry

$$n_0(r) = \bar{n}_0\left(1-\frac{r^2}{R^2}\right)^2 \approx \bar{n}_0\left(1-2\frac{r^2}{R^2}+O(4)\right) = n_{TF}(r) + O(4)\,. \tag{8.5}$$

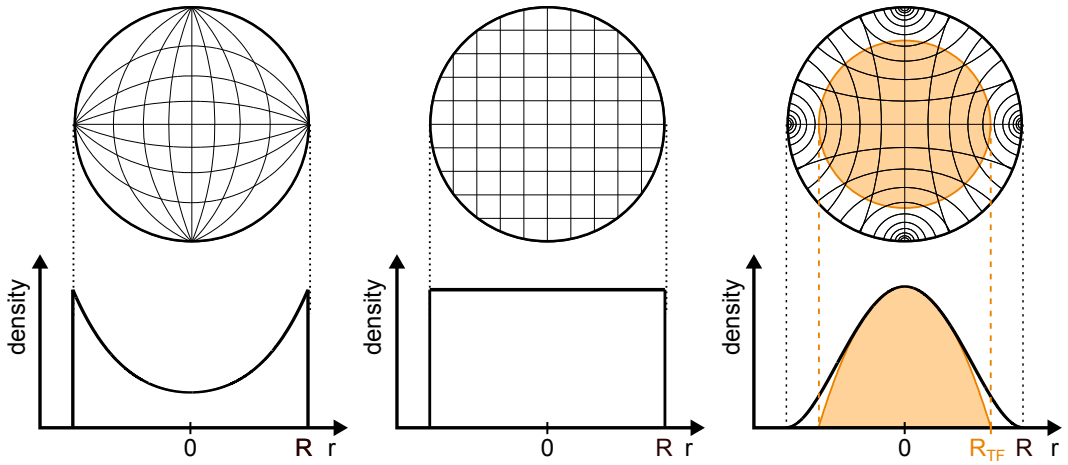

Figure 8.1: Density profiles for implementing spatially curved metrics. The density profiles that implement a spherically curved, flat, and hyperbolic space are shown from left to right. The disks represent the spherical condensate and show a square lattice – two orthogonal sets of parallel geodesics – in the analog space. The orange density profile is the parabolic density of a harmonically trapped condensate. It well approximates the hyperbolic profile around the center but drops faster towards the edges and reaches zero at $r_{TF} = R\sqrt{2}$.

The right panel of fig. 8.1 shows the parabolic density profile in orange in addition to the exact hyperbolic profile. The two profiles match around the center of the condensate; towards the edges, the density of the harmonically trapped condensate drops faster than the ideal profile. It reaches zero at the Thomas-Fermi radius $r_{TF} = R/\sqrt{2}$ which sets the curvature of the analog hyperbolic space to $\kappa = -\frac{2}{r_{TF}^2}$. Thus, deviations from a homogeneous hyperbolic space are only expected towards the edges. The following section tests this prediction with a quantitative analysis of wave packet dynamics in the harmonically trapped condensate.

8.2 Curvature measurement in a harmonically trapped BEC

To test the analog geometry of a harmonically trapped BEC experimentally, we perform measurements similar to the Gedanken-experiments in the previous section, in which intrinsic observers used the propagation of light to probe their surrounding space. In the analog spacetime, we instead use the propagation of phononic excitations. For that purpose, a blue-detuned repulsive laser beam (probe beam, see

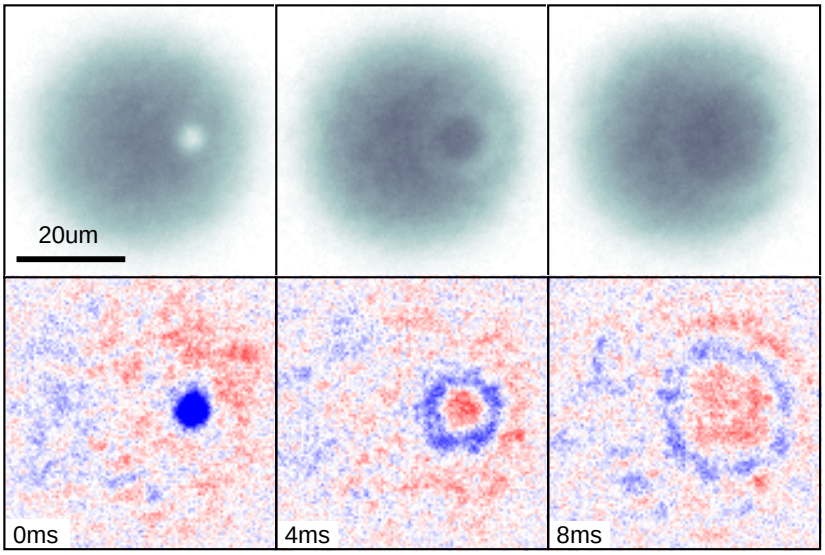

Figure 8.2: propagation of a phononic excitation in a harmonically trapped condensate The upper row shows average images of the perturbed condensate for the initial perturbation and two later times during the propagation of the under-density. The lower row shows the difference between the perturbed and unperturbed condensate for the same time steps; under densities are blue, overdensities red.

section 5.7) is focused onto a small patch of the condensate, which creates a local under-density. Once the laser is turned off, the under-density propagates radially outwards. Its movement is traced by recording the atom density by absorption imaging (see section 6.5) at different times during the propagation. For comparison, images of the unperturbed condensate are recorded for each time step. The condensate is formed by approximately 23.000 atoms held in a harmonic trap and magnetically levitated against gravity. By Feshbach-tuning, the s-wave scattering length is adjusted to $a_s = 100 a_B$ with a_B the Bohr radius. In gravity direction, the condensate is frozen to the ground state of a tight trap of $\omega_z = 2\pi \cdot 1.6\,\mathrm{kHz}$. In the remaining dimensions, the condensate is confined by a circular symmetric trap with frequency $\omega = 2\pi \cdot 12.4\,\mathrm{Hz}$ and has the Thomas-Fermi radius $r_{TF} = 24.5\,\mu\mathrm{m}$ (see section 6.9.2 for details of the trap). This initial perturbation is created at a distance of $0.4\,\mathrm{r_{TF}}$ from the center of the condensate. Around 100 realizations are recorded and averaged for each time step. Figure 8.2 shows examples for the propagation. The lower row of the figure shows the difference in mean density $\Delta\rho$ between the perturbed and unperturbed condensate.

To compare the propagation of the perturbation to the prediction to the structure of a hyperbolic space, we evaluate the propagation along a geodesic. The propagation

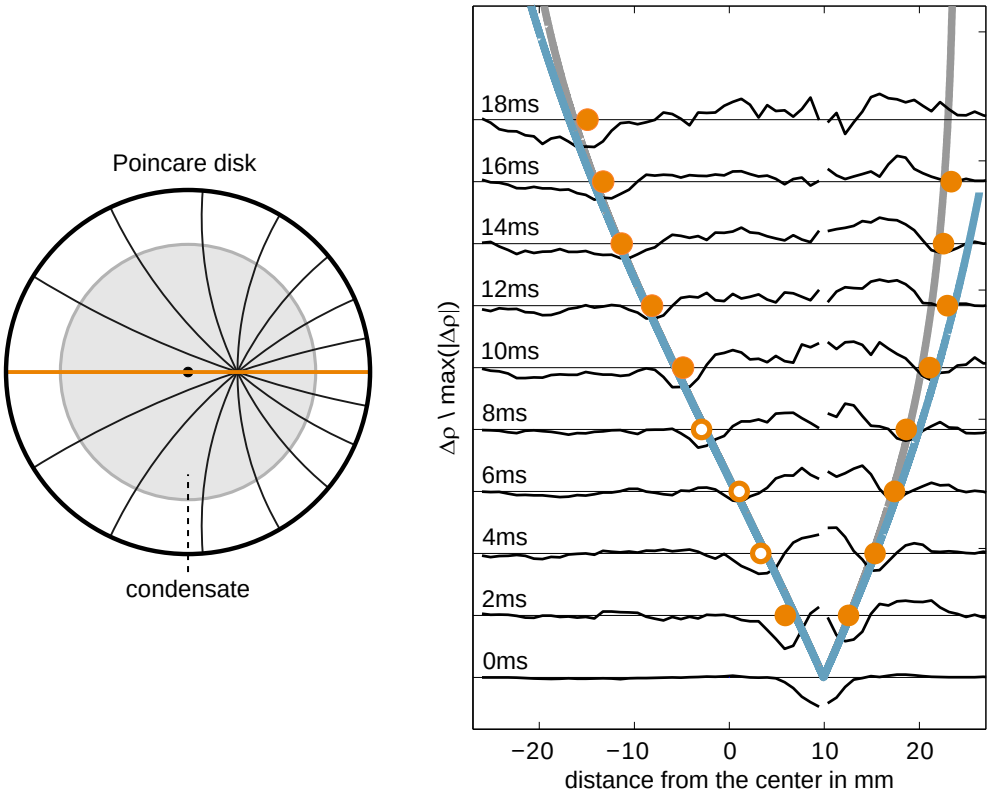

Figure 8.3: propagation of the phononic excitation along a straight geodesic. The left-hand side shows the geodesics in the Poincare disk emanating from the position of the initial under-density. Only the geodesic connecting this initial position with the center of the condensate appears straight in laboratory coordinates (orange line). The right-hand side shows the profile of the normalized density-difference along that line for different propagation times. The propagation of the under-density traces the sound cone of the analog space. The orange dots mark the position of the under-density extracted by a parabolic fit around the minimum. A linear fit to the three open symbols yields the speed of sound at the center of the condensate. The solid lines show the prediction for the propagation in the harmonically trapped condensate (grey) and in a homogeneous hyperbolic space (blue).

speed along the geodesic can be compared with the predictions of the metric. The left-hand side of fig. 8.3 shows geodesics emanating from the point of the initial perturbation. Here the grey shaded area marks the condensate's size within the expected Poincare disk. The geodesic connecting the perturbation with the center of the condensate (orange line) is the only geodesic that is a straight line in the lab coordinates. Along that line, the profiles of the density difference $\Delta\rho$ are obtained as an average over a 10° slice. These density profiles – normalized by the maximum depth of the perturbation – are shown on the right-hand side of fig. 8.3. The position of the minimum is determined by a parabolic fit around the minimum value of each profile and is marked by the orange symbol. The speed of sound at the center of the condensate is extracted by a linear fit to the three open symbols. It is $\bar{c}_s = 1.5\mu\mathrm{m/ms}$ in accordance with the speed of sound predicted from GPE simulations of the ground state.

The sound speed at the center of the condensate, together with the Thomas-Fermi radius and the position of the initial perturbation, predict the entire trajectory. The time at which a position in lab coordinates is reached is given by $t = d/\bar{c}_s$, where d is the analog distance between that position and the initial perturbation. For the hyperbolic space, the distance is given by eq. (7.13) in combination with eq. (7.17) and can be simplified using hyperbolic addition rules. For the simple case of the straight geodesic, the distance alternatively is found by direct integration of the line element of the acoustic metric. Since phonons propagate with the speed of sound, their trajectories are light-like with $\mathrm{d}s^2 = 0$. For the analog hyperbolic space, this yields

$$ds^2 = 0 = -\mathrm{d}t^2 + \frac{1}{\bar{c}_s^2}\left(1 - \frac{r^2}{R^2}\right)^{-2}\mathrm{d}r^2 \,, \tag{8.6}$$

where $r^2\mathrm{d}\varphi^2 = 0$ for this particular trajectory since $\mathrm{d}\varphi = 0$ at all points except the origin where $r = 0$. The above equation can be solved via separation of variables which yields

$$t(r) = \frac{\sqrt{2}r_{TF}}{\bar{c}_s}\left|\tanh^{-1}\left(\frac{r}{\sqrt{2}r_{TF}}\right) \mp \tanh^{-1}\left(\frac{r'}{\sqrt{2}r_{TF}}\right)\right| \,, \tag{8.7}$$

with r' the radial coordinate of the initial perturbation. The minus sign must be used if both points r and r' lie on the same side of the origin and the positive sign if they lie on opposite sides. The direct integration is also possible for the parabolic density distribution which yields

$$ds^2 = 0 = -\mathrm{d}t^2 + \frac{1}{\bar{c}_s^2}\left(1 - 2\frac{r^2}{R^2}\right)^{-1}\mathrm{d}r^2 \,, \tag{8.8}$$

and

$$\tilde{t}(r) = \frac{r_{TF}}{\bar{c}_s} \left| \sin^{-1}\left(\frac{r}{r_{TF}}\right) \mp \sin^{-1}\left(\frac{r'}{r_{TF}}\right) \right| . \tag{8.9}$$

The right-hand side of fig. 8.3 shows both the prediction for the parabolic condensate (grey line) and for the analog hyperbolic space (blue line). The experimental data agree well with the predicted propagation of the phononic perturbation. Only at a distance of $\approx 20\mu\text{m} = 0.8\, r_{TF}$, the measurement deviates from the hyperbolic prediction but still agrees with the harmonically trapped condensate.

To analyze the propagation of the perturbation in the entire two-dimensional space, we extract the 2d-shape of the under-density for each time step. For each angle from the initial perturbation, the radial position of the under-density is determined as an average over a 10° segment. Figure 8.4 shows these positions. As a guide to the eye, concentric circles around the perturbation are drawn (black lines). The rings of the under-density are distorted in comparison. This setting corresponds to the scenario described in section 7.6 where two observers compare their coordinate systems. In terms of observers, the image taken in laboratory coordinates corresponds to the coordinate system of an observer located at the center of the condensate, as is sketched in fig. 8.4. The propagating perturbation can be interpreted as a signal sent by a second observer located at the initial position of the perturbation. Using eq. (7.13) together with eq. (7.15), we can transform into the coordinate system (ξ, φ) of that observer, which is shown on the right-hand side of fig. 8.4. Here the propagation indeed becomes concentric. Since the transformation relies on the hyperbolic geometry, this confirms that the parabolic condensate implements the inner part of the Poincare disk and thus a hyperbolic space.

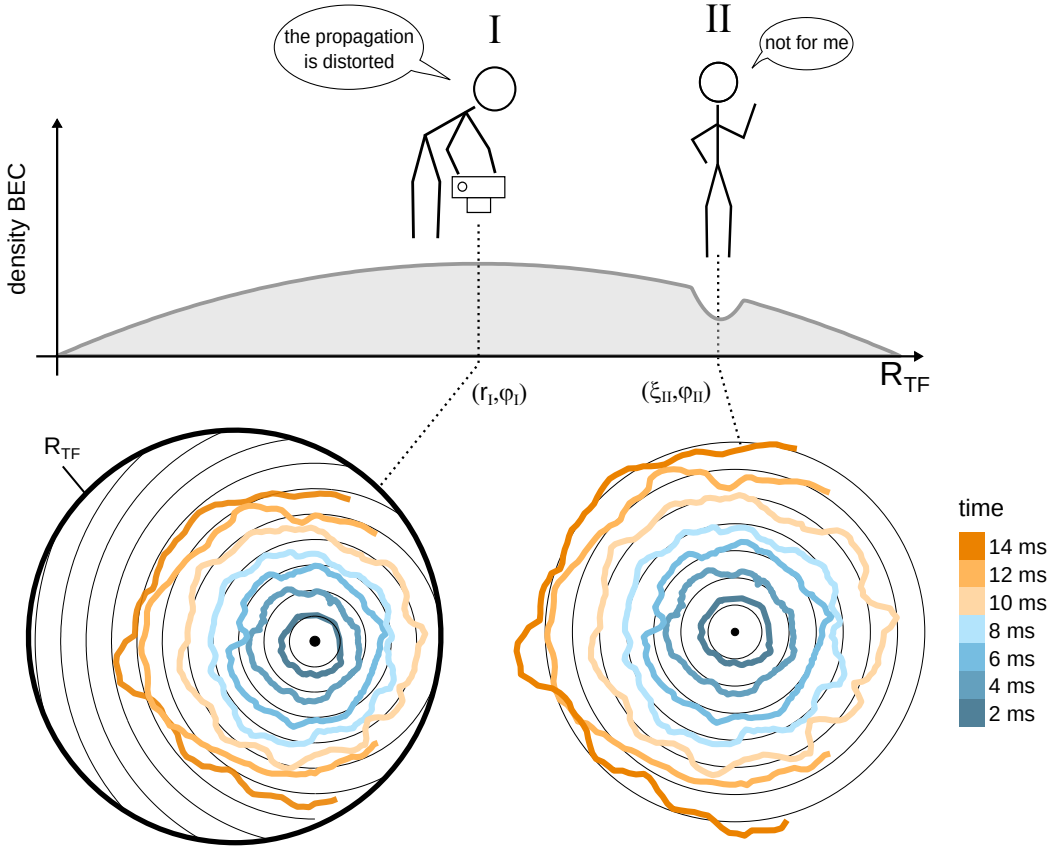

Figure 8.4: propagation of the phononic excitation for two observers. The lower-left side shows the position of the propagating under-density as the colored lines for a propagation times from 2 ms (dark blue) in 2 ms steps till 14 ms (dark orange). The outer bold black circle marks the Thomas-Fermi radius of the condensate. Around the initial position of the under-density (black dot), concentric circles are drawn in black as a guide to the eye. The colored lines do *not* coincide with these lines. This corresponds to the perceived coordinate distortion for an observer at the center of the condensate/Poincare disk. The right-hand side shows the same propagation transformed to the 'physical distances' of an observer located at the position of the initial under-density. Here, the colored lines fall onto the equally spaced concentric lines. This shows that the propagation is indeed circular symmetric in the coordinate frame of that observer and confirms the hyperbolic geometry of the analog space.

Chapter 9

Theory of cosmological particle production

The expansion of space in itself leads to the production of particles. Schrödinger first mentioned this phenomenon in his 1939 paper 'The proper vibrations of the universe' [100]. For him, the production of particles from the vacuum was still an alarming prospect. Today, this process is a likely candidate for creating the initial seeds for the cosmological large-scale structure. This chapter summarizes the derivation of correlation functions and excitation spectra for a scalar quantum field in an expanding spacetime. It summarized the calculations found in [41] and [101]. Here, we only consider the case of spatially flat spacetimes the modifications for curved spaces can be found in the above-mentioned papers.

9.1 A scalar field in expanding flat space

In a static space, a free, mass-less scalar field ϕ needs to fulfill the equation of motion

$$0 = \ddot{\phi} - \frac{\Delta}{a^2}\phi \,, \tag{9.1}$$

with $\ddot{\phi}$ the second time derivative of the field and $a \in R$ – for now – an arbitrary factor. In a spatially flat space, Δ is the Laplace operator. Solutions of this equation factorise into a spatial and a time-dependent part $\phi = \sum_j \mathcal{H}_j(\vec{x}) \cdot v_j(t)$. The spatial part needs to be an eigenfunction of the Laplace operator

$$\Delta\mathcal{H}_j = h_j \mathcal{H}_j \,, \tag{9.2}$$

with h_i the eigenvalue for the ith eigenfunction $\mathcal{H}_i$. In two-dimensional polar coordinates with radius u and angle φ, the Laplace operator takes the form

$$\Delta = \partial_u^2 + \tfrac{1}{u}\partial_u + \tfrac{1}{u^2}\partial_\varphi^2 \,. \tag{9.3}$$

Its eigenfunctions are Hankel functions (drum modes)

$$\mathcal{H}_{km}(u,\varphi) = e^{im\varphi} J_m(ku) \,, \tag{9.4}$$

with $J_m(ku)$ Bessel functions of the first kind and $m \in \mathbb{Z}$ and the eigenvalues are $h_k = -k^2$. Note that the eigenfunctions would be Fourier modes for a choice of Euclidean coordinates. The choice of polar coordinates and thus Hankel functions reflects the local isotropy of cosmological spacetimes. The same assumption is made later in this work in the analysis of experimental data.

The time-dependent part of the above ansatz needs to solve the equation

$$0 = \ddot{v}_k - \frac{h_k}{a^2} v_k \,. \tag{9.5}$$

This is fulfilled for the *mode functions* (see [101] for the proper choice of normalization)

$$v_k = \frac{\exp(-i\omega_k t)}{a\sqrt{2\hbar\omega_k}} \,, \tag{9.6}$$

with the eigenvalues

$$\omega_k = \frac{\sqrt{-h_k}}{a} = \frac{|k|}{a} \,. \tag{9.7}$$

Thus, in static space, the mode functions oscillate in time with their frequency proportional to the mode's momentum k. The field can then be written as a field operator

$$\phi(t,\vec{x}) = \int_{k,m} \left(\hat{a}_{km}\, \mathcal{H}_{km}(u,\varphi)\, v_k(t) + \hat{a}_{km}^\dagger\, \mathcal{H}_{km}^*(u,\varphi)\, v_k^*(t) \right) \,. \tag{9.8}$$

The operators $\hat{a}_i^\dagger$ and $\hat{a}_i$ are the creation and annihilation operator of the ith mode, which fulfill bosonic commutation relations, and integral is an abbreviation for $\int_{k,m} = \int \frac{\mathrm{d}k}{2\pi} k \sum_{m=-\infty}^{\infty}$. This is a decomposition of the field ϕ into pairs of modes with the same k but positive and negative frequencies. In addition, the annihilation operators define a vacuum state $|\Omega\rangle$ by

$$\hat{a}_j\, |\Omega\rangle = 0 \,. \tag{9.9}$$

9.2 Particle-pair production

In expanding space, the equation of motion for the field ϕ acquires an additional term (see [41] for details)

$$0 = 2a\dot{a}\dot{\phi} + a^2\ddot{\phi} - \Delta\phi \,, \tag{9.10}$$

where the time-dependent function $a(t)$ now has the meaning of the cosmological scale factor. Note that we again use the convention, that distances are measured in time and the scale factor has the unit of an inverse velocity. Compared to the equation of motion of a static spacetime eq. (9.1), a friction term appears. This friction is caused by the expansion of space itself and is thus called *Hubble friction* [47]. The spatial part of the solution stays the same as in the static case, but the mode functions $v_j(t)$ now need to fulfill the *mode equation*

$$\ddot{v}_k + 2\frac{\dot{a}}{a}\dot{v}_k - \frac{h_k}{a^2}v_k = 0 \,. \tag{9.11}$$

During the expansion, the v_j will not only oscillate but show a non-trivial evolution that will ultimately lead to particle creation.

For a quantitative treatment of this phenomenon we consider the scenario depicted in fig. 9.1. Here, the space starts in a static situation with scale factor a_i. Following [41] this will be called region I. This is followed by a phase of expansion or contraction during the time Δt (region II) described by $a(t)$ with $a(0) = a_i$ and $a(\Delta t) = a_f$. The expansion/contraction terminates in a second static situation (region III) with scale factor a_f. For the initial and final static region, we get the oscillating solutions with v_k, $\hat{a}_{km}$, $\hat{a}^\dagger_{km}$ and $\omega_{ki} = |k|/a_i$, the mode functions, annihilation operators, creation operators and angular frequencies in region I; and u_k, $\hat{b}_{km}$, $\hat{b}^\dagger_{km}$ and $\omega_{kf} = |k|/a_f$ the same objects in region III.

The annihilation operators in the region I and region III define two different vacua

$$\hat{a}_j\,|\Omega\rangle = 0\,, \qquad \hat{b}_j\,|\Psi\rangle = 0 \,. \tag{9.12}$$

Region I contains the vacuum state $|\Omega\rangle$ and the field operator ϕ. Both remain unchanged during the period of expansion/contraction. However, in region III, $|\Omega\rangle$ is no longer the vacuum state, and also the definitions of the mode functions and ladder operators have changed. In general, the mode functions v_k in region I and u_k in region III can be expressed as the superposition

$$u_k = \alpha_k v_k + \beta_k v_k^* \,, \qquad v_k = \alpha_k^* u_k - \beta_k u_k^* \,, \tag{9.13}$$

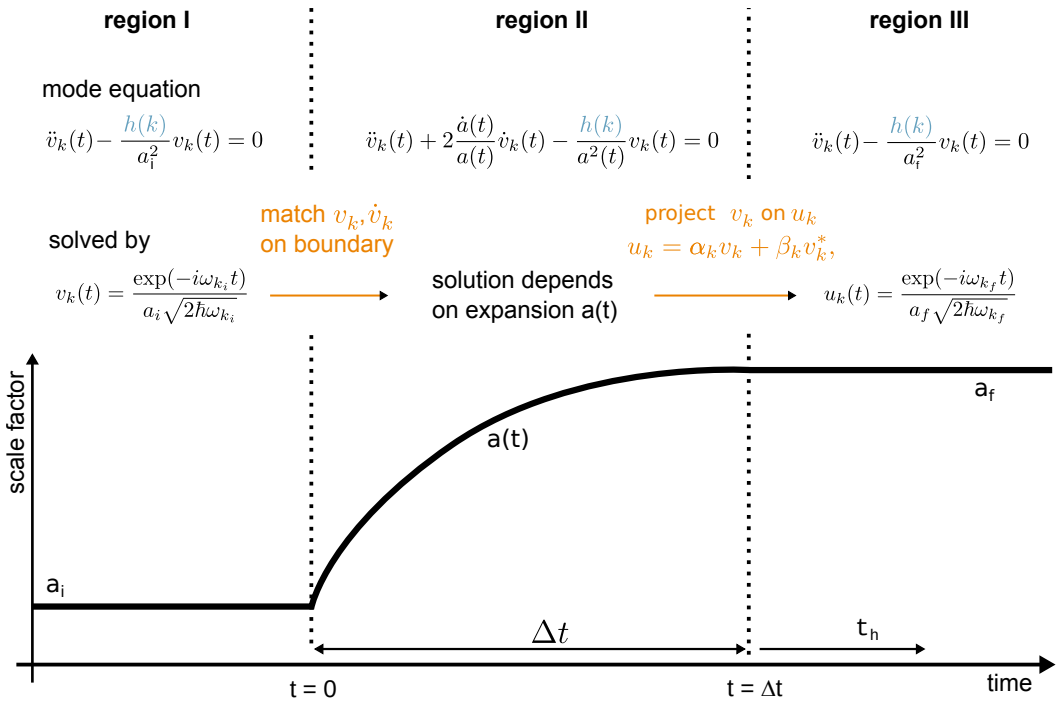

Figure 9.1: Expansion scenario for particle production and a schematic sketch of the calculation. The scenario for particle production starts and ends with a static space (region I and III). Between these regions, space expands/contracts during a period Δt. The important quantity for particle production is the evolution of the mode functions. In regions I and III, modes oscillate. In region II, the evolution is described by the mode equation and depends on the expansion itself. On the boundaries between regions, the mode functions and their derivatives must be matched. This connects mode functions in region I and region III, which in turn defines a Bogoliubov transformation between creation and annihilation operators in these regions.

with complex coefficients α_k and β_k. The field operator eq. (9.8) then is

$$\begin{aligned}\phi(t,\vec{x}) &= \int_{k,m} \left[(\alpha_k^* \hat{a}_{km} - \beta_k^* (-1)^m \hat{a}_{k,-m}^\dagger)\mathcal{H}_{km}\, u_k + (\alpha_k (-1)^m a_{k,-m}^\dagger - \beta_k \hat{a}_{km})\,\mathcal{H}_{km}^*\, u_k^*\right] \\ &\stackrel{!}{=} \int_{k,m} \left[\hat{b}_{km}\,\mathcal{H}_{km}\, u_k + \hat{b}_{km}^\dagger\,\mathcal{H}_{km}^*\, u_k^*\right] , \end{aligned} \tag{9.14}$$

where the property of the Bessel functions $J_{-m}(ku) = (-1)^m J_m(ku)$ was used. This defines a Bogoliubov transformation between the creation and annihilation operators in region I and region III

$$\hat{b}_{km} = \alpha_k^* \hat{a}_{km} - \beta_k^* (-1)^m \hat{a}_{k,-m}^\dagger , \qquad \hat{b}_{km}^\dagger = \alpha_k (-1)^m a_{k,-m}^\dagger - \beta_k \hat{a}_{km} . \tag{9.15}$$

This especially means that the original vacuum state $|\Omega\rangle$ is no longer empty

$$\hat{b}_{km}\,|\Omega\rangle = -\beta_k^*(-1)^m\,\hat{a}^\dagger_{k,-m}|\Omega\rangle \neq 0\ . \tag{9.16}$$

What remains is to determine the coefficients α_k and β_k, which depend on the expansion/ contraction of the spacetime in region II. To do so, the mode functions v_k must be 'transported' from region I, through the expanding region II to the boundary with region III. There they are projected onto the u_k (eq. (9.6), modified to region III) to determine the coefficients α_k and β_k. The evolution of v_k is described by eq. (9.6) in the static regions and eq. (9.11) during expansions. At the boundaries between regions, the value and derivative of v_k must be matched. Taking into account proper normalization as well as the correct commutation relations between ϕ and its canonical momentum (see [41] for details), the coefficients are given by the Wronskian

$$\begin{aligned}\alpha_k &= -i\,\mathrm{Wr}[u_k, v_k^*] = -i\,a_f^2\,\hbar\,[u_k\dot{v}_k^* - \dot{u}_k v_k^*]\ ,\\ \beta_k &= \ \ i\,\mathrm{Wr}[u_k, v_k] = \ \ i\,a_f^2\,\hbar\,[u_k\dot{v}_k - \dot{u}_k v_k]\ ,\end{aligned} \tag{9.17}$$

where v_k and v_k^* are evaluated in region II at the border to region III and the u_k and u_k^* in region III at the border to region II.

9.3 Correlations function and power spectrum

With the Bogoliubov transformation and its coefficients established, correlation functions of the field and its time derivative can be calculated for times t after the expansion/contraction (region III). Expressions for several correlation functions can be found in [101]. One correlation function is of particular interest for this work since it will be connected to observable quantities in a BEC in the following chapter. This is the statistical, connected, equal time, two-point correlation function of the time derivative of the field

$$\mathcal{G}_{\dot\phi\dot\phi}(L) = \left\langle \left\{\dot\phi(t,u,\varphi), \dot\phi(t,u',\varphi')\right\}\right\rangle_c\ . \tag{9.18}$$

Note, that the correlation function depends only on the the distance L between the two points (u,φ) and (us,φ'). This is due to the isotropy and homogeneity in an FLRW metric. Direct calculation relates the correlation function to the time-dependent power-spectrum $S_k(t)$

$$\mathcal{G}_{\dot\phi\dot\phi}(L) = \int_k \mathcal{F}(k,L)\frac{\sqrt{-h(k)}}{a_f^3}S_k(t)\ . \tag{9.19}$$

where, the integral abbreviates $\int_k = \int \frac{\mathrm{d}k}{2\pi} k$ and $\mathcal{F}(k, L) = J_0(kL)$ are Bessel-functions of the first kind. Thus, the above expressions are Bessel transformations between the spectrum and the correlation function. The spectrum itself has the form

$$S_k(t) = \tfrac{1}{2} + N_k + \Delta N_k(t)\,, \tag{9.20}$$

with

$$N_k = \langle \Omega \,|\, \hat{b}^\dagger_{km}\, \hat{b}_{km} \,|\, \Omega \rangle = |\beta_k|^2 \tag{9.21}$$

$$\Delta N_k = \langle \Omega \,|\, \hat{b}^\dagger_{km}\, \hat{b}^\dagger_{k,-m} \,|\, \Omega \rangle = \mathrm{Re}\left[\alpha_k \beta_k \exp(2i\omega_k t)\right]\ . \tag{9.22}$$

where $t \geq \Delta t$ is the time passed since the beginning of the expansion (beginning of region II). The spectrum is decomposed into the time-independent populations N_k and the oscillating coherences $\Delta N_k(t)$. Splitting the oscillation into amplitude and phase, it can be written as

$$\Delta N_k = |\alpha_k \beta_k| \cos(\Theta_k + 2\omega_k t_h)\,, \tag{9.23}$$

with $t_h \geq 0$ the time after the end of the expansion/contraction and Θ_k the initial phase

$$\Theta_k = \mathrm{Arg}(\alpha_k \beta_k) + 2\omega_k\, \Delta t\ . \tag{9.24}$$

If the particle production does not start from a vacuum but from a thermal state, the particle-pair production is enhanced by the thermal fluctuations [41]. The spectrum after the ramp then is modified to

$$S_k(t) = (1 + 2N_k^{in}) \left(\frac{1}{2} + N_k + \Delta N_k(t) \right)\,, \tag{9.25}$$

The initial fluctuations have the thermal spectrum

$$N_k^{in}(T) = \frac{1}{\exp(\hbar\omega_{k_i}/k_B T) - 1}\,, \tag{9.26}$$

and N_k and ΔN_k stil given by eq. (9.21) and eq. (9.23).

For particle-pair production in curved spaces, the calculations must be modified. These modifications are described in [41] and [101].

CHAPTER 10

Expanding spacetime in a BEC

The process of cosmological particle pair production is a general feature of a scalar field in an expanding spacetime and can be simulated in an analog expanding spacetime. Based on the works of our collaboration [41, 42], this chapter is dedicated to the implementation of such an expanding space and the experimental observation of particle-pair creation. It starts with the general idea for achieving an analog expanding space in a BEC in section 10.1. Sections 10.2, 10.3, 10.4 describe different details of the implementation, namely power-law expansion scenarios, the calibration for ensuring a static density distribution, and the choice of exact experimental parameters using the adiabaticity criterion. Section 10.5 shows examples for density distributions after the ramp, which show enhanced fluctuations. It also identifies a proper observable and presents correlation functions of that observable. Additional information is extracted from the time evolution of the correlation functions in section 10.6 and their power spectra in section 10.7. The latter reveals characteristic features in the particle-pair production for different expansion scenarios. Finally, section 10.8 establishes a connection between the adiabaticity criterion and an analog Hubble horizon and discusses a possible connection to the observed feature.

10.1 Implementation in the BEC

To realize an expanding spacetime in a two-dimensional, radially symmetric Bose-Einstein condensate (BEC), its acoustic metric eq. (4.16) needs to take the form of an FLRW metric eq. (3.10) in two dimensions. For a BEC with stationary

density distribution, this yields

$$\mathrm{d}s^2 = -\mathrm{d}t^2 + \frac{1}{c_s^2(r,t)}\left(\mathrm{d}r^2 + r^2\mathrm{d}\varphi^2\right) \stackrel{!}{=} -\mathrm{d}t^2 + a(t)^2\left(\frac{\mathrm{d}u^2}{1-\kappa u^2} + u^2\mathrm{d}\varphi^2\right) , \quad (10.1)$$

with the cosmological scale factor $a(t)$, the curvature κ, the speed of sound $c_s(t,r)$ and polar coordinates (r,φ) and (u,φ), respectively. The right hand side of the equation is not exactly the FLRW metric, but is connected to it by a trivial conformal transformation with a constant factor $1/c^2$. In this form, the scale factor $a(t)$ has the units of an inverse velocity and distances are measured in units of time. The sound speed depends on the atomic mass, density distribution of the background $n_0(r)$ and the 2d-coupling $\lambda(t)$ by $c_s^2(t,r) = \lambda(t)\, n_0(r)/m$. Chapter 7 and chapter 8 already established the connection between the lab coordinates (r,φ) and the reduced circumference coordinates (u,φ) in eq. (7.4) and identified the density profiles $n_0(r)$ that implement a spherical, flat and hyperbolic space in eq. (8.4). Using $\mathrm{d}\vec{x}^2(\kappa)$ as an abbreviation for the spatial part of the metric in the different curvatures, the acoustic metric is

$$\mathrm{d}s^2 = -\mathrm{d}t^2 + \frac{1}{\bar{c}_s^2(t)}\mathrm{d}\vec{x}^2(\kappa) , \quad (10.2)$$

with $\bar{c}_s(t)$ the speed of sound at the center of the condensate. This connects the scale factor in the analog metric to the sound speed in the condensate

$$a(t) = \frac{1}{\bar{c}_s(t)} = \sqrt{\frac{m\bar{n}_0}{\lambda(t)}} = \left(\frac{m^3\bar{n}_0^2}{8\pi\omega_z\hbar^3}\right)^{1/4} a_s(t)^{-1/2} , \quad (10.3)$$

where $\bar{n}_0$ is the density in the trap's center, and $\lambda(t)$ is the time-dependent 2d-coupling. The coupling, in turn, is proportional to the s-wave scattering length $a_s(t)$ (see eq. (2.7)). Equation (10.2) and eq. (10.3) imply that the expansion of space can be implemented by a global decrease in the speed of sound via the s-wave scattering length. This is illustrated in fig. 10.1. The left-hand side shows the expansion of space as it is often depicted in the cosmological context. The distance between the two orange points increases over time, proportional to the scale factor a. The distance increase is indicated by the appearance of additional concentric rings, which indicate proper distances from the central point. This proper distance is defined as the distance that light – or sound in the analog model – can travel in a fixed time step (see chapter 7 for comparison). The right-hand side shows the same scenario in the interpretation of the analog model. The two orange points remain at the same coordinate distance, corresponding to the condensate's static background density.

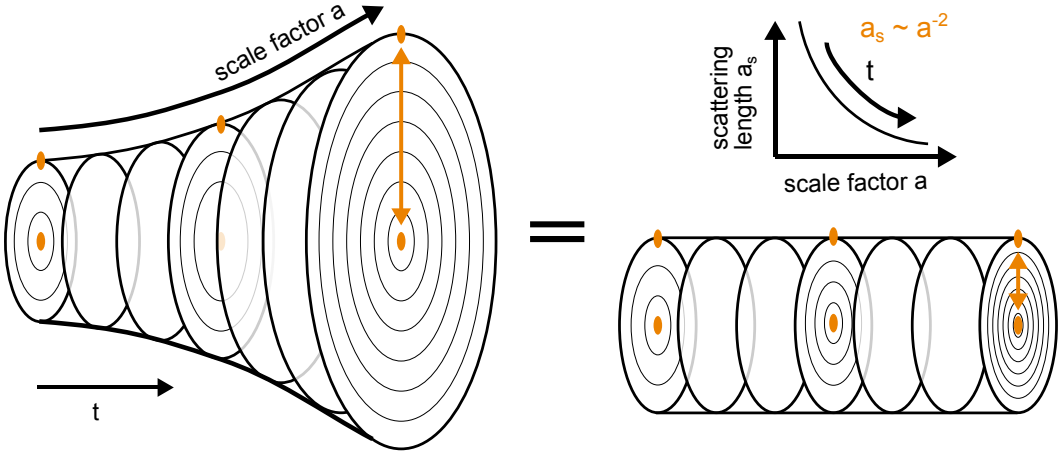

Figure 10.1: Analog expansion of space. Expansion of space can be understood as the increase of distance between any two points. The left-hand side shows this for the two orange points. Their distance increases proportionally to the scale factor a. The concentric equidistant lines serve as a ruler for the proper distances from the central point. Their spacing is defined by the distance that light (or sound) travels in a fixed time. The same expansion scenario is depicted on the right-hand side. Here the coordinate distance between the points stays the same, but the speed of light (or sound) decreases. This leads to a closer spacing of the concentric circles, a 'shrinking of the ruler.' For the analog spacetime of a BEC, the speed of sound is decreased with the s-wave scattering length, as indicated by the inset.

However, the scattering length and thus the speed of sound is decreased, as indicated by the inset and the concentric rings marking proper distance move closer together. Over time, more and more rings fit between the two points, indicating the increase in proper distance. The increase in proper distance is, by definition, the expansion of space.

10.2 Power law expansion

For typical expansion scenarios of an FLRW universe, the scale factor evolves with a power-law $a(t) \propto t^{\gamma}$, which is implemented with the s-wave scattering length $a_s(t) \propto t^{-2\gamma}$. For an expansion of duration Δt, starting from the initial scale factor a_i and scattering length $a_{s,i}$ and ending at the final scale factor a_f and scattering length

$a_{s,f}$ the power law ramps are

$$a(t) = a_i \left[1 - \left(1 - \left(\frac{a_f}{a_i}\right)^{\frac{1}{\gamma}}\right)\frac{t}{\Delta t}\right]^{\gamma} \quad \Leftrightarrow \quad a_s(t) = a_{s,i}\left[1 - \left(1 - \left(\frac{a_{s,f}}{a_{s,i}}\right)^{-\frac{1}{2\gamma}}\right)\frac{t}{\Delta t}\right]^{-2\gamma}. \tag{10.4}$$

The scattering length is controlled via the magnetic field at a Feshbach-resonance. To calculate the necessary magnetic field, the shape of the resonance must be taken into account (see section 5.4 for details). The required magnetic field is

$$B(t) = B_0 + \Delta\left(1 - \frac{a_s(t)}{a_{s,bg}}\right)^{-1}, \tag{10.5}$$

with B_0 and Δ the position and width of the resonance and $a_{s,bg}$ the background scattering length. For different values of γ, different expansion scenarios can be implemented. Depending on the deceleration parameter $q = -\ddot{a}a/\dot{a}^2$ (see section 3.4), accelerated and decelerated expansions are possible. In this work, we consider the three different cases

- uniform expansion with $\gamma = 1$ and $q = 0$,
- decelerated expansion with $\gamma = 1/2$ and $q = 1$,
- accelerated expansion with $\gamma = 3/2$ and $q = -1/3$.

10.3 Calibration for a static density distribution

As previously described, the density distribution of the condensate must remain static during and after the ramps of the scattering length. Experimentally, the density must be actively controlled since a condensate in a harmonic trap collapses during a decrease of the scattering length. Lowering the trap frequency counters this effect and keeps the density distribution static.

For that purpose, we calibrate the size of the condensate against the scattering length and the intensity in the trapping beam. Figure 10.2 shows the Thomas-Fermi radius of the cloud for different intensities and scattering lengths. The orange lines show cuts of a fit function that describes all data points simultaneously. The inverted fit represents the necessary change of the trapping beams' intensity during a change of the scattering length. It is implemented as a feed-forward that ensures a constant Thomas-Fermi radius during the different sweeps.

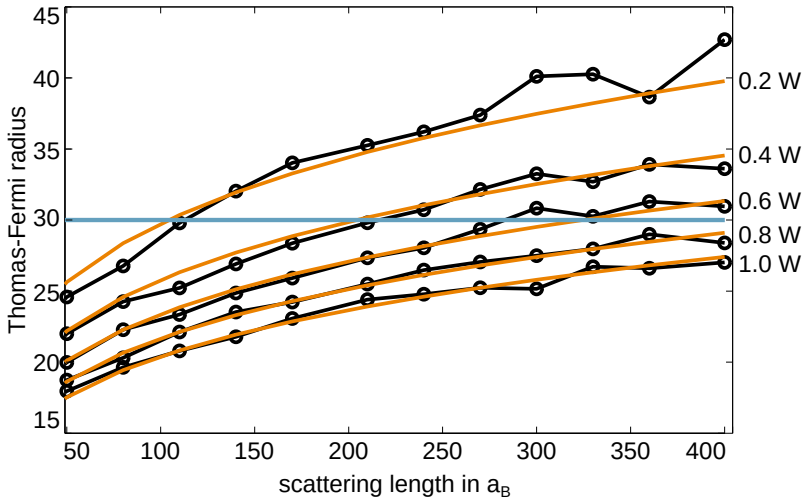

Figure 10.2: Calibration for a static density profile. The size (Thomas-Fermi radius) of the condensate is measured for different scattering lengths and intensities I of the trapping beam. A model is fitted to all data points simultaneously. For the given intensities the corresponding fit curves are plotted in orange. The blue line marks the condensate's size in the experimental runs. To keep the size constant during a ramp of the scattering length, the intensity of the trapping beam is adjusted using the inverse of the fit-function.

10.4 Choosing experimental parameters

For the power-law ramps described in the previous sections, four free parameters remain, the initial scattering length $a_{s,i}$, the final scattering length $a_{s,f}$, the duration of the ramp Δt, and the initial frequency of the harmonic trap confining the atoms. In choosing appropriate parameters, several fundamental and technical boundaries must be taken into account. First of all, the size of the atomic cloud sets an upper limit for the observable wavelength of perturbations which defines a minimal k-mode. [1] Here we define $k_{\min} = 2\pi/(2\,r_{TF})$ with r_{TF} the Thomas-Fermi radius of the condensate. A maximal resolvable k-mode is given by the camera's imaging resolution of $\sim 0.8\mu m$ and pixel size of $0.455\,\mu$m. The imaging resolution is the stronger constraint and leads to $k_{\max} \sim 4\,\mu\text{m}^{-1}$. A much tighter bound on the maximal momentum mode is set by the breakdown of the acoustic regime in the Bogoliubov dispersion relation. To be in the acoustic regime is an important assumption in the derivation of the

[1] For a hyperbolic space projected on the Poincare disk, space is infinite, and modes with arbitrarily large wavelength should be possible. Even though the condensate approximates a Poincare disk, the assumptions made in the derivation of the acoustic metric break down towards the edges of the condensate.

acoustic metric and the analogy between spacetime and condensate breaks down outside this regime. We estimate the upper limit of the acoustic regime by demanding the energy of a mode to be smaller than the chemical potential (see eq. (2.16) for comparison), which leads to

$$k_{ac}(t) < m\, c_s(t)/\hbar \ . \tag{10.6}$$

An additional requirement concerns the duration of the power-law ramps. If the change in scattering length is too slow, modes will not be populated. This principle is formulated in the adiabatic theorem [102, 103]. It states that a quantum mechanical system remains in its current eigenstate if changes are slow compared to the intrinsic time scale of the system. For the case Bogoliubov modes, the latter is determined by the system's energy $\hbar/E$, and the time scale of the change is the inverse relative energy change $E/\dot{E}$. Thus, a mode of energy E can only be excited if the time scale of its energy change is small compared to its intrinsic time scale

$$\frac{\hbar}{E} > \frac{E}{|\dot{E}|} \quad \Leftrightarrow \quad \frac{|\dot{E}|}{E^2}\hbar > 1 \ . \tag{10.7}$$

Modes within the linear part of the Bogoliubov energy have the energy and energy change in the experimental setting

$$E = \hbar c_s|k| = \hbar\sqrt{\frac{\lambda(t)\, n(x)}{m}}|k| \, ; \qquad \dot{E} = \frac{\hbar}{2}\sqrt{\frac{n(x)}{\lambda(t)\, m}}\, \dot{\lambda}(t)\, |k| \ , \tag{10.8}$$

with $\lambda(t)$ the 2d-coupling proportional to the scattering length $a_s(t)$. Thus, a mode can be populated if

$$|k_{\text{crit}}| < \left|\frac{1}{2c_s(x,t)}\frac{\dot{a}_s(t)}{a_s(t)}\right| \ . \tag{10.9}$$

For the three power-law ramps from the previous section with $\gamma \in [1/2, 1, 3/2]$, the criterion yields

$$\gamma = \tfrac{1}{2}: \quad |k_{\text{crit}}| < \left|\frac{1}{2\,\Delta t\, c_{s,i}(r)}\left(1 - \tfrac{a_{s,i}}{a_{s,f}}\right)\left[1 - \left(1 - \tfrac{a_{s,i}}{a_{s,f}}\right)\frac{t}{\Delta t}\right]^{-\frac{1}{2}}\right| \ , \tag{10.10}$$

$$\gamma = 1: \quad |k_{\text{crit}}| < \left|\frac{1}{\Delta t\, c_{s,i}(r)}\left(1 - \sqrt{\tfrac{a_{s,i}}{a_{s,f}}}\right)\right| \ , \tag{10.11}$$

$$\gamma = \tfrac{3}{2}: \quad |k_{\text{crit}}| < \left|\frac{3}{2T\, c_{s,i}(r)}\left(1 - \left(\tfrac{a_{s,i}}{a_{s,f}}\right)^{\frac{1}{3}}\right)\left[1 - \left(1 - \left(\tfrac{a_{s,i}}{a_{s,f}}\right)^{\frac{1}{3}}\right)\frac{t}{\Delta t}\right]^{\frac{1}{2}}\right| \ , \tag{10.12}$$

with $a_{s,i}$ and $a_{s,f}$ the scattering length at the beginning and end of the ramp and $c_{s,i}(r)$ the initial sound speed before the ramp. The sound speed depends on the radial distance from the center r; it is maximal at the center of the trap $\bar{c}_{s,i}$ and decreases due to the parabolic density profile of the condensate as

$$c_{s,i}(r) = \bar{c}_{s,i} \sqrt{1 - \left(\frac{r}{r_{TF}}\right)^2} \,. \tag{10.13}$$

Figure 10.3 shows all these criteria for a condensate of 23, 000 atoms, with a tight trap in gravity direction with $\omega_z = 1.6\,\mathrm{kHz}$ and radial trapping of 23.2 Hz. At an initial scattering length of $400\,a_B$ this results in a Thomas-Fermi radius of $30\,\mu$m and a speed of sound of $\bar{c}_{s,i} = 3.6\,\mu\mathrm{m/ms}$ at the center of the trap. The figure shows the critical momentum mode k_{crit} for ramps with initial scattering length of $400\,a_B$ and final scattering length $50\,a_B$ for the three power-law exponents $\gamma = [0.5, 1, 1.5]$ and for two ramp durations $\Delta t = [1.5\,\mathrm{ms}, 3.0\,\mathrm{ms}]$. The critical mode is evaluated at the center of the condensate and at distances of $0.5\,r_{TF}$ and $0.7\,r_{TF}$. Additionally, the figure contains the limits from the system size k_{min} as well as the breakdown of the acoustic regime at the three positions in the condensate. The grey color marks the 'forbidden' areas. The white area corresponds to modes that are phononic but adiabatic. These modes cannot be excited by the ramp. Finally, the colored areas are the modes that become non-adiabatic and can hence be excited by the ramp. The experimental parameters were chosen such that the excitable modes are larger than k_{min} but still within the acoustic regime. In the analysis of the experimental data in the following section, only the area up to $0.5\,r_{TF}$ will be considered. The figure also shows a clear difference in the time evolution of the critical mode for the three different ramp types. This will become important in section 10.8.

A final limitation is technical: the change of the scattering length is experimentally implemented by a rapid magnetic field change. The inductivity of the magnetic coils will counteract the change. Special care was taken in the construction of the coils to allow for these rapid changes (see [86] for details). To check the quality of the ramps, the current in the coils was measured during the six different ramps described above (using the current transducer in the control circuit of the coils). From the current, the magnetic field and scattering length are calculated and are shown in fig. 10.4 for single ramp-realizations together with their residual to the optimal ramp. Systematic deviations from the optimal ramp shape are visible in the data. For the fast ramp with $\Delta t = 1.5\,\mathrm{ms}$ deviations around 0.8 G appear at the beginning of the ramp. Due to the non-linear relation between the magnetic field and the scattering length in the vicinity of a Feshbach resonance, deviations in the magnetic field influence the scattering length primarily at the beginning of the ramp.

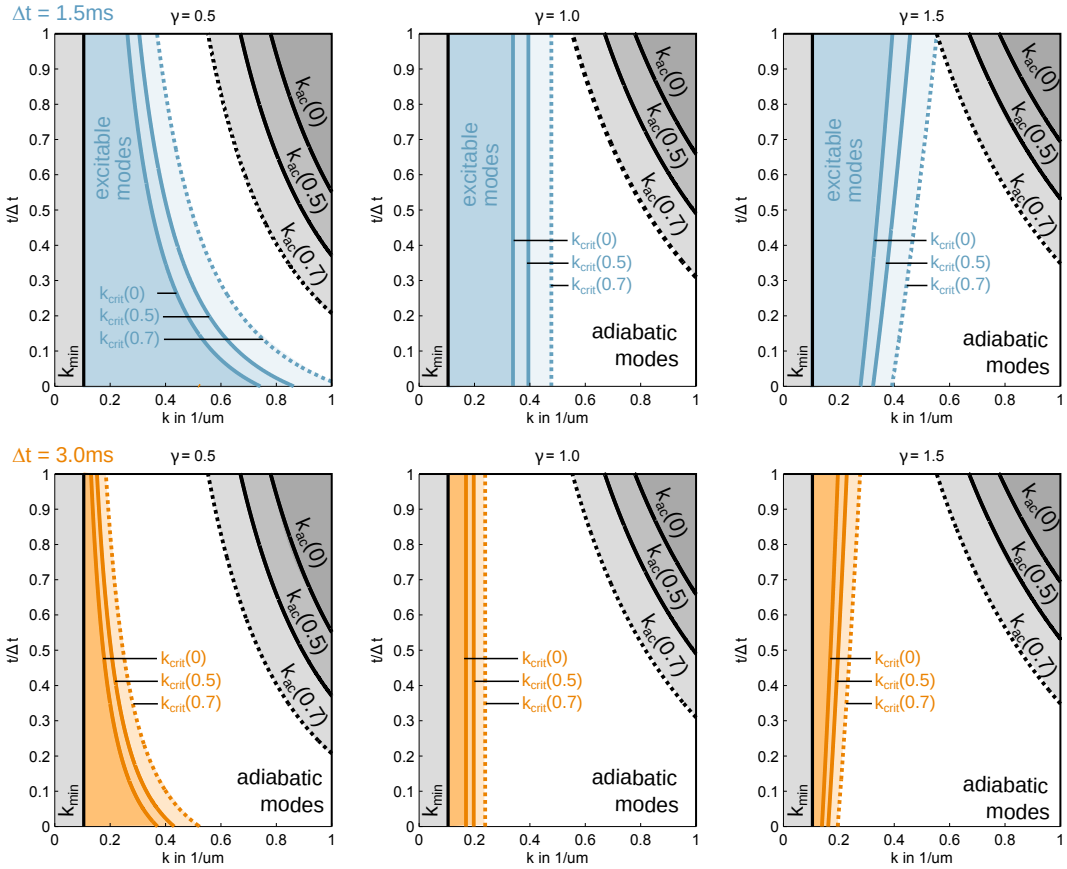

Figure 10.3: Time dependence of the critical mode for different ramp parameters. Modes can only be populated by an experimental ramp of the scattering length if they become non-adiabatic. k_{crit} marks the boundary between adiabatic and non-adiabatic modes at the center of the condensate and at a distance of $0.5\,r_{TF}$ and $0.7 r_{TF}$. The grey areas show modes that are forbidden due to the size of the system k_{min} or due to the breakdown of the acoustic regime k_{ac}. The latter is again shown for three different positions in the condensate. The different panels show different sets of experimental parameters, namely three different power-law exponents $\gamma = 0.5$ (left), $\gamma = 1.0$ (center) and $\gamma = 1.5$ (right) and two different ramp speeds $\Delta t = 1.5\,\mathrm{ms}$ (blue) and $\Delta t = 3.0\,\mathrm{ms}$ (orange). All ramps start at a scattering length of $400\,a_B$ and end at a scattering length of $50\,a_B$.

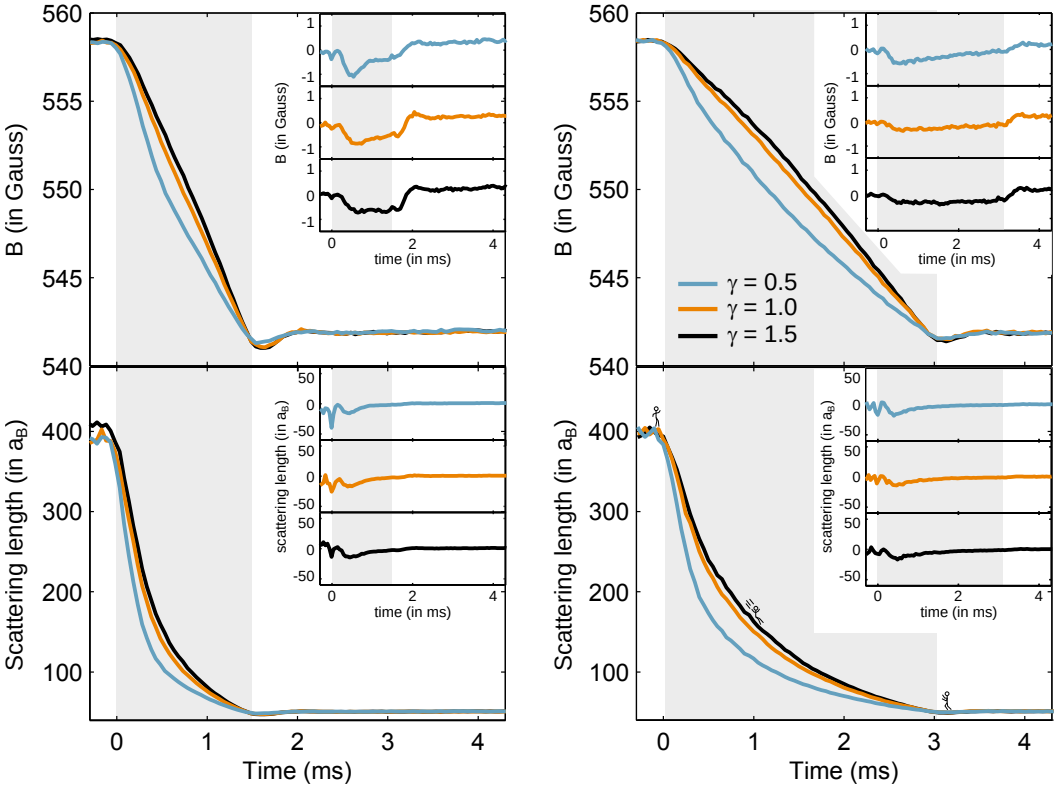

Figure 10.4: Measured ramp shapes. The magnetic field and scattering length during are extracted from a measurements of the current in the magnetic coils for the six different ramps with $\gamma = 0.5$ (blue), $\gamma = 1.0$ (orange) and $\gamma = 1.5$ (black) and for the two ramp durations $\Delta t = 1.5$ ms (left) and $\Delta t = 3.0$ ms (right). The grey areas mark the time during which the magnetic field is ramped and the inset show the residuals to the optimal ramp.

Apart from the first short peak at the onset of the ramp, the error in scattering length is always below $20\,a_B$ and much better for the slower ramp and the second half of the fast ramp. Thus we explicitly show that the different ramps can be clearly distinguished, and the selected ramp speeds are experimentally realizable.

The second dynamical adjustment is the change of trap frequency to ensure the static density distribution (see section 10.3). It is done via an acoustic optic modulator (AOM) that regulates the power in the trapping beam. This process is fast compared to the time scale of the ramp.

10.5 Density fluctuations and their correlation

Experimental runs with the previously determined parameters indeed show the appearance of structures, that are clearly visible even in single realizations. Figure 10.5 shows an example for the density distribution before the ramp in comparison with an image of the condensate after a 1.5 ms ramp with $\gamma = 0.5$. For a quantitative analysis of the fluctuation, we need the right observable. To identify this observable, we need to revisit the definition of the analog scalar field in the derivation of the acoustic metric. In eq. (4.6), the field Φ of the entire condensate was split into the background ϕ_0 and the real and imaginary part of the fluctuations ϕ_1 and ϕ_2

$$\Phi = \phi_0 + \phi_1 + i\phi_2 \ . \tag{10.14}$$

The perturbations ϕ_1 and ϕ_2 are related to the scalar field ϕ in the acoustic metric by $\phi_2 \propto \phi$ and $\phi_1 \propto \dot{\phi}/n_0(r)$ with $n_0(r)$ the density distribution of the background (see eq. (4.12)). To first order in the perturbations, the density distribution of the condensate is

$$n(t, r, \varphi) = \langle \Phi^* \Phi \rangle = n_0(r) + \sqrt{n_0(r)}\, \phi_1 + O(|\phi_1|^2, |\phi_2^2|) \ , \tag{10.15}$$

where $\phi_0^* = \phi_0$ and $\phi_0^2 = n_0(r)$ was used. Note that the leading term in the perturbation is an interference term with the background condensate. This amplifies the fluctuation signal and allows the detection of phases between the background condensate and the fluctuations. This will become very important later in this chapter. Reshuffling of the above formula together with the definition of ϕ_1 relates the derivative of the scalar field $\dot{\phi}$ to the density contrast defined as

$$\dot{\phi} \propto \delta \equiv \sqrt{\frac{n_0(r)}{\bar{n}_0^3}} \left[n(t, r, \varphi) - n_0(r) \right] \ . \tag{10.16}$$

The density contrast is rendered dimensionless by the normalization with the density at the center of the condensate $\bar{n}_0$. The lower panels in fig. 10.5 show the density contrast for the single realizations before and after the ramp, with under-densities shown in blue and over-densities shown in red.

The right-hand side of fig. 10.5 shows the central region of the condensate for three such realizations. The appearing fluctuation pattern is random between realizations. Thus, the background density can be experimentally determined as an average overall realizations

$$n_0(x, y) = \langle n(x, y) \rangle_e \ , \tag{10.17}$$

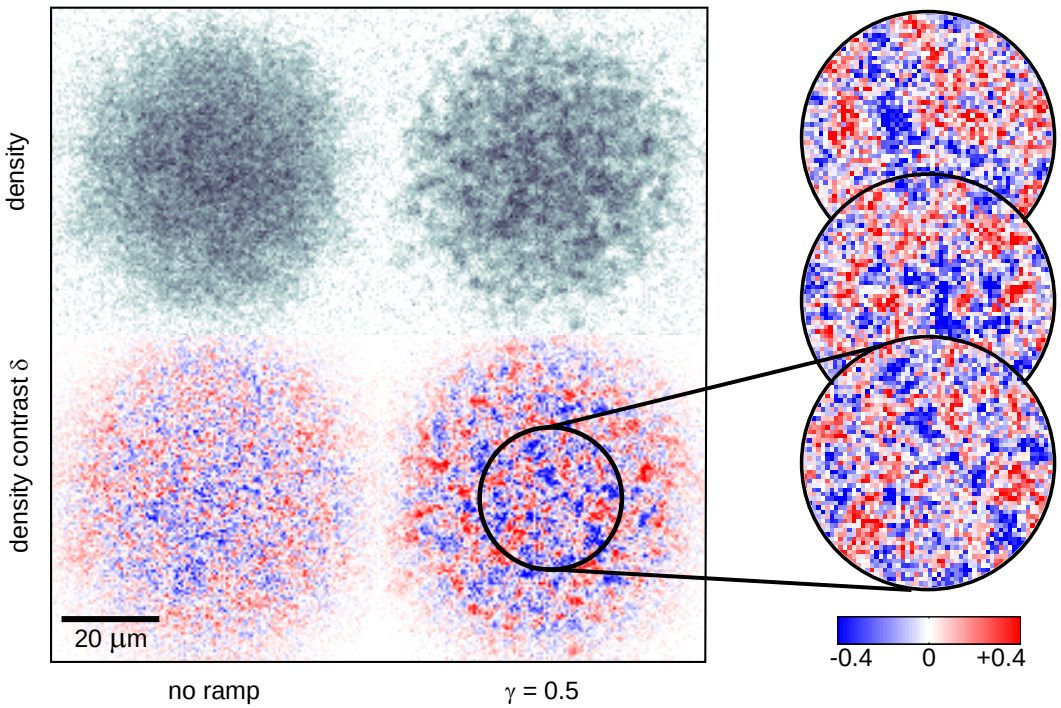

Figure 10.5: Appearance of fluctuations. The panels show the density and density contrast for single images of the condensate before and after a ramp with the ramp duration $\Delta t = 1.5$ms and the power-law exponent $\gamma = 0.5$ (decelerated expansion). The right-hand shows the random patterns in three different realizations. Only the central region of the condensate up to half the Thomas-Fermi radius is shown. This is the region used for the extraction of the correlation function.

where x and y denote the position of pixels in the image and the subscript, e abbreviates the ensemble average. The next higher statistical moment is the two-point correlation function $\mathcal{G}_{\delta\delta}(u, u', \varphi, \varphi') = \langle \delta(u, \varphi)\delta(u', \varphi') \rangle$. In two dimensions, the full density-density correlation is a four-dimensional object depending on the position of both points. However, the implemented analog spacetime is homogeneous and isotropic and all statistical objects in this space need to fulfill the same symmetries. Thus they can only depend on the distance L between points. In particular, this is the case for the correlation function $\mathcal{G}_{\dot\phi\dot\phi}$ eq. (9.18) which is proportional to the two-point correlation of the density contrast

$$\mathcal{G}_{\delta\delta}(t, L) = \frac{\hbar^2 m}{\lambda_f^2 \bar{n}_0^3} \mathcal{G}_{\dot\phi\dot\phi}(t, L) \,, \tag{10.18}$$

with the prefactor taken from [41]. Here, λ_f the 2d-coupling at the end of the analog

expansion and m the atomic mass. Since the two correlation functions are connected only by a constant factor, $\mathcal{G}_{\delta\delta}$ must, in turn, fulfill the same symmetries as $\mathcal{G}_{\dot{\phi}\dot{\phi}}$. It thus only depends on the distances L between points. Hereby, distances must be evaluated in the analog metric (see section 7.4 for the distances in the curved spaces). Experimentally, this is a great advantage. It allows the evaluation of the correlation function as

$$\mathcal{G}_{\delta\delta}(t, L) = \langle \delta(t, x, y)\delta(t, x', y') \rangle_{e,\, \text{distance}(x,y,x',y')=L} \,, \tag{10.19}$$

where the average runs overall realizations and over all pairs of pixels with distance L. This greatly improves statistical power for a limited number of experimental realizations. For the data shown here, around a 100 realizations per parameter set are available for analysis. To improve the signal-to-noise ratio, four pixels (two by two) are averaged before the start of the analysis. Numerically, the evaluation of the correlation function requires the distance evaluation and binning of all pixel-pairs. To perform the computation in a feasible time, it was implemented without loop logic. Details on the exact implementation and the analysis routine can be found in appendix B.

The condensate in a harmonic trap approximates a hyperbolic space described by the Poincare disk with the value of the curvature related to the Thomas-Fermi radius by $\kappa = -r_{TF}/2$ (see section 8.1). To extract the two-point correlation function of the density contrast, we use only a region up to half the Thomas-Fermi radius. At the edge of this region, the density of the condensate is already decreased to three-quarters of the central density. However, the implemented analog metric of the Poincare disk is still very well approximated by a flat Euclidean disk. To confirm this, the correlation function is evaluated using both a flat and a hyperbolic metric. The results are shown in fig. 10.6 together with the correlation function of the initial condensate. The close agreement between the flat and the hyperbolic evaluations justifies the analysis in the flat metric. It will be used for the remainder of this work.

Of particular interest is the difference between the correlation functions of the perturbed and unperturbed condensate. For the latter, the correlation function flattens quickly after the initial peak. After the sweep of the scattering length, however, the correlation shows a pronounced anti-correlation at a length scale of $5\,\mu$m followed by a correlation peak. This is the first indication of analog particle production in the condensate.

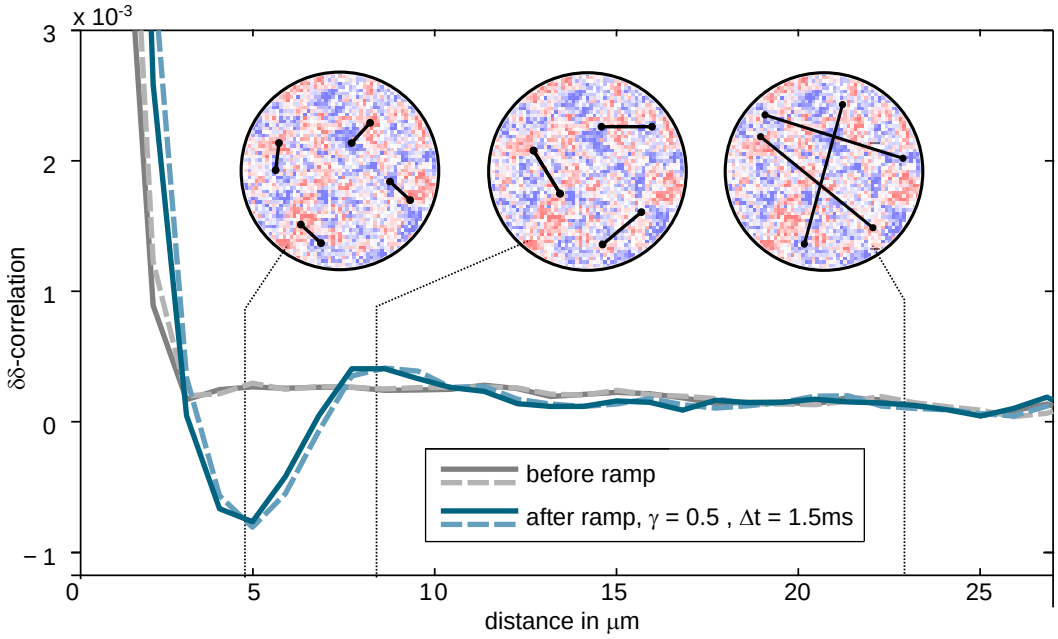

Figure 10.6: Density-contrast correlation function. A clear difference is visible between the correlation function of the condensate before the ramp (grey), and after the ramp (blue). The correlation functions are computed once with a flat metric (solid line) and with a hyperbolic metric (dashed line). The good agreement between flat and hyperbolic analysis justifies the continued use of the flat metric. The insets give examples for pixel-pairs entering in the calculation of the correlation functions.

10.6 Time evolution of the correlation

A single snapshot in time only partly characterizes the quantum state created during the ramp of the scattering length. Similar to [36, 37, 40], we extract additional information about the quantum state from the time evolution of its correlation functions.

For that purpose, the scattering length is held constant for a time t_h after the ramp, before imaging the density distribution of the atoms. The density-contrast correlation function is extracted as described in the previous section and the results are shown in fig. 10.7 for a ramp with $\gamma = 1/2$ (decelerated expansion) and two different ramp durations. It reveals propagation of the correlation structure to larger distances. In the data, the correlation peak propagates with the velocity of

$$v_{\text{prop}} = 2.5 \pm 0.1 \, \frac{\mu\text{m}}{\text{ms}} \, , \tag{10.20}$$

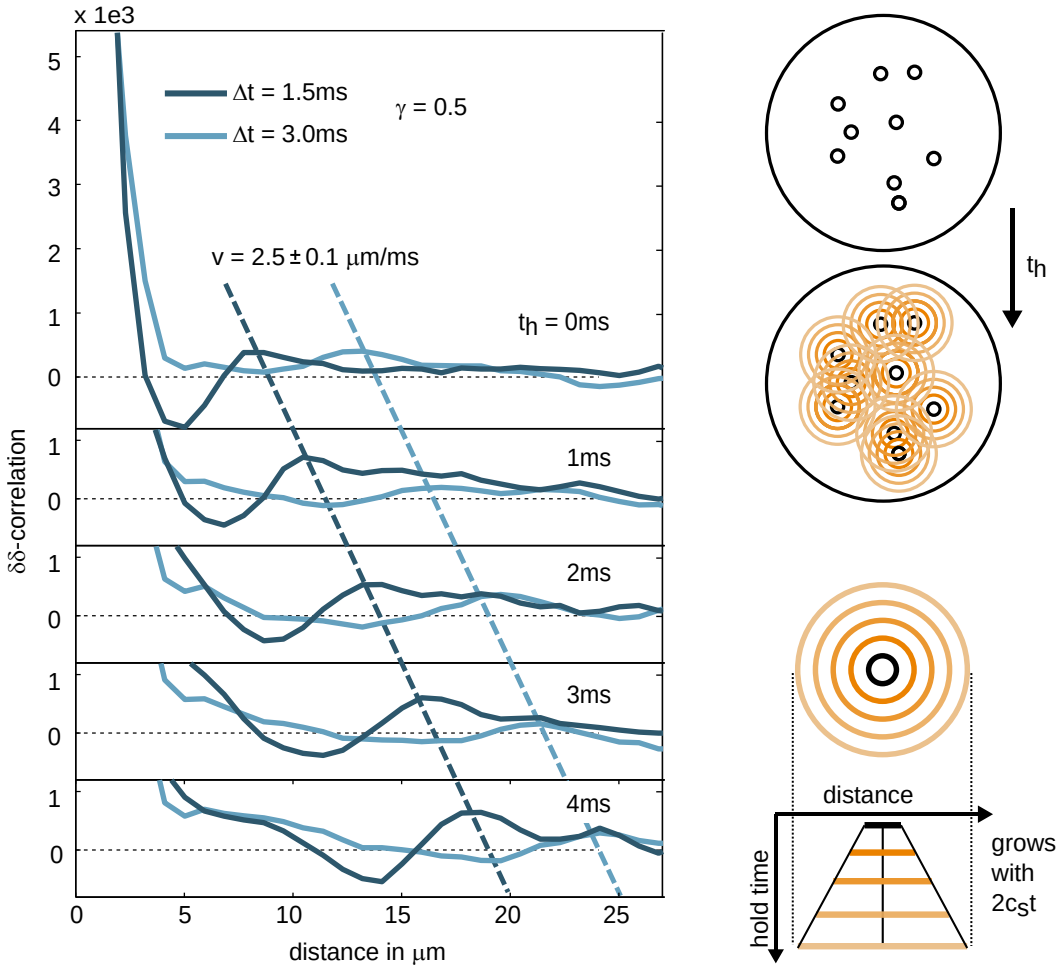

Figure 10.7: Time evolution of the density-contrast correlation. During hold time t_h after the ramp at constant scattering length, the correlation feature propagates towards larger distances. The extracted propagation speed is the same for both ramp durations and is consistent with the speed of sound. The right-hand side shows a real-space interpretation of the propagation. Perturbations created during the ramp are the seeds for circular waves, and their interference forms a complex pattern. However, the structure of the circular wave leaves a distinctive correlation peak at the diameter of the sound cone.

for both ramp durations. The speed of sound can be predicted from GPE simulation of the condensate groundstate to be $c_s = 1.3\,\mu\mathrm{m/ms}$[2]. The propagation of the correlation peak is consistent with twice the speed of sound. An interpretation of this observation is shown on the right-hand side of fig. 10.7: the ramp of the scattering length creates perturbations at random positions in the condensate. The perturbations propagate radially outwards with the speed of sound. The superposition of several perturbations creates a complex interference pattern, but the underlying sound cone is still detectable in the correlation. It results in a correlation peak appearing at the cone's diameter, which grows with twice the speed of sound. The evolution is the real space equivalent of Sakharov oscillations [104] in momentum space. To understand this phenomenon, the power spectrum of the correlations is computed in the following section.

10.7 The spectrum and its time evolution

The propagation of the correlation peak can be understood in more detail in momentum space. For that purpose, we compute the power spectrum of the fluctuations from the density-contrast correlation function using eq. (10.18) and eq. (9.19). In a flat metric, the correlation function and the power spectrum are connected by a Hankel transform with $m = 0$

$$S_k = \frac{\bar{n}_0\, m}{\hbar\, a_f}\frac{1}{k}\int \mathrm{d}L\, L\, J_0(kL)\, \langle \delta_c \delta_c \rangle\, (L), \tag{10.21}$$

where $J_0(kL)$ are the Bessel functions of the first kind. As argued before, the approximation of the flat metric is justified for the analyzed region of the condensate. The Hankel transform is the equivalent to a Fourier transform in polar coordinates. This reflects the rotational symmetry that already reduced the correlation function to an object that only depends on distances[3]. Both $\bar{n}_0 = c_{s,f}^2\, \lambda_f$ and $a(t_f) = 1/c_{s,f}$ are directly related to the speed of sound and the 2d-coupling λ (eq. (2.7)) at the end of the ramp. As a value for the speed of sound $c_{s,f}$ we take half the propagation velocity of the peak in the correlation function. The Hankel transformation is performed numerically using the Matlab package [105]. Figure 10.8 shows the spectra for

[2]The speed of sound can also be estimated in the Thomas-Fermi approximation from the size of two-dimensional condensate in the trap. However, this assumes the condensate to be truly two-dimensional, which is not the case. The estimated sound speed is lower than the GPE simulation value.

[3]Note that this is not the spherical symmetry of the condensate but the symmetry of the implemented spacetime.

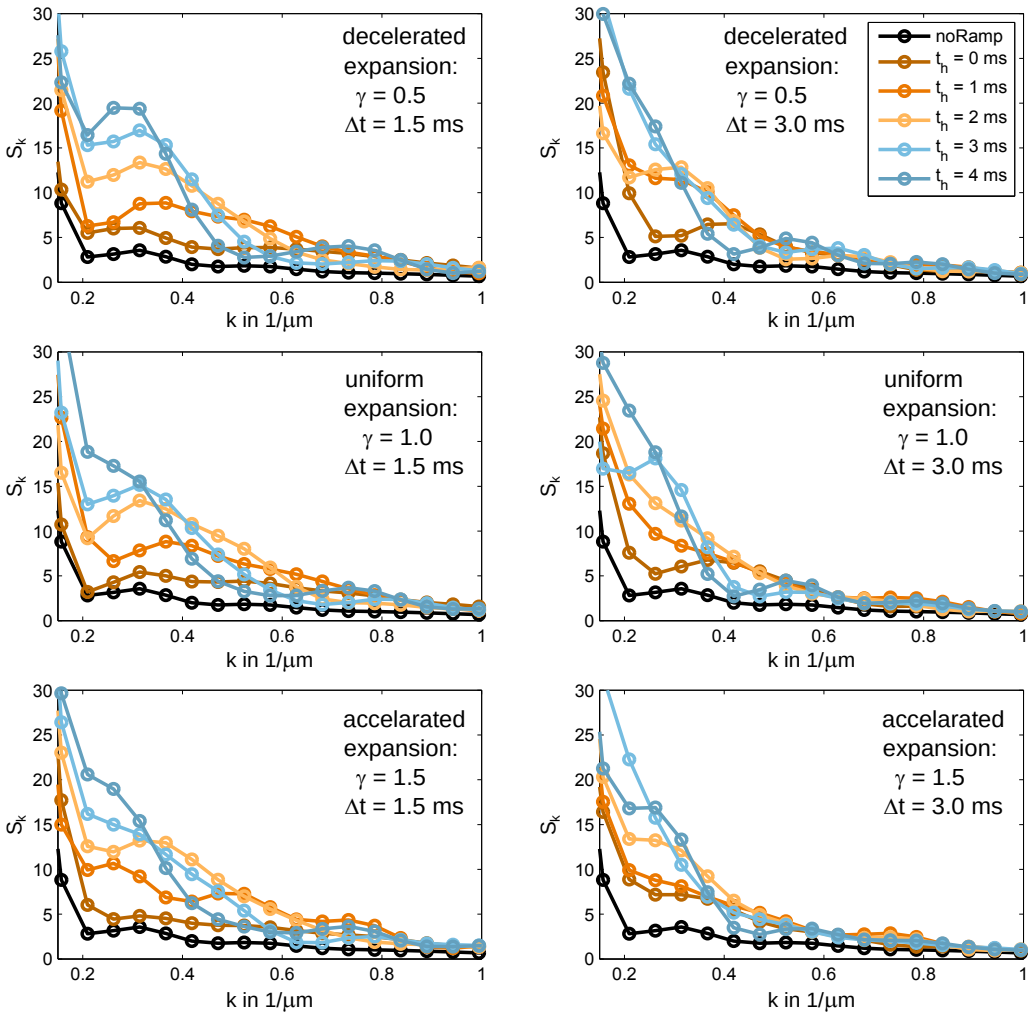

Figure 10.8: Time evolution of the power spectrum. The power spectra are a Hankel transform of the density-contrast correlation function. The spectra show a clear increase in power for all the six different ramps compared to the unperturbed condensate (black line). As expected from adiabaticity arguments, larger k modes are excited for the faster ramp. The time evolution after the ramp (different colors) can even result in an increase in power even though particle-pair production has ceased. This is caused by a phase evolution of a coherence term which is detectable by an interference between the background condensate and the different k-modes.

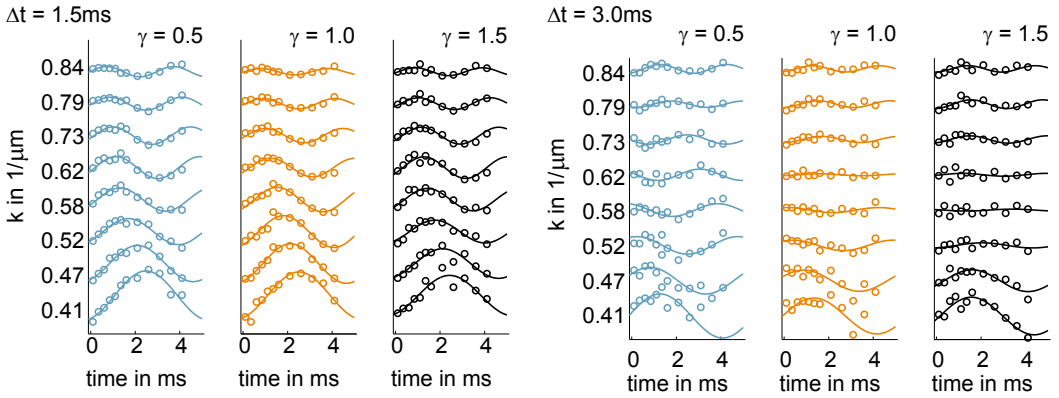

Figure 10.9: Oscillations of the momentum modes. Each momentum mode oscillates in time with a frequency proportional to $2c_{s,f}\,k$. The solid lines are fits of that frequency with offset initial phase and amplitude as fit parameters.

the three different power-law exponents and the two different ramp durations. The plots show the time evolution of the spectra after the ramp and reveal an intriguing feature. The power in many k-modes increases after the ramp even though particle creation should have ceased with the end of the analog expansion. A plot of the power in each k-mode against time in fig. 10.9 reveals an oscillating behavior. These are Sakharov oscillations caused by a buildup of phase difference between two counter-propagating modes of the same k. Sakharov oscillations are a typical sign for particle-pair creation and have been observed in quench experiments [36, 37, 40]. They are connected to the coherence term ΔN_k eq. (9.23) that appears in the spectrum eq. (9.20). From the coherence term, the complex phase of each k-mode is predicted to oscillate with a frequency of $2\omega_k = 2c_{s,f}k$. In the experiment, these oscillations become visible due to an interference of the momentum modes with the background condensate, similar to a heterodyne detection in quantum optics. Figure 10.9 checks this prediction against the experimental data. It shows the time evolution of each k-mode together with a cosine fit. The frequency of the fit is fixed according to the above prediction with the speed of sound taken from the propagation of the correlation peak in fig. 10.7. For the fit, an offset, amplitude, and the initial phase of the oscillation are left as free parameters.

The best-fit values for the phase and amplitude are shown in fig. 10.10 together with the analytical predictions from particle pair creation in an expanding spacetime[4]. The theoretical prediction use a final speed of sound of $c_{s,f} = 1.2\,\mu$m/ms and an

[4]courtesy of the theory team of our collaboration: Álvaro Parra-Lopéz, Mireia Tolosa-Simeón, Natalia Sánchez-Kuntz, Tobias Haas and Stefan Flörchinger

initial scattering length of $a_{s,i} = 350\, a_B$ and a condensate temperature of $T = 40\,\mathrm{nK}$. The first two values are within the error bounds of the experimentally extracted speed of sound and the position of the Feshbach resonance, respectively. The temperature of the condensate was independently determined from its density distribution in the trap [106] to be $T = 60 \pm 10\,\mathrm{nK}$. We attribute the discrepancy between the two temperatures to the location of thermal fluctuations in a harmonically trapped condensate: they are pushed towards the edges of the cloud [106], which results in an effectively lower temperature in the analyzed region around the center of the condensate. The good agreement between predictions and measurements confirms that we indeed observe the analog process of particle-pair creation in an expanding spacetime. This confirms the successful implementation of the dynamics of a scalar field in an analog curved spacetime and paves the way for future experimental investigation of such phenomena.

Remarkably by itself is the k-dependence of the phase in the lower right panel in fig. 10.10. This is the phase eq. (9.24) in the coherence term of the produced quantum state corresponding to the initial phases of the k-mode oscillation in the experimental data. Both prediction and observation show a clear difference for the three different expansion scenarios. The theoretical prediction shows that this feature is independent against the temperature of the initial state. In addition, it is robust against noise. Noise sources may easily add power to different k-modes in the spectrum but will not create an oscillating signal. Other effects, like damping, may distort the oscillation amplitude but not its phase. The observed phase feature is thus a reliable marker for the expansion history.

10.8 Connection to horizons?

The marker for the expansion history identified in the previous section can possibly be explained in terms of horizons. Horizons have been discussed in the context of the mode equation (9.11) which in term determines the spectrum of the produced particles [33, 101]. Here, we will take an approach that connects the Hubble horizon to the critical mode in the adiabaticity criterion (see section 10.4).

For the definition of the Hubble horizon, imagine an observer located in a homogeneous and isotropic expanding space. Due to the expansion, objects will move away from her, with the velocity proportional to the distance (Hubble's law [5]). At any time t, the Hubble radius is defined as the distance at which this velocity is equal to the speed of light. This is equivalent to

$$R_{\mathrm{Hubble}} = \frac{1}{H}\,, \tag{10.22}$$

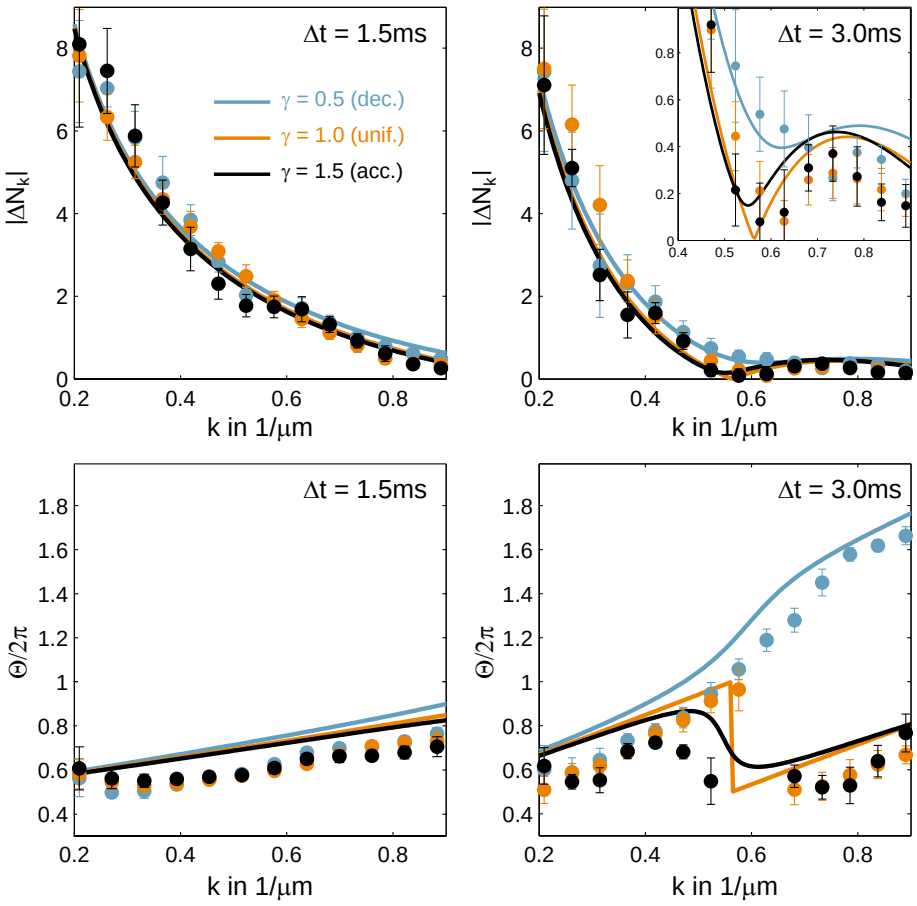

Figure 10.10: Amplitude and initial phase of the coherent oscillations. The amplitude $|\Delta N_k|$ and initial phase Θ of the k-mode oscillations are shown for two different ramp durations $\Delta t = 1.5\,\mathrm{ms}$ (left) and $\Delta t = 3.0\,\mathrm{ms}$ (right), and the three different expansion scenarios (colors). The experimental data points are the fit parameters of the oscillations with a one-std error from the fit. The solid lines are the theory predictions from the quantum state produced during the ramps. The good agreement confirms that the observed fluctuations in the condensate are caused by the process of cosmological particle pair production in the analog expanding spacetime. Remarkable in itself is the feature appearing in the initial phases of the slow ramp (lower-right panel). It shows a clear dependence on the different expansion scenarios and is a robust marker for the expansion history.

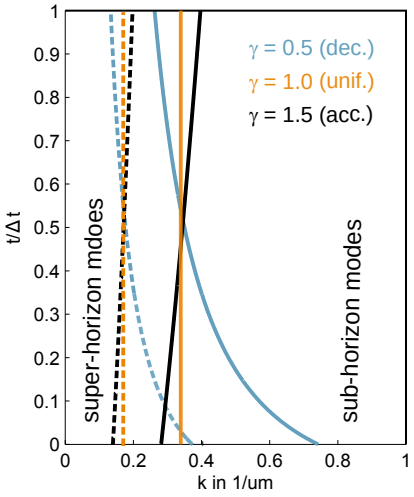

Figure 10.11: Evolution of the comoving Hubble horizon. For the uniform expansion with $\gamma = 1.0$ (orange), the comoving Hubble horizon remains at the same momentum mode. The solid line describes the fast ramp with $\Delta t = 1.5$ms and the dashed line the slow ramp with $\Delta t = 3$ ms.[5] For the accelerated expansion (black line), the horizon moves to larger k during the ramp, i.e., the horizon shrinks. For the decelerated expansion (blue line) the horizon grows.

with $H = \dot{a}/a$ the Hubble parameter. As in the previous chapters, a has the unit of an inverse velocity, and distances are measured in time. In comoving coordinates, the Hubble radius is

$$\eta_{\text{Hubble}} = \frac{R_{\text{Hubble}}}{a} = \frac{1}{\dot{a}} \,, \tag{10.23}$$

which can be connected to the adiabaticity criterion (see section 10.4). The latter states that a mode with energy E and dispersion relation $\omega = c_s k$ can be occupied if

$$\left|\frac{\hbar}{E}\right| > \left|\frac{E}{\dot{E}}\right| \quad \Leftrightarrow \quad |k_{\text{crit}}| < \left|\frac{\dot{c}_s}{c_s^2}\right| = |\dot{a}| = \frac{1}{\eta_{\text{Hubble}}} \,. \tag{10.24}$$

Here, the relation between the scale factor and the speed of sound $c_s = 1/a$ and $\dot{c}_s = -\dot{a}/a^2$ in the acoustic metric was used. This shows that modes can only be populated if their momentum is smaller than the inverse horizon. These are modes with a wavelength larger than the horizon (super-horizon modes). Modes with wavelengths smaller than the horizon (sub-horizon modes) cannot be excited.

The evolution of the horizon during the different expansions (see fig. 10.10) qualitatively explains the different features in the k-dependence of the initial phase.

For the uniform expansion with $\gamma = 1$, the horizon is at a fixed k for the entire ramp duration. Two neighboring modes on different sides of the horizon experience a very different evolution during the ramp, leading to the very sudden jump in the initial phase. For $\gamma = 1.5$, the accelerated expansion, the comoving horizon shrinks, and the k corresponding to the horizon grow over time. Thus, k modes cross from inside the horizon to outside. They can be excited only after that crossing. Two neighboring modes differ in the time of their crossing but are not clearly separated by the horizon. This softens the jump of the initial phase in fig. 10.10. For the decelerated expansion with $\gamma = 0.5$, the comoving horizon grows, and modes cross from outside the horizon to inside. The k-range swept by the horizon is very wide, which explains the slow change of the initial phase for this scenario.

While this discussion may explain the shapes of the phase features for the different types of evolution, this order-of-magnitude estimation does not predict the correct position of the jumps. We suspect that the exact position may be related to the cosmological event horizon, which differs from the Hubble horizon for power-law expansions. However, understanding these relations and connecting them to the mode equation remains a task for the future.

Chapter 11

What was achieved and what is to come

With this work, we introduce a new cold atom experiment of potassium-39 that has recently become operational and will grow into an integral part of the Heidelberg research. This new machine was used to experimentally test a novel mapping between the dynamics of a scalar field in a curved and expanding spacetime and the phononic excitations of a circularly symmetric, quasi-two-dimensional Bose-Einstein condensate.

The first major result is the experimental confirmation that a harmonically confined Bose-Einstein condensate can implement a hyperbolic space with constant curvature – one of the possible spatial curvatures of an FLRW metric. This is the first demonstration of such a space in an analog system. Building on these results, a straightforward upgrade of the experimental setup by a digital micromirror device (DMD) will enable the implementation of different curvatures. Just recently, our experimental team has achieved this upgrade, and first measurements in an analog spherical geometry have been successfully performed [42]. With the DMD, more complex, non-homogeneous spaces can be implemented. This opens intriguing possibilities for the study of scalar fields in curved spaces beyond the symmetry assumptions of theoretical models.

The second result of this work is the realization of an analog expanding spacetime, implemented with a ramp of the scattering length. We observe the appearance of fluctuations in the condensate and extract their correlation functions and power spectra. Using the time evolution of these observables, we characterize the quantum state created by the expansion. The good agreement with theoretical predictions confirms that the fluctuations in the condensate are indeed caused by particle-pair

production. We thus simulate the quantum process that likely seeds the Universe's large-scale structure. Furthermore, we identified a clear and robust marker for the spacetime's expansion history in the time evolution of the power spectrum. To the best of our knowledge, it is the first time this feature has been identified. It is not yet clear whether this marker can be connected to observations of real cosmological phenomena, like the baryon acoustic oscillations, but it is an intriguing prospect for future research.

This work also has implications for phenomena intrinsic to a Bose-Einstein condensate, which can be reinterpreted and thus better understood in the framework of curved spacetimes and differential geometry. The concepts of curvature, cosmological particle production, or horizons can be applied to phenomena native to a Bose-Einstein condensate. This can significantly contribute to our understanding of quantum phenomena and may lead to entirely new avenues of research.

Appendix A

A.1 Setup magneto-optical traps

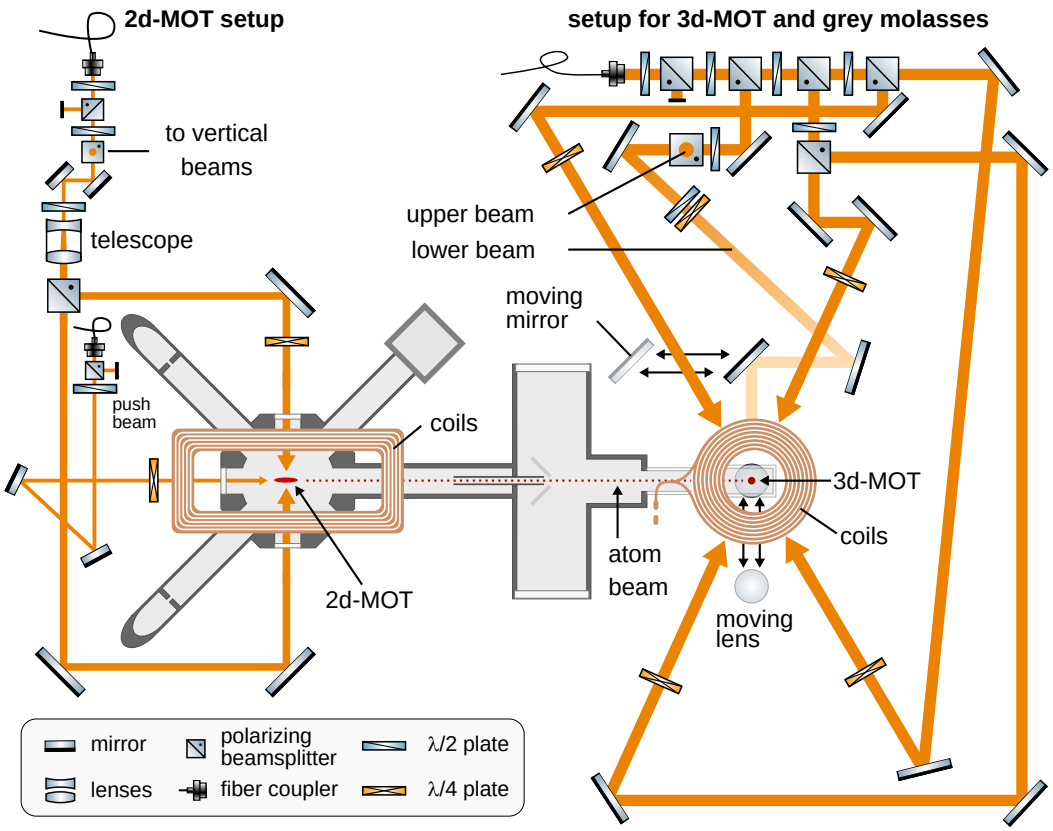

Figure A.1: Detailed drawing of the 2d-MOT and 3d-MOT setups.

A.2 Frequency stabilisation D1 and D2 master lasers

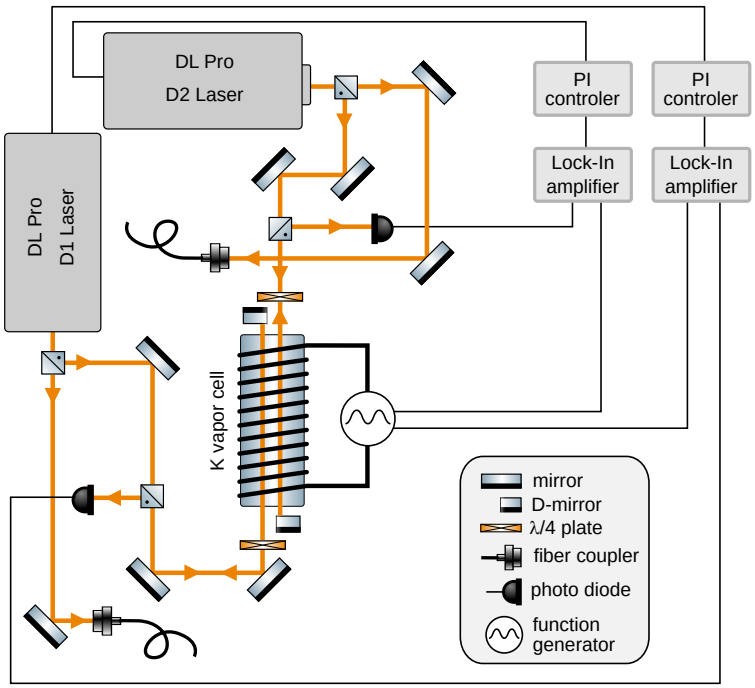

Figure A.2: The D2 and D1 master lasers are locked on the potassium-39 resonances with Doppler-free absorption spectroscopy. For the creation of the error signal, a magnetic field at the potassium vapor cell is modulated with 86 kHz. The light of each laser is coupled into a single-mode, polarization-maintaining optical fiber and amplified by tapered amplifiers (the amplification is not shown here).

A.3 Frequency adjustment and mixing for MOTs and molasses

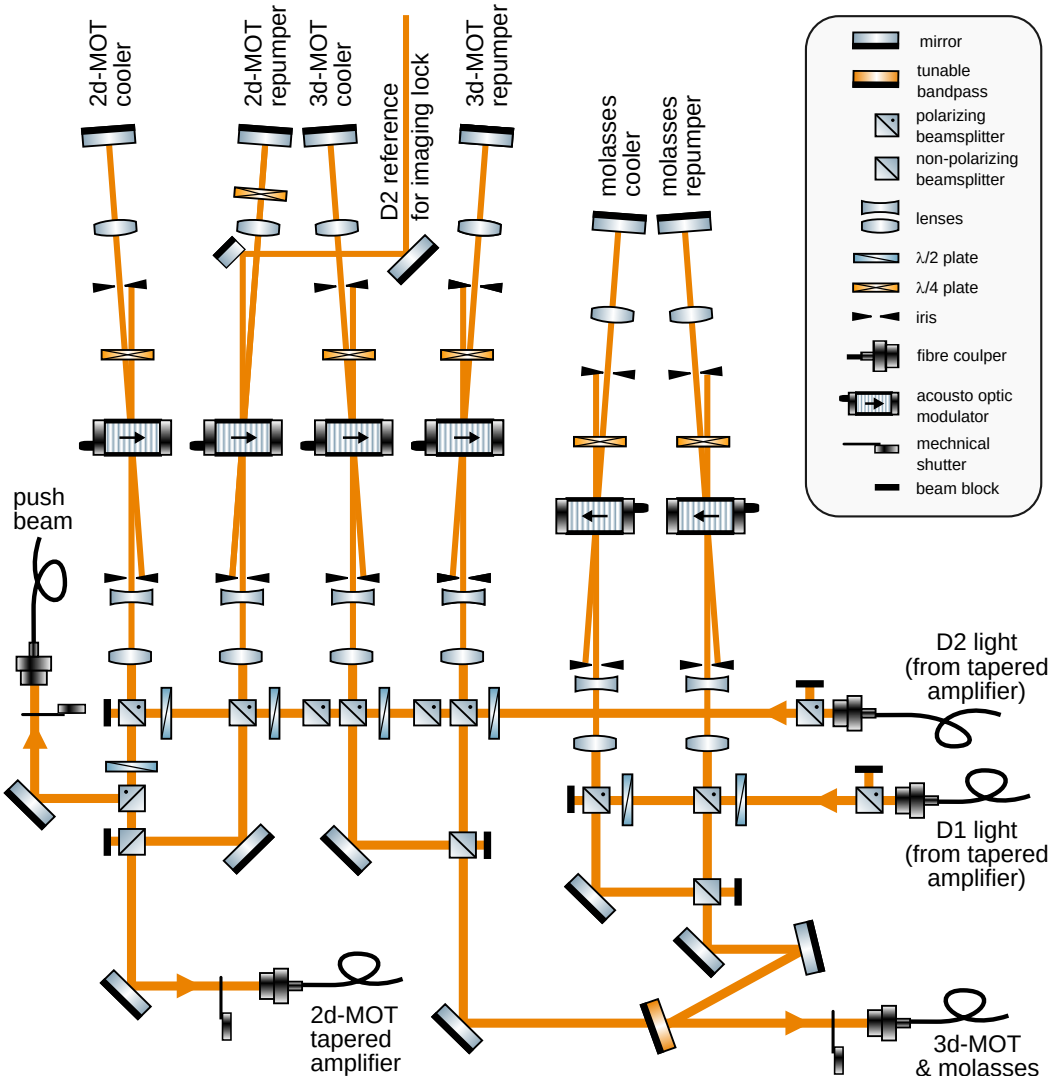

Figure A.3: The amplified lights from the D2 and D1 master lasers are adjusted to the right frequencies for 2d-MOT, 3d-MOT, and grey molasses. This is done with acousto-optical modulators in a double pass setup. The lights are mixed and coupled into the respective fibers. The light for 3d-MOT and grey molasses use the same fiber, mixing is done with a tunable bandpass.

A.4 Imaging laser - offset lock

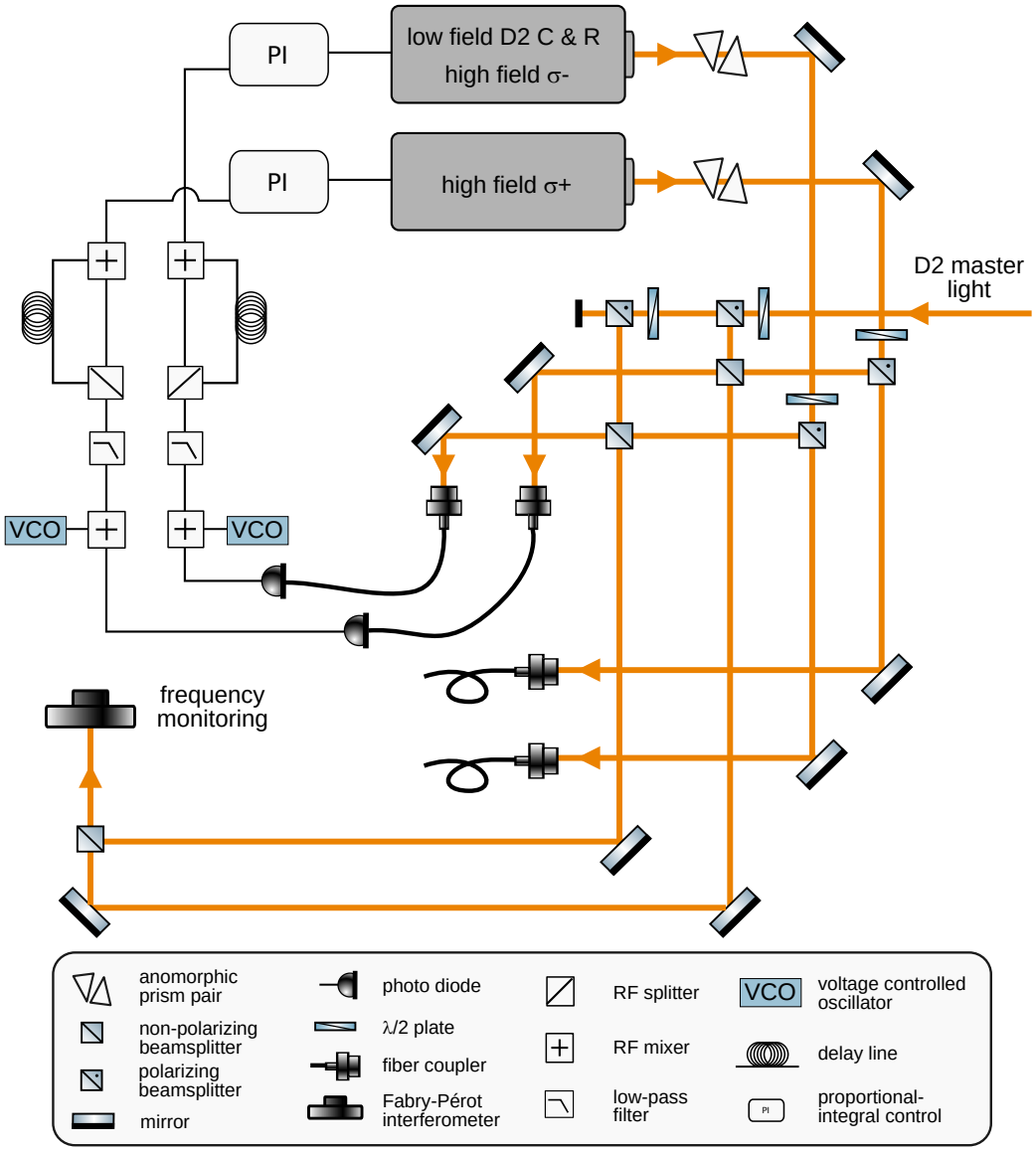

Figure A.4: The imaging lasers are offset locked onto reference light from the D2 master laser. The first laser creates the light for low field imaging. For a different offset in the lock, it also creates the σ^--light for high field imaging. The second laser creates the σ^+ light for high-field imaging. Both lasers are coupled into fibers to be transported to the mixing setup (next figure).

A.5 Imaging laser - mixing

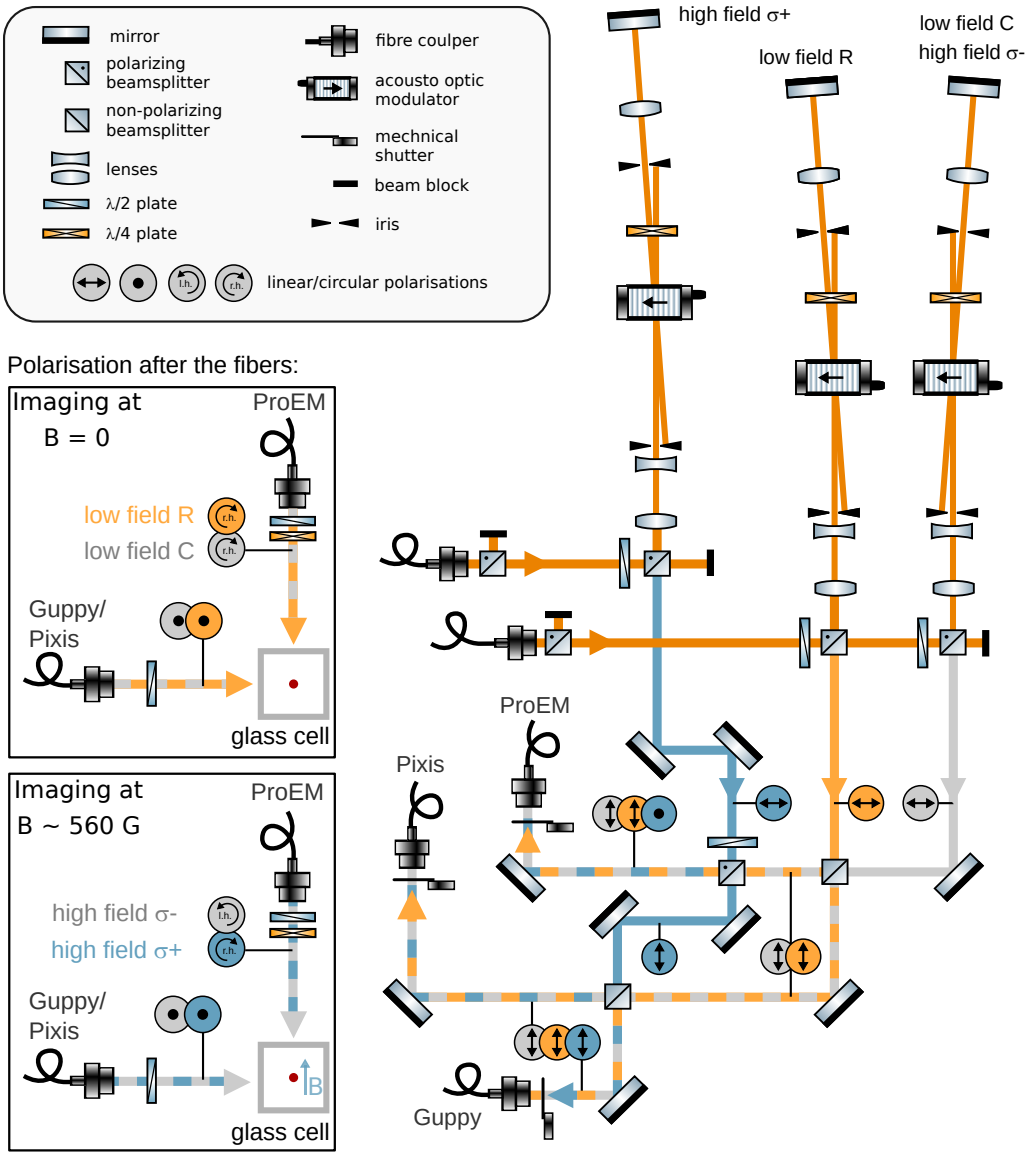

Figure A.5: Switching and frequency adjustment of the imaging lights is done with acousto-optical modulators in a double-pass setup. For imaging at zero magnetic fields, the second and third AOM paths (from the left) are used. For imaging at the high magnetic field, the first and the third path are used. The lights are mixed and coupled into three fibers for the three different absorption imagings. The polarization of the lights is indicated for the different mixing steps and after the fibers (insets on the left).

A.6 High power laser system 1064 nm light

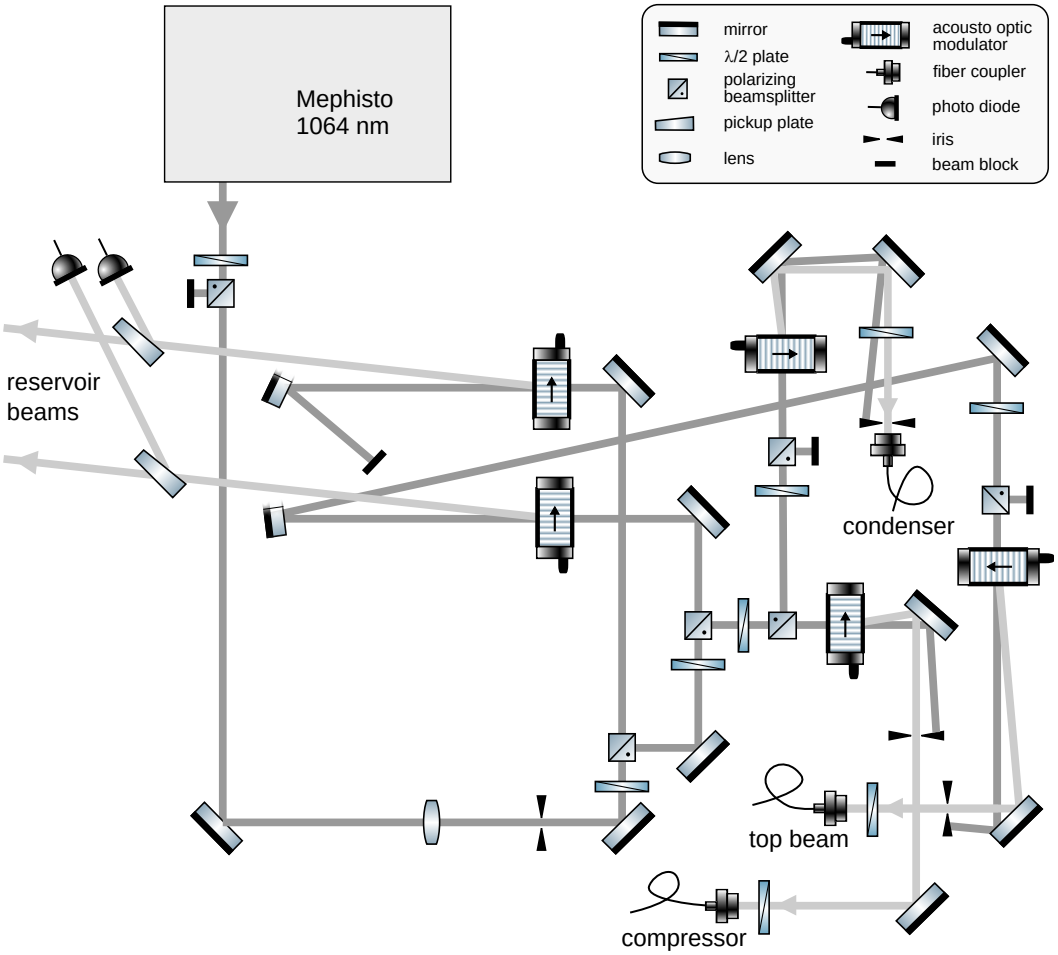

Figure A.6: For the attractive dipole beams, a total of five beams is used. The two reservoir beams have up to 12 W each and are arranged in a free-space setup. The other three beams (compressor, condenser, and top beam) are fiber-coupled with a maximum of 2 W in each beam. Switching and power control are done with acousto-optical modulators. For the top beam, the zeroth AOM order from one of the reservoir beams is reused.

A.7 High power laser system 532 nm light

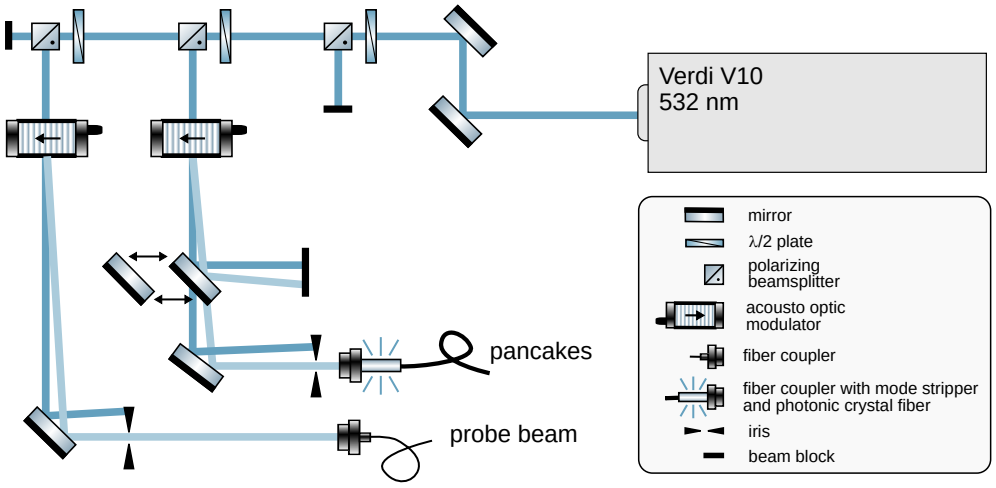

Figure A.7: There are two repulsive dipole traps using 532 nm light. Switching and power control are achieved with acousto-optical modulators. The probe beam needs less 1 mW in power and a normal fiber can be used. The beam for the pancake interferometer needs up to 2 W after the fiber. For green light, this is not possible with an ordinary single-mode fiber due to induced Brillouin scattering. A photonic crystal fiber is used instead. A moving mirror blocks the light from reaching the fiber during the early stages of the experimental sequence. This allows keeping the pancake AOM turned on most of the time. This reduces the thermal effects in the AOM and leads to a more stable coupling into the fiber.

APPENDIX B

Extraction of correlation functions and spectra

For the extraction of the correlation function, all experimental shots within one parameter set are used that deviate less than 10% from the mean atom number (see fig. B.1 for illustration). To improve the signal to noise, four pixels (two by two) are averaged to form a larger pixel. For each image, an offset is determined from the regions far away from the atom cloud, and this offset is subtracted. An average over all shots yields a mean image. The Thomas-Fermi radius r_{TF} is extracted from a fit to the profile. A mask is created that leaves pixel values unchanged for the central region up to half the Thomas-Fermi radius and sets all other pixels to NaN values. This mask is used both on the mean image and on all individual images. To correct for fluctuations in the atom number, the mean image is scaled to each individual shot. The factor for this scaling is chosen such that the signal for the mask region is the same in the individual shots and in the mean image. From each pair of images and corresponding rescaled mean image, the density contrast (eq. (10.16)) is calculated. From the density contrast, the two-point correlation functions are evaluated for each image and then averaged for the final result. Finally, the power spectrum is calculated by a Hankel transform of the correlation function.

A loop-free algorithm is used for the extraction of the calculation functions. It is written in such a way, that it also works if distances between two points are evaluated for hyperbolic and spherical geometry. fig. B.2 illustrates the extraction for a small mask region, containing only five pixels. In the first step, all non-NaN pixels are arranged in two matrices as is illustrated in the picture. The matrices are constructed such, that they contain all pairs of pixels exactly once (with the first 'member' of the pair in the first matrix and the second 'member' in the second matrix). This matrix structure is used to record the x and y-positions of the pixels and for the pixel values themselves. From the position, the distance between the pixels of each pair is calculated. The figure illustrates this for a flat metric, but instead, a spherical or hyperbolic distance measure can be used. For each distance (or distance-bin in the real data), a distance mask is created. These masks select the corresponding pixel pairs in the matrices of the pixel values. Once masked, an entry-wise multiplication and average over the non-NaN pixels yield the value for the correlation function at the corresponding distance.

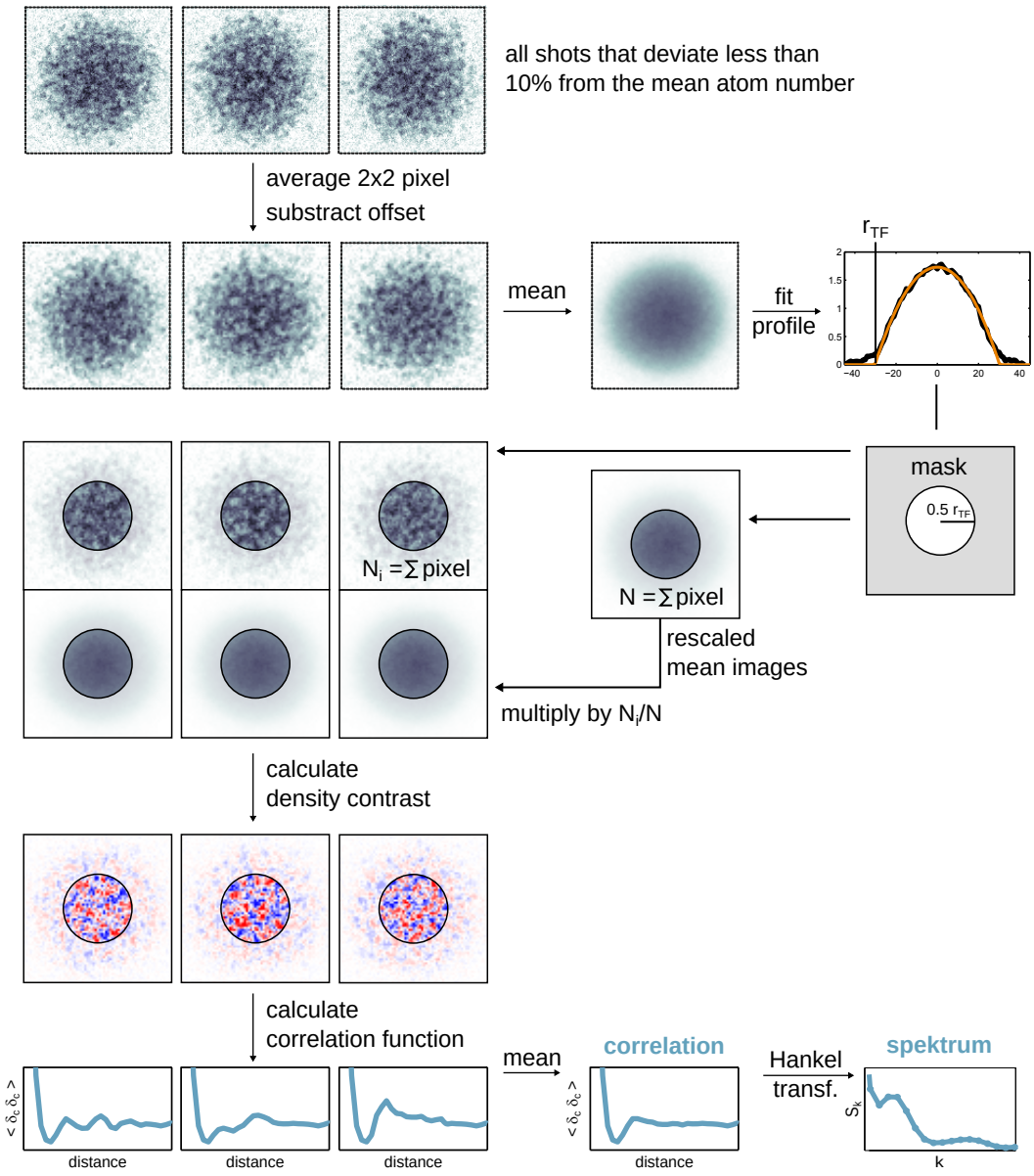

Figure B.1: Data processing for the extraction of correlation functions and spectra. The description is provided on the previous page

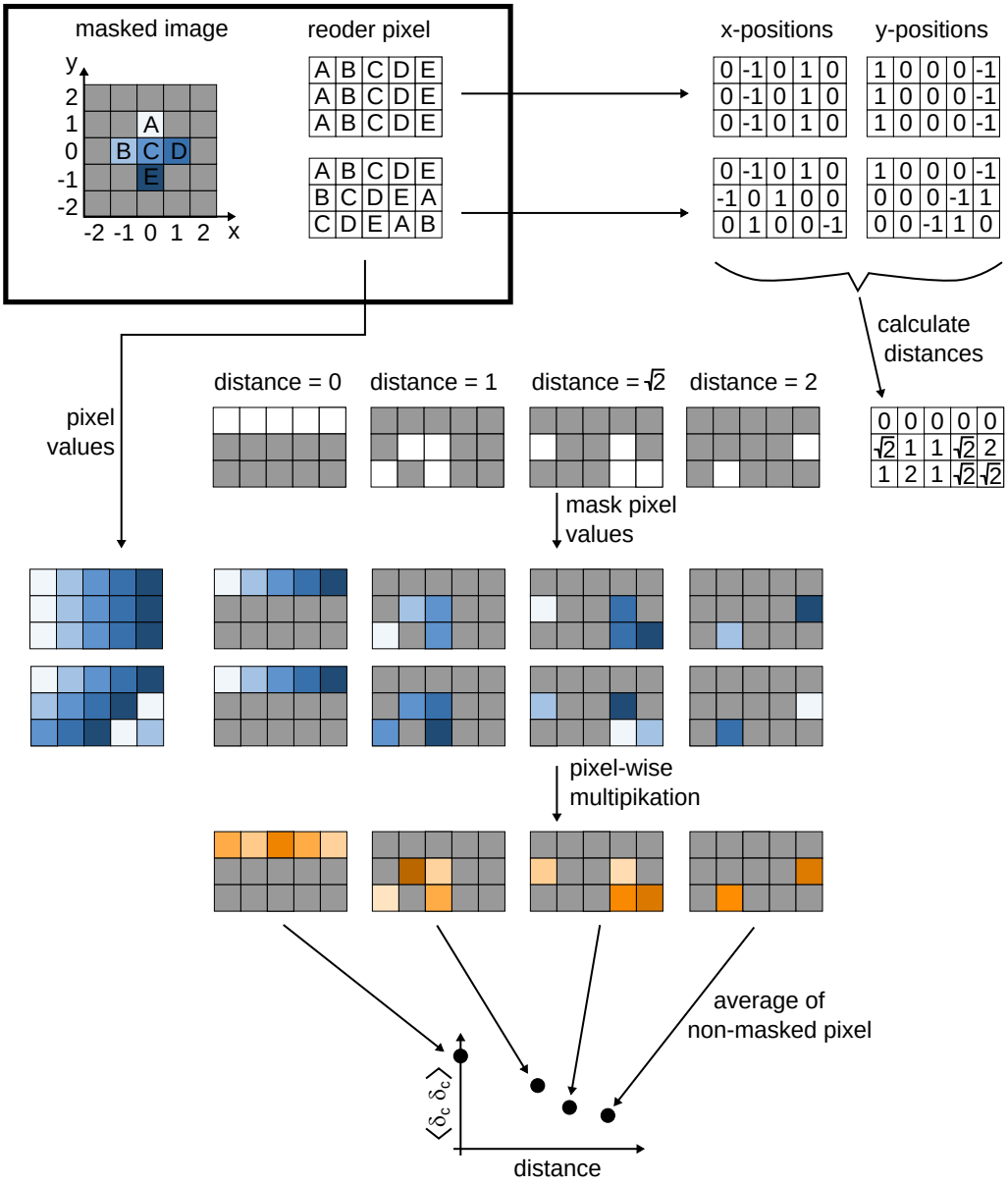

Figure B.2: Loop-free calculation of the correlation functions.The description is provided on the previous page

List of Publications

Publications related to this work

- C. Viermann, M. Sparn, N. Liebster, M. Hans, E. Kath, Á. Parra-López, M. Tolosa-Simeón, N. Sánchez-Kuntz, T. Haas, H. Strobel, S. Floerchinger and M. K. Oberthaler. *Quantum field simulator for dynamics in curved spacetime*. arXiv, 2202.10399 (2022).

- M. Tolosa-Simeón, Á. Parra-López, N. Sánchez-Kuntz, T. Haas, C. Viermann, M. Sparn, N. Liebster, M. Hans, E. Kath, H. Strobel, M. K. Oberthaler and S. Floerchinger. *Curved and expanding spacetime geometries in Bose-Einstein condensates*. arXiv, 2202.10441 (2022).

- M. Hans, F. Schmutte, C. Viermann, N. Liebster, M. Sparn, M. K. Oberthaler and H. Strobel. *High signal to noise absorption imaging of alkali atoms at moderate magnetic fields*. Review of Scientific Instruments **92**, (2021)

Prior publications

- C. Viermann, F. Fabis, E. Kozlikin, R. Lilow and M. Bartelmann. *Nonequilibrium statistical field theory for classical particles: Basic kinetic theory*. Phys. Rev. E **91**, 062120 (2015).

- C. Viermann, J. T. Schneider, R. Lilow, F. Fabis, C. Littek, E. Kozlikin and M. Bartelmann. *A Model for Hydrodynamics in Kinetic Field Theory*. arXiv, 1810.13324 (2018).

- M. Bartelmann, E. Kozlikin, R. Lilow, C. Littek, F. Fabis, I. Kostyuk, C. Viermann, L. Heisenberg, S. Konrad and D. Geiss. *Cosmic Structure Formation with Kinetic Field Theory*. Annalen der Physik **531** (2019).

- M. Bartelmann, F. Fabis, D. Berg, E. Kozlikin, R. Lilow and C. Viermann. *A microscopic, non-equilibrium, statistical field theory for cosmic structure formation*. New Journal of Physics **18** (2016).

- R. Lilow, F. Fabis, E. Kozlikin, C. Viermann and M. Bartelmann. *Resummed Kinetic Field Theory: general formalism and linear structure growth from Newtonian particle dynamics*. Journal of Cosmology and Astroparticle Physics. **4** (2019).

- E. Kozlikin, F. Fabis, R. Lilow, C. Viermann and M. Bartelmann. *Non-equilibrium statistical field theory for classical particles: Impact of correlated initial conditions on non-ideal gases*. arXiv:1412.2715 (2014).

Bibliography

[1] S. W. Hawking. Black hole explosions? *Nature*, 248(5443):30–31, 1974.

[2] S. W. Hawking. Particle Creation by Black Holes. *Commun. Math. Phys.*, 43:199–220, 1975.

[3] L. Parker. Quantized fields and particle creation in expanding universes. i. *Phys. Rev.*, 183: 1057–1068, 1969.

[4] S. Weinberg. *Cosmology*. Oxford University Press, 2008.

[5] S. Dodelson. *Modern Cosmology*. Academic Press, Elsevier Science, 2003.

[6] W. G. Unruh. Experimental black-hole evaporation? *Phys. Rev. Lett.*, 46:1351–1353, 1981.

[7] T. Jacobson. Black-hole evaporation and ultrashort distances. *Phys. Rev. D*, 44:1731–1739, 1991.

[8] M. Visser. Hawking radiation without black hole entropy. *Phys. Rev. Lett.*, 80:3436–3439, 1998.

[9] M. Visser. Acoustic black holes: horizons, ergospheres and Hawking radiation. *CQGRDG*, 15 (6):1767–1791, 1998.

[10] G.E. Volovik. Is there analogy between quantized vortex and black hole?, 1995.

[11] G. E. Volovik. *The Universe in a helium droplet*. Oxford University Press, 2009.

[12] L. J. Garay, J. R. Anglin, J. I. Cirac, and P. Zoller. Sonic analog of gravitational black holes in Bose-Einstein condensates. *Phys. Rev. Lett.*, 85:4643–4647, 2000.

[13] L. J. Garay, J. R. Anglin, J. I. Cirac, and P. Zoller. Sonic black holes in dilute Bose-Einstein condensates. *Phys. Rev. A*, 63:023611, 2001.

[14] C. Barceló, S. Liberati, and M. Visser. Analogue gravity from Bose-Einstein condensates. *CQGRDG*, 18(6):1137–1156, 2001.

[15] C. Barceló, S. Liberati, and M. Visser. Towards the observation of hawking radiation in Bose–Einstein condensates. *IJMPA*, 18(21):3735–3745, 2003.

[16] T. G. Philbin, C. Kuklewicz, S. Robertson, S. Hill, F. König, and U. Leonhardt. Fiber-optical analog of the event horizon. *Science*, 319(5868):1367–1370, 2008.

[17] G. Rousseaux, C. Mathis, P. Maïssa, T. G. Philbin, and U. Leonhardt. Observation of negative-frequency waves in a water tank: a classical analogue to the Hawking effect? *New J. Phys.*, 10 (5):053015, 2008.

[18] S. Weinfurtner, E. W. Tedford, M. C. J. Penrice, W. G. Unruh, and G. A. Lawrence. Measurement of Stimulated Hawking Emission in an Analogue System. *Phys. Rev. Lett.*, 106:021302, 2011.

[19] O. Lahav, A. Itah, A. Blumkin, C. Gordon, S. Rinott, A. Zayats, and J. Steinhauer. Realization of a sonic black hole analog in a Bose-Einstein condensate. *Phys. Rev. Lett.*, 105:240401, 2010.

[20] J. Steinhauer. Observation of self-amplifying Hawking radiation in an analogue black-hole laser. *Nat. Phys.*, 10(11):864–869, 2014.

[21] J. Steinhauer and J. R. M. Muñoz de Nova. Self-amplifying Hawking radiation and its background: A numerical study. *Phys. Rev. A*, 95:033604, 2017.

[22] J. R. Muñoz de Nova, K. Golubkov, Victor I. K., and J. Steinhauer. Observation of thermal Hawking radiation and its temperature in an analogue black hole. *Nature*, 569(7758):688–691, 2019.

[23] J.-C. Jaskula, G. B. Partridge, M. Bonneau, R. Lopes, J. Ruaudel, D. Boiron, and C. I. Westbrook. Acoustic analog to the dynamical Casimir effect in a Bose-Einstein condensate. *Phys. Rev. Lett.*, 109:220401, 2012.

[24] C. Barcelo, S. Liberati, and M. Visser. Analogue gravity. *Living Rev. Rel.*, 8:12, 2005.

[25] R. Schützhold. Recreating fundamental effects in the laboratory? *arXiv*, 2010.

[26] M. J. Jacquet, S. Weinfurtner, and F. König. The next generation of analogue gravity experiments. *Phil. Trans. Roy. Soc. Lond. A*, 378(2177):20190239, 2020.

[27] A. Marte, T. Volz, J. Schuster, S. Dürr, G. Rempe, E. Kempen, and B. J. Verhaar. Feshbach resonances in rubidium 87: Precision measurement and analysis. *Phys. Revl. Lett.*, 89:283202, 2003.

[28] M. W. Zwierlein, C. A. Stan, C. H. Schunck, S. M. F. Raupach, S. Gupta, Z. Hadzibabic, and W. Ketterle. Observation of Bose-Einstein condensation of molecules. *Phys. Rev. Lett.*, 91(25), 2003.

[29] P. O. Fedichev and U. R. Fischer. Gibbons-Hawking effect in the sonic de sitter space-time of an expanding Bose-Einstein-condensed gas. *Phys. Rev. Lett.*, 91:240407, 2003.

[30] P. O. Fedichev and U. R. Fischer. 'cosmological' quasiparticle production in harmonically trapped superfluid gases. *Phys. Rev. A*, 69:033602, 2004.

[31] C. Barceló, S. Liberati, and M. Visser. Analogue models for FRW cosmologies. *IJMPD*, 12 (09):1641–1649, 2003.

[32] C. Barceló, S. Liberati, and M. Visser. Probing semiclassical analog gravity in Bose-Einstein condensates with widely tunable interactions. *Phys. Rev. A*, 68:053613, 2003.

[33] U. R. Fischer and R. Schützhold. Quantum simulation of cosmic inflation in two-component Bose-Einstein condensates. *Phys. Rev. A*, 70:063615, 2004.

[34] S. Weinfurtner. Analogue model for an expanding universe. *Gen. Relativ. Grav.*, 37(9): 1549–1554, 2005.

[35] U. R. Fischer. Quasiparticle universes in Bose-Einstein condensates. *Mod. Phys. Lett. A*, 19 (24):1789–1812, 2004.

[36] C. Hung, V. Gurarie, and C. Chin. From cosmology to cold atoms: Observation of Sakharov oscillations in a quenched atomic superfluid. *Science*, 341(6151):1213–1215, 2013.

[37] C. Chen, S. Khlebnikov, and C. Hung. Observation of Quasiparticle Pair Production and Quantum Entanglement in Atomic Quantum Gases Quenched to an Attractive Interaction. *Phys. Rev. Lett.*, 127:060404, 2021.

[38] S. Eckel, A. Kumar, T. Jacobson, I. B. Spielman, and G. K. Campbell. A rapidly expanding Bose-Einstein condensate: An expanding universe in the lab. *Phys. Rev. X*, 8:021021, 2018.

[39] S. Banik, M. Gutierrez Galan, H. Sosa-Martinez, M. Anderson, S. Eckel, I. B. Spielman, and G. K. Campbell. Accurate determination of hubble attenuation and amplification in expanding and contracting cold-atom universes. *Physical Review Letters*, 128(9), 2022.

[40] J. Steinhauer, M. Abuzarli, T. Aladjidi, T. Bienaimé, C. Piekarski, W. Liu, E. Giacobino, A. Bramati, and Q. Glorieux. Analogue cosmological particle creation in an ultracold quantum fluid of light. *arXiv*, 2021.

[41] M. Tolosa-Simeón, Á. Parra-López, N. Sánchez-Kuntz, T. Haas, C. Viermann, M. Sparn, N. Liebster, M. Hans, E. Kath, H. Strobel, M. K. Oberthaler, and S. Floerchinger. Curved and expanding spacetime geometries in Bose-Einstein condensates. *arXiv*, 2022.

[42] C. Viermann, M. Sparn, N. Liebster, M. Hans, E. Kath, Á. Parra-López, M. Tolosa-Simeón, N. Sánchez-Kuntz, T. Haas, H. Strobel, S. Floerchinger, and M. K. Oberthaler. Quantum field simulator for dynamics in curved spacetime. *arXiv*, 2022.

[43] S. Carroll. *Spacetime and Geometry: An Introduction to General Relativity*. Benjamin Cummings, 2003.

[44] M. Bartelmann. Lecture notes 'Cosmology', 2022.

[45] M. Bartelmann. Lecture notes 'General Relativity', 2022.

[46] S. Chen, G.W. Gibbons, Y. Li, and Y. Yang. Friedmann's equations in all dimensions and Chebyshev's theorem. *J. Cosmol. Astropart. Phys.*, 2014.

[47] L. Amendola and S. Tsujikawa. *Dark Energy: Theory and Observations*. Cambridge University Press, 2010.

[48] A. Albrecht. Coherence and Sakharov oscillations in the microwave sky. *arXiv*, 1996.

[49] E. Madelung. Quantentheorie in hydrodynamischer Form. *Z. Phys.*, 40(3):322–326, 1927.

[50] P. Jain, S. Weinfurtner, M. Visser, and C. W. Gardiner. Analog model of a Friedmann-Robertson-Walker universe in Bose-Einstein condensates: Application of the classical field method. *Phys. Rev. A*, 76:033616, 2007.

[51] C.-J. Foot. *Atomic physics*. Oxford University Press, USA, 2014.

[52] H. J. Metcalf and P. van der Straten. *Laser Cooling and Trapping*. Springer-Verlag, New York, 1999.

[53] T. G. Tiecke. Properties of potassium, 2011.

[54] H. Wang, P. Gould, and W. Stwalley. Long-range interaction of the 39K(4s) + 39K(4p) asymptote by photoassociative spectroscopy. i: The 0g- pure long-range state and the long-range potential constants. *Chem. Phys.*, 106:7899, 1997.

[55] S. Falke, E. Tiemann, C. Lisdat, H. Schnatz, and G. Grosche. Transition frequencies of the *D* lines of ^{39}K, ^{40}K, and ^{41}K measured with a femtosecond laser frequency comb. *Phys. Rev. A*, 74:032503, 2006.

[56] E. Arimondo, M. Inguscio, and P. Violino. Experimental determinations of the hyperfine structure in the alkali atoms. *Rev. Mod. Phys.*, 49:31–75, 1977.

[57] G. Breit and I. I. Rabi. Measurement of nuclear spin. *Phys. Rev.*, 38:2082–2083, 1931.

[58] B. Erdmann. Wechselwirkung von atomaren Mehrniveau-Systemen mit Laserlicht. *Bachelor thesis*, 2019.

[59] J. Dreher. An offset locking scheme for absorption imaging of 39K at high magnetic fields. *Bachelor thesis*, 2021.

[60] F. Schmutte. Closed optical cycle scheme for absorption imaging of 39K atoms at intermediate magnetic field strengths. *Bachelor thesis*, 2020.

[61] M. Hans. in preparation. *PhD thesis*, 2022.

[62] R. Grimm, M. Weidemüller, and Y. Ovchinnikov. Optical dipole traps for neutral atoms. *Adv. At. Mol. Opt. Phys.*, 42:95, 2000.

[63] C. Chin, R. Grimm, P. Julienne, and E. Tiesinga. Feshbach resonances in ultracold gases. *Rev. Mod. Phys.*, 82:1225–1286, 2010.

[64] W. Ketterle, D. S. Durfee, and D. M. Stamper-kurn. *Making, probing and understanding Bose-Einstein condensates*. Press, 1999.

[65] G. Gauthier, I. Lenton, N. McKay Parry, M. Baker, M. J. Davis, H. Rubinsztein-Dunlop, and T. W. Neely. Direct imaging of a digital-micromirror device for configurable microscopic optical potentials. *Optica*, 3(10):1136–1143, 2016.

[66] M. Sparn. A setup for creating arbitrary potentials in a two-dimensional 39K BEC with a digital micromirror device. *Master thesis*, 2020.

[67] J. Dalibard and C. Cohen-Tannoudji. Laser cooling below the doppler limit by polarization gradients: simple theoretical models. *J. Opt. Soc. Am. B*, 6(11):2023–2045, 1989.

[68] M. Landini, S. Roy, L. Carcagní, D. Trypogeorgos, M. Fattori, M. Inguscio, and G. Modugno. Sub-doppler laser cooling of potassium atoms. *Phys. Rev. A*, 84:043432, 2011.

[69] V. Gokhroo, G. Rajalakshmi, R. Easwaran, and C.S. Unnikrishnan. Sub-doppler deep-cooled bosonic and fermionic isotopes of potassium in a compact 2D+–3D MOT set-up. *J. Phys. B*, 44:115307, 2011.

[70] M. Landini. A tunable Bose-Einstein condensate for quantum interferometry. *PhD thesis*, 2008.

[71] K.-J. Boller, A. Imamoğlu, and S. E. Harris. Observation of electromagnetically induced transparency. *Phys. Rev. Lett.*, 66:2593–2596, 1991.

[72] A. Aspect, E. Arimondo, R. Kaiser, N. Vansteenkiste, and C. Cohen-Tannoudji. Laser cooling below the one-photon recoil energy by velocity-selective coherent population trapping. *Phys. Rev. Lett.*, 61:826–829, 1988.

[73] M. Weidemüller, T. Esslinger, M. A. Ol'shanii, A. Hemmerich, and T. W Hänsch. A novel scheme for efficient cooling below the photon recoil limit. *EPL*, 27(2):109–114, 1994.

[74] M. Gerken. Gray molasses cooling of lithium-6 towards a degenerate Fermi gas. *Master thesis*, 2016.

[75] D. Nath, R. K. Easwaran, G. Rajalakshmi, and C. S. Unnikrishnan. Quantum-interference-enhanced deep sub-Doppler cooling of ^{39}K atoms in gray molasses. *Phys. Rev. A*, 88:053407, 2013.

[76] G. Salomon, L. Fouché, P. Wang, A. Aspect, P. Bouyer, and T. Bourdel. Gray-molasses cooling of 39K to a high phase-space density. *EPL (Europhysics Letters)*, 104(6):63002, 2013.

[77] G. Reinaudi, T. Lahaye, Z. Wang, and D. Guéry-Odelin. Strong saturation absorption imaging of dense clouds of ultracold atoms. *Opt. Lett.*, 32(21):3143–3145, 2007.

[78] A. Bergschneider, V. M. Klinkhamer, J. H. Becher, R. Klemt, G. Zürn, P. M. Preiss, and S. Jochim. Spin-resolved single-atom imaging of ^{6}Li in free space. *Phys. Rev. A*, 97:063613, 2018.

[79] M. Hans, F. Schmutte, C. Viermann, N. Liebster, M. Sparn, M. K. Oberthaler, and H. Strobel. High signal to noise absorption imaging of alkali atoms at moderate magnetic fields. *Rev. Sci. Instr.*, 92(2):023203, 2021.

[80] G. Salomon, L. Fouché, S. Lepoutre, A. Aspect, and T. Bourdel. All-optical cooling of ^{39}K to Bose-Einstein condensation. *Phys. Rev. A*, 90:033405, 2014.

[81] C. R. Cabrera Córdova. Quantum liquid droplets in a mixture of Bose-Einstein condensates, 2018.

[82] G. Semeghini. Ultracold atoms in three-dimensional disorder. *PhD thesis*, 2015.

[83] J. Krieger. Zeeman-Slower und Experimentsteuerung für das NaLi-Experiment. *Diploma thesis*, 2008.

[84] I. Stroescu. On a cold beam of potassium. *Dipolma thesis*, 2010.

[85] W. Müssel. Characterization of a two-dimensional MOT for 39K. *Dipolma thesis*, 2011.

[86] M. Hans. An experimental setup for a potassium Bose-Einstein condensate with tunable interactions. *Master thesis*, 2017.

[87] M. Sparn. Magnetic fields for cooling and trapping of potassium atoms. *Bachelor thesis*, 2017.

[88] P. Anantha Murthy. Emergent phenomena in two-dimensional Fermi systems. *PhD thesis*, 2018.

[89] C. D'Errico, M. Zaccanti, M. Fattori, G. Roati, M. Inguscio, G. Modugno, and A. Simoni. Feshbach resonances in ultracold39K. *New J. Phys.*, 9(7):223–223, 2007.

[90] D. W. Preston. Simple scheme for tunable frequency offset locking of two lasers. *Am. J. Phys.*, 64:1432–1436, 1996.

[91] W. Demtröder. *Laserspektroskopie 1: Grundlagen*. Springer Berlin Heidelberg, 2011.

[92] A. Impertro. Laser system for magneto-optical cooling and trapping of potassium. *Bachelor thesis*, 2017.

[93] F. Nicolai. Design and construction of a fiber-coupled tapered amplifier system. *Master thesis*, 2017.

[94] E.A. Donley, T. Heavner, F. Levi, M. Tataw, and S. Jefferts. Double-pass acousto-optic modulator system. *Rev. Sci. Instr.*, 76, 2005.

[95] A. Beikert. Controlled frequency generation for grey molasses cooling. *Bachelor thesis*, 2021.

[96] U. Schunemann, H. Engler, R. Grimm, M. Weidemüller, and M. Zielonkowski. Simple scheme for tunable frequency offset locking of two lasers. *Rev. Sci. Instrum.*, 70:242 – 243, 1999.

[97] A. Kobyakov, M. Sauer, and D. Chowdhury. Stimulated brillouin scattering in optical fibers. *Adv. Opt. Photon.*, 2(1):1–59, 2010.

[98] R. Saint-Jalm, P. C. M. Castilho, É. Le Cerf, B. Bakkali-Hassani, J.-L. Ville, S. Nascimbene, J. Beugnon, and J. Dalibard. Dynamical symmetry and breathers in a two-dimensional Bose gas. *Phys. Rev. X*, 9:021035, 2019.

[99] G. Gauthier, T. A. Bell, A. B. Stilgoe, M. Baker, H. Rubinsztein-Dunlop, and T. W. Neely. Dynamic high-resolution optical trapping of ultracold atoms. *Adv. At. Mol. Opt. Phys.*, page 1–101, 2021.

[100] E. Schrödinger. The proper vibrations of the expanding universe. *Physica VI, no 9*, 1939.

[101] N. Sánchez-Kuntz, Á. Parra-López, M. Tolosa-Simeón, T. Haas, and S. Floerchinger. Scalar quantum fields in cosmologies with 2+1 spacetime dimensions. *arXiv*, 2022.

[102] M. Born and V. Fock. Beweis des Adiabatensatzes. *Zeitschrift für Physik*, 51:165–180, 1928.

[103] D. Griffiths. *Introduction to Quantum Mechanics*. Prentice Hall PTR, 1994.

[104] L. P. Grishchuk. Cosmological Sakharov oscillations and quantum mechanics of the early Universe. *Phys.-Uspekhi*, 55(2):210–216, 2012.

[105] Marcel Leutenegger. Matlab package 'hat.m', 2006.

[106] S. Giorgini, L. P. Pitaevskii, and S. Stringari. Condensate fraction and critical temperature of a trapped interacting Bose gas. *Phys. Rev. A*, 54:R4633–R4636, 1996.

Acknowledgements

First of all, I want to thank Markus Oberthaler for accepting me into his group, showing me the world of quantum research, and introducing me to the exciting work of the Structures cluster. Thank you for letting me join in your vision for future research and for the catching enthusiasm with which you create new ideas. Thank you also for your trust and the freedom you gave me in pursuing this somewhat strange but wonderful topic.

Special thanks go to Matthias Bartelmann, who shaped my fascination for cosmology and deeply influenced my approach to physics and my understanding of science. Thank you especially for supporting me in my decision to switch from theoretical to experimental physics, for never giving up on me in that process, and for reviewing this work that resulted from my second chance.

For being part of my defense committee, I want to thank Wolfram Pernice and André Butz. I am looking forward to discussing this work with you!

I also want to thank Helmut Strobel, who taught me everything I know about the work in the laboratory, including the millions of small tricks that make all the difference in building and stabilizing an ultracold atom experiment. Thank you for your never-ending patience and for many long days and some nights during which we tried to reach the next milestone in the construction of the experiment – and sometimes even succeeded.

None of this work would have been possible without the awesome members of the BECK team. This includes the current team – in the order of their joining – Maurus Hans, Marius Sparn, Nikolas Liebster, and Elinor Kath; and the students that worked with us over the years and added their own mark to the development of the experiment. These are Alexander Impertro, Benedikt Erdmann, Jan Dreher, Finn Schmutte, and Alexandra Beikert. Thank you all for your support and the many contributions to this thesis, for sharing work, discussing ideas, correcting this text, and for all the non-sense and fun in between. This thank extends to the entire Matterwave team and the members of the other SYNQS experiments.

In addition to the experimental team, I want to thank the theory group of our collaboration. These are Tobias Haas, Natalia Sánchez-Kuntz, Mireia Tolosa-Simeón, Álvaro Parra-López, Simon Brunner, and of course, Stefan Flörchinger. Thank you for proposing the idea in its very initial form and for your incredible stamina in exploring and iterating both theoretical and experimental concepts and details until our results emerged. I am still amazed at how well everything worked out and that it is so stunningly beautiful.

Building the experiment would have been impossible without the members of the KIP's electronic and mechanic workshops and especially David Jansen. Thank you for the many developments and parts you added to the machine and for never despairing over our short-notice, late-afternoon, very-urgent, and sometimes absurd requests.

Thank you all so much for every single step of the way!

Finally, I want to thank my family and friends who accompanied me during these years and joined in all the ups and downs. Thank you for enjoying the good times together, celebrating successes, and your help and support, especially in times of frustration. I am glad and honored that you are part of my very own little universe.